UNIVERSITÀ DEGLI STUDI DI PADOVA

University College Dublin
Ireland's Global University

Sede Amministrativa: Università degli Studi di Padova

Consiglio nazionale delle ricerche, Istituto di Fotonica e Nanotecnologie (CNR-IFN), Padova

Dipartimento di Ingegneria dell'Informazione (DEI)

SCUOLA DI DOTTORATO DI RICERCA IN: Ingegneria dell'Informazione

INDIRIZZO: Scienza e tecnologia dell'Informazione

CICLO: XXXII

TESI IN COTUTELA

Optical characterization of graphene in vacuum ultraviolet spectral region & spectroscopic studies of colliding laser plasmas (Al, Si)

Direttore della Scuola: Prof.Andrea Neviani

Supervisore: Ch.mo Prof. Piergiorgio Nicolosi

Supervisore: Ch.mo Prof. Thomas McCormack

Dottorando: Nadeem Ahmed Malik

2019

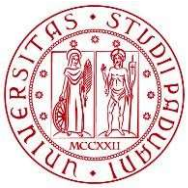

UNIVERSITÀ DEGLI STUDI DI PADOVA

University College Dublin
Ireland's Global University

Optical characterization of graphene in vacuum ultraviolet spectral region & spectroscopic studies of colliding laser plasmas (Al, Si)

Nadeem Ahmed Malik

Thesis presented for the degree

of

Doctor of Philosophy

To the

School of Physics
College of Science
University College Dublin, Ireland

And

Department of Information Engineering

University of Padova, Italy

Supervisors: Prof. Piergiorgio Nicolosi, Prof. Thomas McCormack

Head of School: Prof. Martin Grünewald

2019

Dedication

I would like to dedicate this endeavor to my parents and family, whom I love the most. Especially, I dedicate this work to my beloved father (late) Noor Ahmed, who is no more in this world, but his memories and teachings are always there to regulate my life. He was the humblest and kind person I have ever met. There is a void, after he left, that can never be filled. We miss you a lot 'Abu Jee'. May Allah (SWT) grant him Jannat- ul- Firdous. Ameen

Summary

The aim of this research is to investigate and explore new innovative material(s) and techniques regarding development and improvement of vacuum ultraviolet (VUV) and extreme ultraviolet (EUV) optics and sources; for the advancement of EUV and VUV technological areas like space exploration (e.g. observation and spectroscopic diagnostics of the solar corona) and EUV lithography (e.g. advancement and minimization of integrated electronic circuits (ICs)).

The research work was primarily focused on the investigations of the optical and structural properties of graphene (mono and few-layer) deposited on SiO_2/Si substrate in VUV spectral region by exploiting different diagnostic techniques, based on reflection and polarimetric measurements.

The study was addressed starting from silicon dioxide deposited on silicon (SiO_2 / Si), which works as the substrate for graphene samples. The optical properties of SiO_2/Si were thoroughly investigated at the hydrogen Lyman–alpha line (121.6 nm) by employing the tabletop EUV-VUV polarimetry facility located at CNR-INF Padova. An approach based on the combined use of reflectometry with polarimetry technique was used to find out the reliable values of the optical constants. The results show the potential of the approach and it was demonstrated in this study that the optical constants retrieved by using ellipsometric parameters; ratio (ρ), and phase shift (ϕ), are more reliable than the retrieved one using least square fitting of the reflectivity. Moreover, it was found that SiO_2 behaves as a phase retarder by introducing a phase difference between the *s*- and *p*- polarization components of the incoming light. The phase differences observed was 18° to 160° depending on the incidence angle.

Using the similar experimental technique, the ellipsometric parameters (phase shift (ϕ), ratio (ρ)) of graphene (1LG/SiO_2/Si) sample were also investigated and compared with that of SiO_2/Si to know the effect of the graphene as capping layer. It was found that 1LG on top of SiO_2 improves optical throughput and despite having atomic thickness it affects the polarimetric properties of the underlying substrate.

Further, detailed optical properties of mono (1L) and tri-layer (3L) of commercial graphene grown on (SiO_2/Si) substrate were studied at hydrogen Lyman alpha by using laboratory based (at CNR-IFN, Padova) and synchrotron light-based (at BEAR beamline, Elettra synchrotron) EUV-VUV reflectometer setups. Angular reflectance measurements of graphene samples along with bare

substrate were performed by taking into account the light polarization. Distinguishable optical performance was observed for both samples (1LG and 3LG) in spite of the ultra-thin thickness of the films. Optical anisotropy with the axis of symmetry nearly perpendicular to the surface and coherently related to the p-orbitals structural orientation has been experimentally demonstrated. Anisotropic "effective optical constants" corresponding to "effective thickness" were retrieved by simulating the interaction of the electromagnetic wave with the structure of the sample. Furthermore, the reliability of the derived optical constants was tested qualitatively by deducing surface differential reflectance (SDR) from the reflectance measurements. Another very interesting effect induced by graphene is the shift of the pseudo-Brewster angle with respect to what was observed for the substrate. The downshift of the pseudo-Brewster angle was observed for both samples 1LG (-1.5°), and 3LG (-5°), with larger shift for an increasing number of layers. However, in literature an upshift in the Brewster angle is reported but for different spectral region. AFM, XPS and Raman spectroscopies were used to study surface morphology, quality of graphene coatings, and to estimate the thickness/ number of layers.

To the best of our knowledge, these remarkable optical properties of graphene at VUV spectral region was determined for the first time and results are of considerable interest for VUV optics advancement.

The last part of the thesis is about the study of the stagnation layer formed at the collision front of two colliding plasmas by employing time resolved spectroscopic technique. Time evolution and dynamics of the Al-Al, Al-Si colliding plasmas studied and compared in the case of flat and wedge targets. It was observed that in case of wedge target the overall emission from stagnation layer was more intense and higher ionization states of (Al and Si) appeared earlier in time having higher intensity compared to the flat target. The time evolution of the electron number density was also studied and it was observed that wedge target results in a relatively higher electron number density.

Sommario

Il presente lavoro di tesi ha come obiettivo principale lo studio di materiali innovativi per lo sviluppo di componenti ottici nella regione spettrale dell'estremo ultravioletto (EUV) e dell'ultravioletto da vuoto (VUV). I campi di applicazione sono molteplici e spaziano dalla litografia EUV all'esplorazione spaziale. Questo tipo di ricerca richiede contemporaneamente l'utilizzo e la messa a punto di adeguati metodi di caratterizzazione, che permettano una completa analisi delle proprietà nella regione spettrale di interesse.

Il risultato più interessante presentato è sicuramente l'analisi ottica e strutturale di strati di grafene (singolo e triplo) depositati su silicon oxide, nella regione spettrale dell'ultravioletto da vuoto. Lo studio è stato affrontato combinando diverse tecniche sperimentali e partendo dalle proprietà ottiche dell'ossido di silicio depositato su silicio (SiO_2/Si), che costituisce il substrato.

Il SiO_2/Si è stato caratterizzato alla hydrogen Lyman-alpha (121.6 nm) utilizzando un riflettometro dedicato alla riflettometria nell'ultravioletto e recentemente implementato per misure polarimetriche (CNR-IFN Padova).

Sono stati determinati i parametri ellissometrici, *ratio* (ρ) and *phase shift* (ϕ), le costanti ottiche e le proprietà polarimetriche del silicon oxide. Il SiO_2 si comporta effettivamente come una lamina di ritardo introducendo una differenza di fase tra le componenti *s*- e *p*- della radiazione incidente. La differenza di fase introdotta varia dai 18° ai 160° e dipende dall'angolo di incidenza.

Successivamente, lo stesso tipo di analisi sperimentale è stata completata per i campioni con uno strato di grafene depositato sull'ossido di silicio (1LG/SiO_2/Si). E' stato osservato che, nonostante il sottile spessore, il singolo strato di grafene migliora la riflettività del substrato. Dall'analisi polarimetrica, non si può invece affermare che il grafene introduca un ritardo di fase osservabile.

Le costanti ottiche del singolo e triplo strato di graphene cresciuto su SiO_2/Si sono state studiate alla hydrogen Lyman-alpha utilizzando misure in riflettometria in polarizzazione *s*- e *p*- acquisite utilizzando luce di sincrotrone (ELETTRA Trieste, BEAR beamline).

Si notano differenze misurabile nella riflettività dei campioni. Le differenze dipendono dal numero di strati di graphene. Queste misure sono state utilizzate per ricavare le costanti ottiche. E' stata inoltre sperimentalmente osservato una anisotropia ottica con asse di simmetria quasi perpendicolare

alla superficie e coerentemente correlata all'orientamento degli orbitali π. Le costanti ottiche efficaci sono state ricavate simulando l'interazione della radiazione elettromagnetica con la struttura del campione. Inoltre, l'attendibilità delle costanti ottiche trovate è stata qualitativamente testata ricavando la *"surface differential reflectance (SDR)"* dalle misure di riflettività.

Un altro effetto molto interessante indotto dal grafene è lo spostamento dell'angolo di pseudo-Brewster rispetto a quanto osservato per il substrato. Lo spostamento, che cresce in valore assoluto con il numero di strati, induce un *downshift* contrariamente a quanto osservato in altre regioni spettrali. La qualità della superficie, la morfologia e il numero di layer sono stati caratterizzati con misure di microscopia a forza atomica e spettroscopia Raman. Per quanto ne sappiamo, questi risultati relativi allo studio delle proprietà ottiche del grafene nel VUV sono assolutamente nuovi.

L'ultima parte della tesi riguarda lo studio dello strato di stagnazione che si forma sul fronte di collisione di due plasmi collidenti. La tecnica utilizzata è una spettroscopia risolta in tempo. Il tempo di evoluzione e le dinamiche dei plasmi collidenti di Al-Al e Al-Si sono stati studiati con tecniche spettroscopiche risolte in tempo. È stato osservato che nel caso di un "wedge target" lo strato di ristagno produce uno spettro più luminoso e in precedenza sono comparsi stati di ionizzazione più elevati con un'intensità relativamente più elevata di un "flat target". Il tempo di evoluzione della densità elettronica è stato studiato e confrontato nel caso delle due configurazioni con i target diversi e una densità elettronica relativamente più alta è stata osservata nel caso di "wedge target".

Acknowledgments

Firstly, I would like to express my profound appreciativeness and sincere thanks to my advisors Prof. Piergiorgio Nicolosi, Dr. Tom McCormack and Dr. Paola Zuppella, for their patience, continuous guidance, wholehearted encouragement and useful assessments of research work based on their vast knowledge and experience, without their immense support this thesis would not have been possible.

I would also like to express great appreciation to Dr. Fergal O'Reilly for his valuable and constructive suggestions during the planning and execution of research activities while I was on my research mobility period at UCD, Dublin Ireland.

I am also thankful and appreciate the great support and guidance from Dr. Angelo Giglia during beamtime experiments at BEAR beamline–ELETTRA Synchrotron. It is my pleasure also to acknowledge, Prof. Stefano Nannarone, Prof. Luca Pasquali and Dr. Konstantin Koshmak (BEAR beamline–ELETTRA Synchrotron) for their support for beamline experiments.

Immense gratitude to the administrative staff of the department of information engineering (DEI), University of Padova and school of physics University College Dublin for supporting me for all the bureaucratic work. I am also grateful to the director of the CNR-IFN Dr. Luca Poletto, administrative and academic staff of CNR-IFN Padova for supporting and providing me a pleasant research environment.

I am thankful to my fellow partner in the EXTATIC program, especially to my direct colleagues from the program: Ahmed Eid Gaballah, Kety Mayelin Jimenez and Mewael Sertsu, for their support and useful discussions.

Furthermore, I also like to extend my acknowledgments to the financial support from The Education, Audiovisual, and Culture Executive Agency (EACEA), Erasmus Mundus Joint Doctorate, EXTATIC Program under framework partnership Agreement No. 2012-0033.

I am so much grateful to my father (late: April 2019) and my mother for their continuous encouragement and support. Lastly, I am incredibly thankful to my wife and daughters for their patience and allowing me to pursue my Ph.D. far away from them. Without my parents and family support it would not be possible to move forward.

Publications and Conference Presentations

Publications during the Ph.D. program

1. **Nadeem Ahmed**, P. Nicolosi, A. E. H. Gaballah, K. Jimenez, and P. Zuppella "EUV reflective ellipsometry in laboratory: determination of the optical constants and phase retarder properties of SiO2 at hydrogen Lyman–alpha", Proc. SPIE 11032, EUV and X-ray Optics: Synergy between Laboratory and Space VI, 110320V (26 April 2019); https://doi.org/10.1117/12.2520834 **(BEST PAPER AWARD)**

2. Paola Zuppella, Ahmed E. H. Gaballah, **Nadeem Ahmed**, Kety Jimenez, and Piergiorgio Nicolosi "Optical performances of new materials in the EUV spectral range: metrology, methods and results", Proc. SPIE 11032, EUV and X-ray Optics: Synergy between Laboratory and Space VI, 110320B (26 April 2019); https://doi.org/10.1117/12.2525893.

3. Paola Zuppella, Ahmed E. H. Gaballah, **Nadeem Ahmed**, Kety Jimenez, and Piergiorgio Nicolosi. "Characterization of optical materials for EUV spectral region: Methods and analysis." AIP Conference Proceedings 2146, KEYTECH 2019, 020024 (2019). https://doi.org/10.1063/1.5123711.

4. A.E.H. Gaballah, P.Zuppella, **Nadeem Ahmed**, K. Jimenez, G. Pettinari, A. Gerardino , P. Nicolosi, "A tabletop polarimetric facility for the EUV spectral range: implementations and characterization". Proc. SPIE 10235, UV and X-ray Optics: Synergy between Laboratory and Space (2017). https://doi.org/10.1117/12.2265592.

5. K. Jimenez, A.E.H. Gaballah, **Nadeem. Ahmed**, P. Zuppella, P.Nicolosi "Optical and structural characterization of Nb, Zr, Nb/Zr, Zr/Nb thin films on Si3N4 membranes windows". Proc. SPIE 10236, Damage to VUV, EUV, and X-ray Optics (2017). https://doi.org/10.1117/12.2267348.

6. A.E.H. Gaballah, P. Nicolosi, **Nadeem Ahmed**, K. Jimenez, G. Pettinari, A. Gerardino, P.Zuppella "EUV polarimetry for thin film and surface characterization and EUV phase retarder reflector development" Rev. Sci. Instrum. 89, 015108 (2018). https://doi.org/10.1063/1.5010786.

7. A.E.H. Gaballah, P. Nicolosi, P.Zuppella, **Nadeem Ahmed**, K. Jimenez, G. Pettinari, A. Gerardino, P. Nicolosi "Vacuum ultraviolet quarter wave plates based on SnTe/Al bilayer: design, fabrication and ellipsometric characterization", Appl. Surf. Sci. 463 (2018) 75–81. doi:10.1016/j.apsusc.2018.08.190.

8. K. Jimenez, P. Nicolosi, L. Juschkin, **Nadeem. Ahmed**, A.E.H. Gaballah, E. Cattaruzza, M. G. Sertsu, A. Gerardino, A. Giglia, G. Mussler, P. Zuppella. "EUV free-standing

transmittance filters, for high brilliance sources, based on Nb/Zr and Zr/Nb thin films on Si3N4 membranes; Design, fabrication, optical and structural characterization". (**Accepted in thin solid film 2019**).

9. **Nadeem Ahmed**, P. Nicolosi, K. Jimenez , A.E.H. Gaballah, A. Giglia, P. Zuppella, "Experimental Evidence For VUV Optical Anisotropy of Few Layers Graphene Coating. " (**ready for submission**)

Other publications by Author

10. A Mahmood, **Nadeem Ahmed***, Q Raza, Taj Muhammad Khan, M Mehmood, M M Hassan, and N Mahmood, "Effect of thermal annealing on the structural and optical properties of ZnO thin films deposited by the reactive e-beam evaporation technique". Phys. Scr. 82 (2010) 065801 (8pp). https://doi.org/10.1088/0031-8949/82/06/065801.

11. Afzaal Qamar, Arshad Mahmood, Tuba Sarwar, **Nadeem Ahmed**, "Synthesis and characterization of porous crystalline SiC thin films prepared by radio frequency reactive magnetron sputtering technique". Applied Surface Science, 257 (15) (2011), 6923 (5pp). https://doi.org/10.1016/j.apsusc.2011.03.033.

Presentations at Conferences and Workshops

- **EXTATIC Workshop**, "Optical properties of 2D materials in EUV-VUV spectral region" (16-20 January 2017) at the International Centre for Theoretical Physics (ICTP) in Trieste, Italy. **(Oral Presentation)**
- **Graphene 2017,** (March 28-30, 2017), Barcelona, Spain.
- **EXTATIC Workshop**, "Optical properties of 2D materials in EUV-VUV spectral region", (22-24 September, 2017) at Czech Technical University (CTU), Prague, Czech Republic. **(Oral Presentation)**
- **304. PTB-Seminar VUV and EUV Metrology,** "EUV/FUV polarimetric study of Single-layer graphene/SiO_2 (285nm)/Silicon", (19-20 October 2017), Berlin, Germany. **(Poster Presentation)**
- **Graphene 2018,** "Preliminary study on the optical properties of single (few) layer graphene/SiO_2". (26- 29 June 2018), Dresden, Germany. (**Poster Presentation**)
- **PXRMS 2018**, "Optical properties of graphene at hydrogen Lyman-alpha." (07-09 Nov, 2018). Paris, France. **(Poster Presentation)**
- **SPIE Optics+ optoelectronics** "EUV reflective ellipsometry in laboratory: determination of the optical constants and phase retarder properties of SiO_2 at hydrogen Lyman–alpha". (01-05 April 2019) Prague, Czech Republic. **(Poster Presentation).** Received Best Student Paper Award**.**

- **Training & measurement sessions**: optical characterization of materials in EUV spectral range at BEAR beamline, ELETTRA synchrotron Trieste, Italy, (Nov 2016, October 2017)
- **Training & measurement sessions**: optical characterization (transmittance, reflectance and XPS) of 2D materials and membrane filters, at BEAR beamline, ELETTRA synchrotron Trieste, Italy, (March 2018 and November 2018).
- **Training & measurement session:** optical characterization (transmittance and reflectance) of 2D materials and membrane filters, at Optics Beamline, BESSY II, Germany. (January 2019).
- **Training and measurement session:** optical characterization (NEXAFS, reflectance and TEY) of epitaxial graphene and CVD graphene samples, at BEAR beamline, ELETTRA synchrotron Trieste, Italy, (November, 2019).

Glossary

UV	Ultraviolet
VUV	Vacuum Ultraviolet
FUV	Far Ultraviolet
EUV	Extreme Ultraviolet
SXR	Soft X-ray
E.M	Electromagnetic
SE	Spectroscopic Ellipsometry
CL	Capping Layer
FELs	Free Electron Lasers
G	Graphene
1LG	Monolayer Graphene
3LG	Tri-Layer Graphene
QWR	Quarter Wave retarder
QWP	Quarter Wave Plate
HCL	Hollow Cathode lamp
AFM	Atomic Force Microscope
LPP	Laser Produced Plasma
GDP	Gas Discharge Plasma
LPP	Laser Produced Plasma
CLPP	Colliding Laser Produced Plasma
CCDs	Charged Couple Devices
ICCDs	Intensified Charged-Couple Devices
LIBS	Laser Induced Breakdown Spectroscopy
PLD	Pulsed Laser Deposition
CE	Conversion Efficiency
BE	Binding Energy
XPS	X-ray Photoelectron Spectroscopy
MSSTA	Multi-Spectral Solar Telescope Array
TRACE	Transition Region and Coronal Explorer
SOHO	Solar & Heliospheric Observatory
SUMER	Solar Ultraviolet Measurements of Emitted Radiation

Table of Contents

List of Figures

List of Tables

Chapter 1. Introduction and Motivation

1.1 Introduction and Motivation

Since the research has extended the focus to more short wavelengths (i.e., vacuum-ultraviolet (VUV), extreme ultraviolet (EUV) and soft X-ray spectral region). This research work was motivated by different applications related to the short wavelength technological areas, such as space exploration to observe and study the phenomena occurs at the sun which in turn affects our life on earth, EUV lithography, and soft x-ray technologies are of great interest to the modern semiconductor industry. Thus, the need to develop optical elements, systems operating in the vacuum ultraviolet (VUV), extreme ultraviolet (EUV) and soft X-ray are constantly growing. Apart from the new improved optics development, the need to develop techniques to generate short-wavelength light sources at laboratory scale is increasing, which is crucial for the implementation and realization of short wavelength technology at industrial scale. Then fabrication of mirrors, filters, polarizers, and phase retarders for VUV spectral region is in high demand, although it requires proper designs, optimized deposition procedures and proper selection and characterization of materials. For the design of optical elements, accurate knowledge of optical constants is crucial. Optical constants are the fundamental properties of materials which describes how electromagnetic waves propagate through that medium. The optical constants are not only a function of the atomic nature of the material, but they are also strongly dependent on its preparation technique. On the basis of knowledge of optical constants, optical behavior of the material can be predicted qualitatively as well as quantitatively. In some particular cases, it is possible to predict the non-optical properties of materials. One of the main problems with the optics in the EUV-VUV spectral region is that the materials are strongly absorptive exhibiting a complex refractive index n (optical constants) [1]. There is a lack of availability of transmissive optics in this region of the E.M spectrum, which dictates the reflective optics to be used in this spectral region. In VUV spectral region Aluminium optics performance in terms of reflectance is best. However, it undergoes unavoidable oxidation which affects the performance of Al drastically, and Al optics

cannot be used without anti-oxidation coating, which affects the optical throughput of the Al mirror. Different approaches were adopted out of which the most successful is the MgF_2/Al multilayer optics with the cost of reflectivity [2][3]. There is a great demand to explore novel materials for optics development and improvement for short wavelengths technological domains.

Two dimensional (2D) materials are appealing researchers since decades. Their unique crystallographic structure is composed of discrete (2D) layers, having van der Waals interaction instead of ionic or covalent bonding. Among the 2D materials, the most studied are graphene and MoS_2. Graphene is the best known for its unique electrical properties, e.g., high conductivity, zero bandgap and semi-metallic behavior, massless Dirac fermions, ballistic transport [4][5]. Furthermore, the chemical inertness, thermal and chemical stability in harsh environments, mechanical strength, and impermeability to ion diffusion promote graphene as very strong candidate for corrosion resistance and as a protective layer on metals and optical coatings [6][7]. The physical surface of sp^2 carbon allotropes forms a natural diffusion barrier which provides a physical separation between the protected thin film/ coating and reactants. The scientific literature highlights graphene is impermeable to gases as small as Helium [8] providing oxidation resistance at high temperature in the absence of electrolyte [9]. Then, in principle, a perfect sheet without defects and grain boundaries can preserve the surfaces exposed to reactive environments over a long period [6][9].

The optical constants of graphene have been studied in the infrared (IR), visible (VIS), and ultraviolet (UV) spectral regions [10][11]. To date, the optical constants and the optical properties of graphene have not been investigated at the short-wavelength (EUV-VUV) and soft x-ray spectral region. Few studies refer about the interaction between graphene and light at the shorter wavelengths by showing the breaking of ordered sp^2 matrix [12] and, in some cases, the photo reduction process induced by soft x-ray irradiation [13]. There is no experimental evidence concerning the optical throughputs and performance of graphene in this spectral region is available. Therefore, an in-depth investigation at shorter wavelengths is necessary in order to propose innovative applications in many scientific and technological domains, such as the development of space optical components, lithography masks, EUV pellicles [14][15], enhanced optical elements for free-electron lasers, and the fourth generation light sources. We believe that knowing the optical properties, these 2D materials like graphene could have good potential for the EUV-VUV technologies.

Considering the fact that the graphene has atomic thickness and have no optical constant database in EUV-VUV spectral region, we chose relatively simple sample structure G/SiO_2/Si to find and report reliable optical properties of graphene. The SiO_2 was chosen as a substrate material because it is environmentally stable and has been extensively studied for the desired spectral region. Moreover, the quality of graphene films over SiO_2/Si substrate is well optimized.

The choice of the hydrogen Lyman alpha spectral line for the optical performance of graphene is because of the technological importance for solar applications. The hydrogen Lyman alpha spectral line is of great interest for solar corona studies. It is the strongest emission line in the vacuum ultraviolet (VUV) region of the solar spectrum. This spectral line is sensitive to changes in solar atmosphere. Number of space apparatuses have been manufactured and used for imaging the outer solar atmosphere at this spectral line. Some of the examples are; Multi-Spectral Solar Telescope Array (MSSTA) used for taking full-disk images of the Sun at hydrogen Lyman alpha [16], Transition Region and Coronal Explorer (TRACE) spacecraft took pictures of Sun [17] and SUMER spectrograph on SOHO took spectral profiles of the Lyman alpha line from the different areas of solar disc [18].

1.2 Thesis Breakdown

Chapter 1 (current chapter) of the thesis is about the brief introduction and motivation of the research work carried out during Ph.D. Chapter-wise thesis breakdown summary is also presented in this chapter.

Chapter 2 is based on the theoretical background. Starting from the introduction of short wavelength technological domain and light-matter interaction in the VUV spectral region, different important concepts relevant to the work presented in this thesis are discussed. Some of the important topics, covered in this chapter are Fresnel equations, Brewster angle, optical constants, optical anisotropy, methods to retrieve the optical constants.

Chapter 3 is about a brief overview of the structure and properties of graphene with more emphasis on the optical properties of graphene in the light of the literature review.

Chapter 4 is about the experimental activities carried out to achieve the research objectives. Brief descriptions of the experimental setups, experimental activities and methods of optical and

structural characterizations of graphene (1LG and 3LG) and SiO_2 samples are discussed in this chapter.

Chapter 5 this chapter is about the detailed investigation of optical properties (optical constants, ellipsometric parameters, etc.) of SiO_2 with the main focus on the technique to find out the reliable values of optical constants of SiO_2 by implementing the tabletop polarimetric setup. Moreover, ellipsometric parameters (phase shift and ratio) of 1LG sample was also measured and compared with that of the bare substrate (SiO_2/Si) in this chapter.

Chapter 6 is about the detailed optical investigations of the 1LG, and 3LG samples at the VUV spectral region. The optical performance of the graphene samples over the dielectric substrate (SiO_2) was studied and reported in terms of reflectance, Brewster angle, 'effective optical constants' corresponding to the 'effective thickness' of graphene layers and optical anisotropy of graphene at hydrogen Lyman alpha spectral line. Reliability of the retrieved optical constants was demonstrated qualitatively by SDR analysis.

Chapter 7 is about the experimental activities related to the time-resolved colliding plasma spectroscopy. The first part of this chapter is based on the brief introduction and motivation of LPP and CLPP and their use in the different technological domains. Then brief description of the experimental setup, the experimental procedure to generate the stagnation layer at the collision front of two colliding plasmas and its time-resolved spectroscopy is presented. Then the results of the time-resolved plasma spectroscopy of Al-Al and Al-Si with respect to two geometrical configurations of the target (i.e., flat and 90° wedge) are discussed along with analysis in terms of the time evolution of different ion states and electron number density.

Chapter 8 is about the overall conclusions of the Ph.D. research work presented in this thesis along with future aspects and directions.

Chapter 2. Theoretical Background

2.1 Introduction to VUV Spectral Region

The electromagnetic spectrum is described by the electromagnetic wave equation, which is valid for the whole electromagnetic spectrum. The materials behave differently with photons of different regions of the spectrum because of the different photon energy associated with different spectral regions. So the electromagnetic spectrum is divided based on its interaction with the material. Moving from the low energy (infrared) towards higher energies (UV, EUV, soft x-ray), some interesting phenomena (e.g., photoionization of atoms, excitation of molecular vibrations and electron transitions) occurs. Each phenomenon has distinctive resonances, exclusive for every material, which allows to establish many metrology techniques to characterize matter using electromagnetic radiations. Moving towards the lower wavelengths in the electromagnetic spectrum beyond 200 nm even dielectrics as well as air shows absorbance, which necessitates the vacuum for the propagation of the electromagnetic wave. Because of this fact, the electromagnetic spectrum beyond 200 nm down to 10 nm called Vacuum Ultraviolet (VUV) [19]. The scientific community further divided the VUV spectral regions into subgroups (FUV, EUV, and soft x-rays) based on its behavior with materials. e.g., the last transparent material found in nature is LiF, which starts absorbing beyond 100 nm, so the region from 200- 100 nm called FUV (Far ultraviolet) or simply VUV. There are no sharp boundaries between the subgroups of VUV spectral region, so the different conventions were adopted by various groups, e.g., astronomy people referred EUV spectral region 10 nm to 91.2 nm (photoionization of the hydrogen atom) [20] some researcher referred EUV 5 nm to 40 nm [1]. Figure 2.1 shows the different regions of the electromagnetic spectrum divided into groups and their associated names.

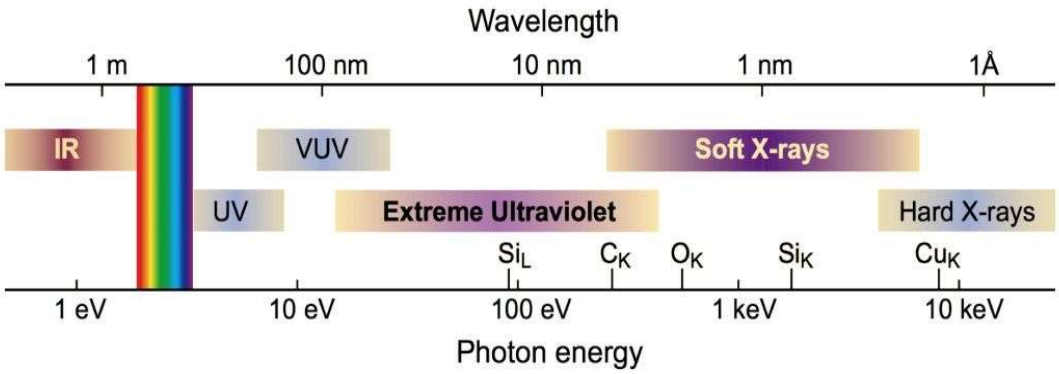

Figure 2.1: Electromagnetic spectrum showing different spectral regions [1].

A detailed description of the EUV and soft x-ray physics and applications are mentioned in a well-known book of David Atwood. Here we will present the short description of this spectral region and some physical phenomena's associated with it. This region of the electromagnetic spectrum is very important because of two of its characteristics i.e.

- E.M radiation energy is comparable with the binding energies of the core electrons of atoms
- The associated wavelength is small enough as the atomic dimension.

These characteristics make this spectral region very important to study the fundamental physical and chemical properties of the materials. For example, as mentioned earlier plenty of resonances in EUV region make it suitable for the development of metrological tools with higher chemical and elemental sensitivity. Moreover, the spectral resolution of EUV radiation is much higher than visible light, which make it suitable for microscopy and lithography advancements. Off course one of the achievements of this spectral region is the realization of EUV lithography which works at 13.5nm.

2.2 EUV-VUV Radiation Sources

VUV radiation is generally emitted from the solar corona. There is number of ways to generate VUV radiation artificially. There are three main types of the VUV sources, i.e. synchrotron light sources, high harmonic generation sources, and hot plasma emissions. At synchrotron radiation facilities, the radiation is emitted by accelerating relativistic electrons through a periodic sequence of the magnetic field; the commonly used assemblies to produce synchrotron radiation are bending magnets, undulators, and wigglers [19][1]. A synchrotron is a comprehensive facility consist of

different types of electron accelerators and huge electron storage ring in which electron moves in circular orbits. The generated radiation is projected at a tangent to the ring and used in experimental stations on different "beamlines". Their application is limited to mainly scientific research because of high maintenance cost. Free-electron lasers (FEL) works on the same physical principle. The use of synchrotron radiations (VUV- soft x-ray) produced a significant advancement in the scientific research. At the laboratory scale, the EUV radiations are most commonly produced by hot plasma emission in two ways from laser-produced plasmas (LPP), and Discharge produced plasma. In LPP a high irradiance laser is focused on the target, as a results the target material is heated and vaporize or sputter. The free electrons released from the ionized target, collide with each other and with ionized atoms, this process creates plasma, The created plasma depend on laser intensity, laser wavelength, pulses duration, focusing lens, and the target material [21]. There are some issues related to the LPP, e.g., besides photons, plasma generates a flow of ions and particles, damaging and contaminating the primary optics[22].The EUV emission can also be achieved in discharged produced plasma (DPP), in which a high-voltage pass through the working gases corresponding to the desired spectral emission. DPP sources are based on a high-current discharge within a working gas (Xe, Ar, Kr, O2, N2, D2, etc.).

2.3 EUV Light-Matter Interaction

In the EUV spectral region, almost all material absorbs the radiations. The reason behind the absorption in short wavelength is because the radiation interacts with the electron in the atom. The absorption phenomena occur when the incoming photon has energy equal to the occupied and empty energy levels in the material. If the incoming photon has energy higher than the binding energy of the electron, the material becomes ionized because of the ejection of the electron from the outer shell. When the material is in the excited or ionized state, it tends to relax, and the electron jumps to lower energy state by emitting the characteristic photon or some time electron. These photons and electrons carry essential information about the material or atom, and these are the basis of different spectroscopic techniques, e.g., XPS, fluorescence spectroscopy, NEXAFS, etc.

The light-matter interaction in the EUV spectral region is governed by two main phenomena (light absorption and scattering). The EUV interaction with matter can be explained by two well-known models, i.e., the photo absorption model and coherent scattering model.

If the incident photon has energy less than the ionization energy of atoms, the normally occurring process is the coherent scattering [1]. Consequently, the interaction of EUV radiation with matter can be described by the electron-photon interactions model through the concept of scattering cross-sections of particles by the following relation:

$$f^o(\omega) = f_1^o(\omega) + if_2^o(\omega) \tag{2.1}$$

where f_1^o and f_2^o are the atomic scattering factors of the atom associated with the reflection and absorption, respectively.

Interaction of any material with the electromagnetic radiation can be expressed in terms of its optical constants (refractive index) although these are not constants but depends on the incident radiation wavelength. Because of the fact that every material absorbs EUV radiation so their refractive index is a complex number and can be expressed as below.

$$\bar{n} = 1 - \delta + i\beta = n + ik \tag{2.2}$$

Where δ and β, or equivalently n and k, are the optical constants. In the EUV, the refractive index (n) can be described in terms of the atomic scattering factors f_1^o and f_2^o as [1]

$$\overline{n} = 1 - \delta + i\beta = n + ik = 1 - \frac{n_a r_e \lambda^2}{2\pi} f^o(\omega) \tag{2.3}$$

Where n_a is the atomic density per unit volume, and λ is the wavelength of the EUV radiation and r_e is the classical electron radius which is defined as

$$r_e = \frac{e^2}{4\pi\varepsilon_o m_e c^2} = 2.82\text{x}10^{-15} m \tag{2.4}$$

$$\delta = \frac{n_a r_e \lambda^2}{2\pi} f_1^o \tag{2.5}$$

$$\beta = \frac{n_a r_e \lambda^2}{2\pi} f_2^o \tag{2.6}$$

These mathematical expressions indicate essential features of light-matter interaction in the EUV spectral region. The real part of the optical constants (n), responsible for the refraction of light is smaller than that compared to visible and lower energy regions. The absolute value of optical constants decreases with increasing photon energy. Figure 2.2 shows the variation of the real part of the optical constants (n) across the electromagnetic spectrum, associated with resonances (ω) at each region. Because the wavelength becomes short so the nanoscale imperfections or nanoscale structural changes on films or coatings turn out to be more critical. These imperfections affect the performance entirely in the case of EUV [3].

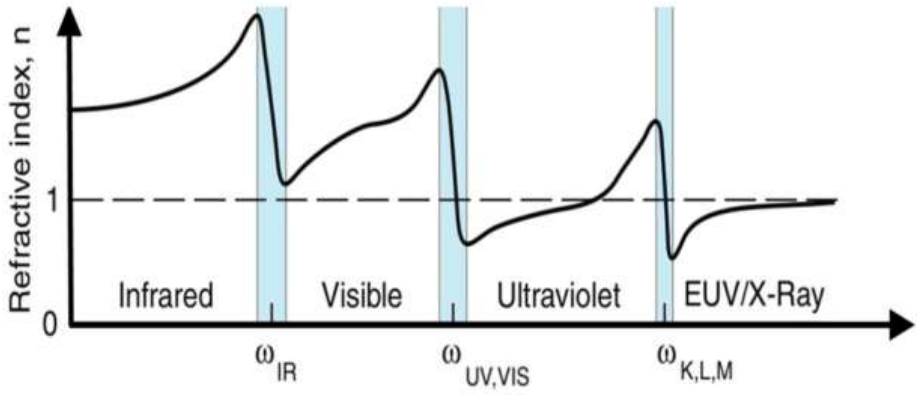

Figure 2.2: Variation of the real part of the refractive index in the electromagnetic spectrum; showing abrupt variations around the resonances, and refractive index tendency is towards unity for very short wavelengths [1].

In semiconductors or dielectrics, there is no absorption if the photon energy is less than the bandgap. The bandgap is the barrier between the transmittance to the absorption region of the material. In the case of metals, valence and conduction bands overlap; the loosely bound electrons i.e., conduction electrons, are shared by all atoms. These are responsible for the optical properties of metals, i.e., high reflectivity and absorptive behavior.

2.4 Electromagnetic Wave and The Optical Constants

The propagation of the electromagnetic wave through any material/ medium is dependent on optical constants of the material. As the optical constants are the fundamental properties of the material, it is vital to understand the wave function of the electromagnetic wave in terms of optical constants of the material. Let us consider the plane wave equation associated with the electromagnetic spectrum is

$$E = E_o \exp\left[-i\left(\omega t + k \bullet r\right)\right] \tag{2.7}$$

Where k is the wave vector, ω is the angular frequency, r is the position vector in space, and E_0 is the initial amplitude of the wave. The relationship between the wavenumber k and refractive index is as follow

$$\frac{\omega}{k} = \frac{c}{\overline{n}} \tag{2.8}$$

Where c is the speed of light in vacuum, and we know that the refractive index for the absorptive material is expressed as

$$\overline{n} = 1 - \delta + i\beta \tag{2.9}$$

So putting the value of the refractive index, we get wave vector

$$k = \frac{\omega}{c}\left(1 - \delta + i\beta\right) \tag{2.10}$$

As a result of inserting the value of the wave vector in eq. (2.7) we get

$$E = E_o \exp\left[-i\left(\omega t + \frac{\omega}{c}\left[1 - \delta + i\beta\right]r\right)\right] \tag{2.11}$$

Now we have the plane wave equation which contains the optical constants as propagating factor. By further simplifying

$$E = E_o \exp\left(-i\left(\omega t - \frac{\omega}{c}r\right)\right)\exp\left(-i\left(\frac{\omega}{c}r\delta\right)\right)\exp\left(-\left(\frac{\omega}{c}r\beta\right)\right) \tag{2.12}$$

$$\omega = 2\pi f$$

$$f = \frac{c}{\lambda}$$

$$E = E_o \underbrace{\exp\left(-i\omega\left(t-\frac{r}{c}\right)\right)}_{term1} \underbrace{\exp\left(-i\left(\frac{2\pi}{\lambda}\delta\right)r\right)}_{term2} \underbrace{\exp\left(-\left(\frac{2\pi}{\lambda}\beta\right)r\right)}_{term3} \tag{2.13}$$

We have splitted the wave function into three terms in which term1 correspond to wave propagation in a vacuum, term2 correspond to the phase shift (i.e. $(\frac{2\pi\delta}{\lambda})$ and term3 related to the absorption of radiation in the medium. [1]

The imaginary part of the refractive index, i.e. (β) extinction coefficient is directly related to the absorption coefficient of the medium through the relation

$$Absorption = \alpha = \left(\frac{2\pi}{\lambda}\beta\right) \tag{2.14}$$

The real part of the refractive index (δ) is associated with the phase shift through relation

$$phase\ \text{diff} = \Delta\varphi = \left(\frac{2\pi}{\lambda}\delta\right)\Delta r \tag{2.15}$$

Δr the propagation distance within the medium. From these relations, it is evidenced that the optical constants strongly affect the propagation of electromagnetic wave within the medium. The physical phenomena (reflection, transmission, and refraction) associated with the interaction of the EM wave between two media of different refractive indices are explained in the following section.

2.5 Reflection and Transmission of Electromagnetic Wave

The electromagnetic waves traveling in space interact with medium or material, some physical phenomena like reflection, transmission, and refraction occur at the interfaces between two media having distinct optical constants. These phenomena can be explained by the Fresnel equations. Augustin-Jean Fresnel in 1823 derived these equations, and these are considered one of the most fundamental findings of classical optics [23]. The Fresnel equations are the correlation of the incident light wave parameters (e.g., amplitudes, phases, and polarization) to the transmitted or reflected waves at the interface between two media of different refractive indices . These are

relevant to fundamentally all fields of optical design, e.g., lens design, imaging, lasers, optical communication, spectroscopy, and holography.

Here we will describe Fresnel's equations briefly without going in detailed derivation. Let us consider a plane wave impact on a plane boundary from medium with refractive index (n_o) to the medium with refractive index (n_1). At the boundary the electric field vector associated with the incident light wave can be decomposed into two components, i.e. one in the incidence plane, which is called p-polarization or transversal magnetic (TM), and the other in the perpendicular plane, which is referred to as s-polarization or transversal electric (TE) as shown in Figure 2.3.

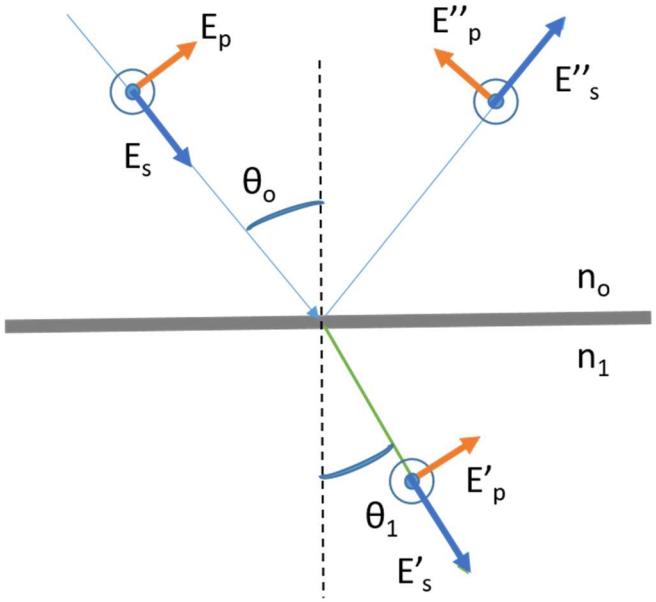

Figure 2.3: Coordinate system showing the E vector of the plane wave reflected and refracted at the boundary between two medium of different refractive indices [24]

The Fresnel reflectance coefficient at the interface is defined as the ratio of reflected electric field intensity to the incident electric field intensity, and similarly, transmittance Fresnel coefficient is defined as the ratio of transmitted or refractive electric field intensity and incident electric fields intensity.

By considering the above coordinate system, the Fresnel amplitude reflection coefficients for a single interface can be written as

$$r_s = \frac{E_s^{"}}{E_s} = \frac{n_o \cos\theta_o - n_1 \cos\theta_1}{n_o \cos\theta_o + n_1 \cos\theta_1} \tag{2.16}$$

$$r_p = \frac{E_p^{"}}{E_p} = \frac{n_1 \cos\theta_o - n_o \cos\theta_1}{n_1 \cos\theta_o + n_o \cos\theta_1} \tag{2.17}$$

The amplitude transmission coefficients are

$$t_s = \frac{E_s^{'}}{E_s} = \frac{2n_o \cos\theta_o}{n_o \cos\theta_o + n_1 \cos\theta_1} \tag{2.18}$$

$$t_p = \frac{E_p^{'}}{E_p} = \frac{2n_o \cos\theta_o}{n_1 \cos\theta_o + n_o \cos\theta_1} \tag{2.19}$$

The Fresnel amplitude reflection and transmission coefficients can be rewritten in the form of only angle of incidence and refraction with the help of Snell's law as follows[25]

$$\frac{\sin\theta_o}{\sin\theta_1} = \frac{n_1}{n_o} \tag{2.20}$$

to eliminate n_0 and n_1 from reflection and transmission coefficients

$$r_s = \frac{\sin(\theta_o - \theta_1)}{\sin(\theta_o + \theta_1)} \tag{2.21}$$

$$r_p = \frac{\tan(\theta_o - \theta_1)}{\tan(\theta_o + \theta_1)} \tag{2.22}$$

$$t_s = \frac{2\sin\theta_1 \cos\theta_o}{\sin(\theta_o + \theta_1)} \tag{2.23}$$

$$t_p = \frac{2\sin\theta_1 \cos\theta_1}{\sin(\theta_o + \theta_1)\cos(\theta_o - \theta_1)} \tag{2.24}$$

For non-absorbing materials the intensity reflection coefficients Rs and Rp are simply the squares

$$R_s = \left|r_s^2\right| = \left|\frac{\sin^2(\theta_o - \theta_1)}{\sin^2(\theta_o + \theta_1)}\right| \tag{2.25}$$

$$R_p = \left|r_p^2\right| = \left|\frac{\tan^2(\theta_o - \theta_1)}{\tan^2(\theta_o + \theta_1)}\right| \tag{2.26}$$

For normal incidence

$$R_s = R_p = \frac{\left(n_o - n_1\right)^2}{\left(n_o + n_1\right)^2} \tag{2.27}$$

The refractive index is a complex quantity in case of absorbing materials. In this case the angle of refraction is complex, which makes difficult calculations for reflection and transmittance. For absorbing materials, the amplitude reflection coefficients are written below

$$r_s = \left|r_s\right| e^{i\delta_s} \tag{2.28}$$

$$r_p = \left|r_p\right| e^{i\delta_p} \tag{2.29}$$

where$|r_s|$ and $|r_p|$ are the magnitudes of the reflectance and δ_s and δ_p are the phase changes on reflection. The intensity reflection coefficients are calculated as.

$$R_s = r_s r_s * \tag{2.30}$$

$$R_p = r_p r_p * \tag{2.31}$$

2.6 The Brewster Angle

Brewster angle for the dielectric materials is the angle where the p-polarization component of incident light is not reflected or have reflection minima. At Brewster angle, the refracted and reflected rays are 90º to each other and p–polarized wave is totally refracted into the second medium. It is also called the polarizing angle because of the fact that at this angle only s-component of the polarization reflected for the wave with (arbitrary elliptic polarization, unpolarized or partially polarized light). This phenomenon is technologically important and is

used in Brewster windows for gas lasers, for photography and photographic glasses. The Brewster phenomenon in dielectrics can be explained with the interaction of E.M wave with the electric dipole radiation at the interface of media. If the incidence angle of the p-polarized light wave is not equal to the Brewster angle. In this case, the electric dipole radiation occurs from the atoms located near the interface, and only light waves that satisfy the law of reflection (i.e., incidence angle = reflected angle) will be reflected.

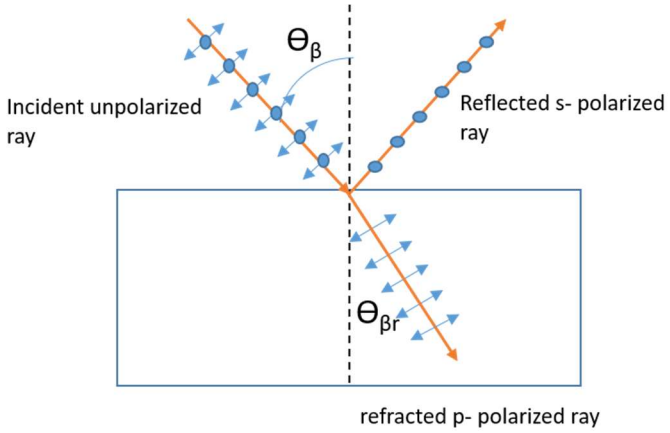

Figure 2.4 Schematic of Brewster phenomena

This occurs because the propagation direction of the reflected light and the oscillatory direction of the electric dipoles are not parallel. However, if the incidence angle is the Brewster angle, in that case, no p-polarized light wave reflected because the propagation direction of the reflected light wave is parallel to the oscillatory direction of the electric dipoles. This is the reason for non-absorbing materials the p- polarized light has zero reflection, i.e. $R_p = 0$ at θ_β. In case of absorbing material, the p- polarized reflection has non zero minima; in such cases, it is called pseudo-Brewster angle.

In Figure 2.4 dot represent s- polarized ray and arrow represents the p- polarized ray. The well-known formula for Brewster angle is retrieved from Snell law in case of dielectrics is.

$$\tan \theta_\beta = \frac{n_1}{n_o} \tag{2.32}$$

Where θ_β is the Brewster angle and n_1 is the refractive index of a dielectric medium, and n_o is the refractive index of air or vacuum. However, for EUV spectral region even dielectrics have non-

zero reflectivity minima at this angle, in this case, it is called pseudo-Brewster angle. The eq. 2.32 is also known as Brewster's law.

2.7 Techniques to Determine Optical Constants in VUV Spectral Region (Overview)

For the design of optical elements, and optical modeling, accurate information about the optical constants is mandatory. Hence, several techniques for the determination of optical constants have been developed. Palik in his handbook [26] mentioned the detailed overview of the techniques to find the optical constants of materials. We summarize in the following section,few common techniques for the determination of optical constants of materials in the short wavelength region of the E.M spectrum.

2.7.1 Angular Reflectance Measurement

In this technique, the angular reflectance measurements are performed for various angles ranging from near normal to grazing incidence at a fixed wavelength. The measured reflectance used to fit with the Fresnel's reflectance coefficients by considering the suitable optical model. In this technique, both (n) and (k) can be calculated using Fresnel equations. Many scientists adopted this approach of finding the optical constants. This technique has been described more extensively in the references [27][26]. The suitable optical model for the fitting analysis is critical to get reliable optical constants data. Especially for the short wavelength region, the surface roughness can affect considerably the optical properties of the material, so the surface properties should be accounted for in the optical model. Some examples of the use of the reflectance-versus-angle method are given in[28],[29], [30]. This technique was used extensively in this thesis for optical constants extraction.

2.7.2 Transmittance Over a Large Spectrum

In this technique, the transmittance of various thickness of the material is measured over a wide spectral range. Also, the transmittance measurement of the bare substrate needs to be measured in this technique which is required in the beer lambert law. Value of the extinction coefficient at each spectral line obtained using the Beer-Lambert law as follow

$$T_i = T_s \exp(\frac{4\pi k d_i}{\lambda}) \tag{2.33}$$

T_i corresponds to the transmittance of the sample with thickness di and T_s is the transmittance of the bare substrate, d_i the film thickness. Using the linear fit of the normalized transmittance vs. the film thickness, k value can be determined, the reflectance of the sample is neglected here. After retrieving the value of k, n value can be determined by using the Kramer Kroning relation. This technique has some advantages over reflectance, e.g., effect of any possible contamination can be minimized, and the dependence on roughness is much smaller, which is a significant advantage at short wavelengths. But the problem in this technique is the lack of transparent substrates in EUV. This issue can only be solved by preparing self-supporting thin film samples (membranes) that support the material to be investigated, which is not always straightforward [31]. In the literature, this technique was also adopted by directly depositing the material on the detector [32]. In the pioneering work by Hagemann et al. [33], several materials were characterized, mostly metals using this technique.

2.7.3 Spectroscopic Ellipsometry

Spectroscopic ellipsometry (SE) is a very useful and effective method developed for optical and structural analysis of materials and thin films. Ellipsometry measures the change in the state of polarization of the incident incoming ray upon reflection from the sample surface. The ellipsometric measured parameters are expressed as follow [34]:

$$\tan\psi = \frac{r_p}{r_s} \tag{2.34}$$

$$\Delta = \delta_p - \delta_s \tag{2.35}$$

where ellipsometric parameters Ψ and Δ are correspond to the intensity ratio of the two orthogonal components of the electric field vector and the phase difference introduced by the sample under test.

Using the measured ellipsometric parameters, i.e., both (n) and (k) values of the material can be determined by choosing an appropriate optical model. Because of the lack of the availability of phase retarders and wideband polarizers for short wavelength, only few ellipsometers available which works in this spectral region. Hilfiker et al. [34] discussed the use of EUV-VUV ellipsometry. Moreover, some ellipsometers connected to the synchrotron beamlines are also

getting available for measurements [35]. We have also an EUV–VUV ellipsometer developed at IFN Padova [36], [37] that have been used some of the experimental activities presented in this thesis.

2.8 Reflection and Transmission of Light by Anisotropic Materials

Crystals are the periodic arrangement of atoms in an ordered geometrical pattern. The crystal structure based on this ordered arrangement is the characteristic of the crystal. Based on the crystal structure, the atoms are characterized in seven distinct crystal systems [38] (e.g., cubic, trigonal, tetragonal or hexagonal, orthorhombic, monoclinic, or triclinic). Based on reflection and transmission of light through the crystals, it can be divided into two main categories, i.e., Isotropic crystals and anisotropic crystals. Isotropic crystals are those crystals in which the E.M. light propagation is independent of propagation direction within the medium. However, the light reflection and transmission in the anisotropic materials is different than from isotropic materials. Optical response changes with the orientation of the samples in case anisotropic materials. As a result, the dielectric tensor or three-dimensional index ellipsoid used to describe the optical constants of anisotropic materials. To understand the anisotropic properties of the materials, dielectric tensor associated with material needs to discussed first.

2.8.1 Dielectric Tensor

Electromagnetic plane-wave propagation is determined by the dielectric tensor, which links the displacement vector (D) and the electric field vector (E). In the case of isotropic material, E and D are parallel with each other and can be expressed as follows.

$$D = \epsilon E \tag{2.36}$$

$$\epsilon = \epsilon_0 \epsilon_r \tag{2.37}$$

Where ϵ is permittivity, ϵ_0 permittivity of free space and ϵ_r is the relative permittivity [34].

In an optically anisotropic material, the propagation of the electromagnetic wave depends on the orientation of the electric field vector and axial directions of the crystal. As a consequence, D will not always be oriented in the direction of E, and related to each other as follows

$$\begin{pmatrix} D_x \\ D_y \\ D_z \end{pmatrix} = \begin{pmatrix} \varepsilon_{xx} & \varepsilon_{xy} & \varepsilon_{xz} \\ \varepsilon_{yx} & \varepsilon_{yy} & \varepsilon_{yz} \\ \varepsilon_{zx} & \varepsilon_{zy} & \varepsilon_{zz} \end{pmatrix} \begin{pmatrix} E_x \\ E_y \\ E_z \end{pmatrix} \tag{2.38}$$

Because of the symmetry of the dielectric tensor, it has only six instead of nine independent components. By properly defining the coordinate system in such a way that by rotation, the symmetric tensor transforms into diagonal form with diagonal elements as principal dielectric constants. The axes of this coordinate system are known as principal axes. In such a case, D can be written as [34]

$$\begin{pmatrix} D_x \\ D_y \\ D_z \end{pmatrix} = \begin{pmatrix} \varepsilon_{xx} & 0 & 0 \\ 0 & \varepsilon_{yy} & 0 \\ 0 & 0 & \varepsilon_{zz} \end{pmatrix} \begin{pmatrix} E_x \\ E_y \\ E_z \end{pmatrix} \tag{2.39}$$

Whereas principle permittivities are equivalent to the square of the refractive index and the above equation can be represented as

$$\begin{pmatrix} D_x \\ D_y \\ D_z \end{pmatrix} = \begin{pmatrix} n_x^{\,2} & 0 & 0 \\ 0 & n_y^2 & 0 \\ 0 & 0 & n_z^2 \end{pmatrix} \begin{pmatrix} E_x \\ E_y \\ E_z \end{pmatrix} \tag{2.40}$$

So based on principle permittivities, isotropic crystals can be defined as those crystals having all the three permittivities' equal, i.e., $\varepsilon_{xx} = \varepsilon_{yy} = \varepsilon_{zz}$ example of such crystals is cubic crystals, e.g., Diamond. However, anisotropic crystals can be further grouped into two categories based on their dielectric permittivities i.e. Biaxial anisotropic crystal (crystals whose all three principle permittivities are different) and Uniaxial anisotropic crystal. (crystals whose one principle permittivity is different than other two)

2.8.2 Uniaxial Anisotropic Crystals

Uniaxial anisotropic crystals have two equal principal permittivities, $\varepsilon_{xx} \neq \varepsilon_{yy} = \varepsilon_{zz}$. Any incident light upon refraction split into two rays (linearly polarized in orthogonal directions) in the uniaxial crystals, as shown in Figure 2.5. The ray which is polarized perpendicular to the principal plane is

called ordinary ray and obeys Snell's law. This ordinary ray propagates in the same direction as if the material is isotropic. The second ray called the extraordinary ray, which is polarized parallel to the principal plane and is called p-polarized.

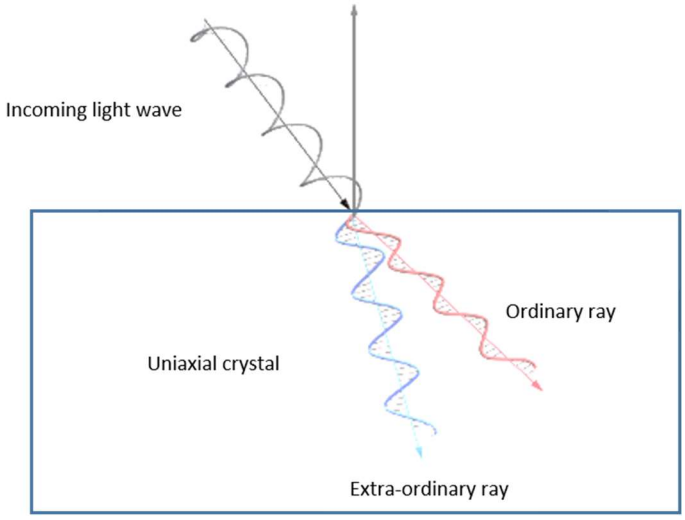

Figure 2.5. EM wave propagation in the uniaxial crystal [39]

Uniaxial crystals have one optical axis, which means in uniaxial crystal the ordinary and extraordinary refraction rays coincide in one direction within the crystal. Trigonal, tetragonal, and hexagonal crystal structures are called uniaxial crystals. Examples of such crystals are Zirconia and Quartz [39].

2.8.3 Optic Indicatrix

Because the refractive index varies with the direction of vibration of light waves for anisotropic crystals, and the refractive index is dependent on the direction of propagation, it is beneficial to represent the refractive index of anisotropic crystals geometrically. The geometric representation of the refractive index is called optic indicatrix, which is the representation of 'n' values for all the directions of vibration of a crystal. The indicatrix is an ellipsoid with the equation. [22][24][40]

$$\frac{x^2}{n_x^2}+\frac{y^2}{n_y^2}+\frac{z^2}{n_z^2}=1 \tag{2.41}$$

The indicatrix lets us find the refractive index as a function of polarization direction of the monochromatic plane waves [41]. Indicatrix is the generalized representation of the refractive index ellipsoid e.g., for isotropic materials, optic indicatrix is a sphere with a refractive index equal

in all directions of propagation. For uniaxial crystals, the indicatrix is an ellipsoid of revolution with two principal axes. For biaxial anisotropic crystals, the indicatrix is an ellipsoid with three principal axes, as shown in Figure 2.6.

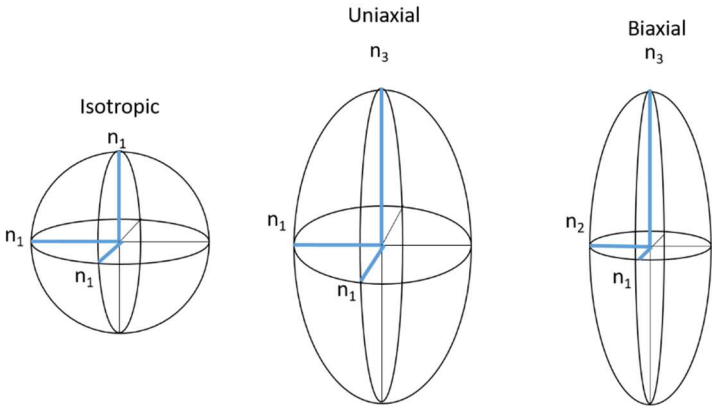

Figure 2.6: Geometrical representation of isotropic (left), uniaxial (center), and biaxial crystals (right).

The equation of the uniaxial indicatrix is

$$\frac{x^2+y^2}{n_o^2}+\frac{z^2}{n_e^2}=1 \tag{2.42}$$

where n_o is the index of refraction for the wave polarized perpendicular to the optic axis and follow the Snell's law, called ordinary ray, n_e is the index of refraction for the wave polarized parallel to the optic axis, called extraordinary ray. The uniaxial crystal is categorized as positive crystal If $n_e > n_o$ and for $n_e < n_o$ it is categorized as negative uniaxial crystal. As the indicatrix of the uniaxial crystal is circularly symmetric about the optic axis, its properties depend on the polar angle which wave makes with the optic axis and does not depends on the azimuthal orientation of wave vector k relative to the x and y-axes.

Chapter 3. Graphene: Brief Literature Overview

The motivation to choose graphene for short wavelength applications is mentioned in detail in chapter 1. This chapter is based on the literature review about the graphene, its historical introduction, structure, growth techniques, oxidation/ corrosion resistive properties, and mechanical properties. An overview of the literature about the optical properties of graphene with special emphasis on its optical constants is also discussed in this chapter.

3.1 Graphene: Historical Introduction

Historically it can be considered that Wallace did the first study on graphene in 1947 in which he used the tight bonding approximation to study the electronic bands of crystalline graphite [42]. Because of some reports and literature, that the semi-metallic phase is unstable in bi- dimensional [43][44], it was believed that the graphene could not exist in free state because it would be too thermodynamically unstable. Graphene described as "academic" material. Many experiments were performed to achieve the monolayer graphene, e.g., under scanning tunneling microscope (STM) monolayer graphene structure was observed, produced by the decomposition of hydrocarbon on Pt (111) surface [45]. A Japanese scientist successfully achieved the thickness of graphite film up to 30 nm by cleaved kish graphite to evaluate the thickness effect of graphite crystals on electrical properties [46] this work inspired the scientific community and in 2004 Novoselov and Geim demonstrated the robust, reliable and practically viable approach for obtaining monolayer graphene. They presented that monolayer graphene can be achieved by repeatedly peeling highly oriented pyrolytic graphite (HOPG) [47]. This approach is called scotch tape or mechanically exfoliation method, which opens up great opportunities and stimulated scientists to study the structure and physical properties of graphene.

Geim and Novoselov received the Nobel prize in Physics in 2010 for innovative experiments concerning the 2D Graphene material. This breakthrough in graphene has driven a tremendous amount of research on graphene because of its incredible features. Since its discovery in 2004, the number of scientific publications of graphene are increasing year after year.

Graphene is the single horizontal layer of carbon atoms strongly bonded as 2D honeycomb lattice. Graphene is the mother block for all graphitic materials, as depicted in Figure 3.1 [48]. Graphene can be rolled into 1D nanotubes, wrapped up into 0D fullerenes, or stacked into 3D graphite [49]

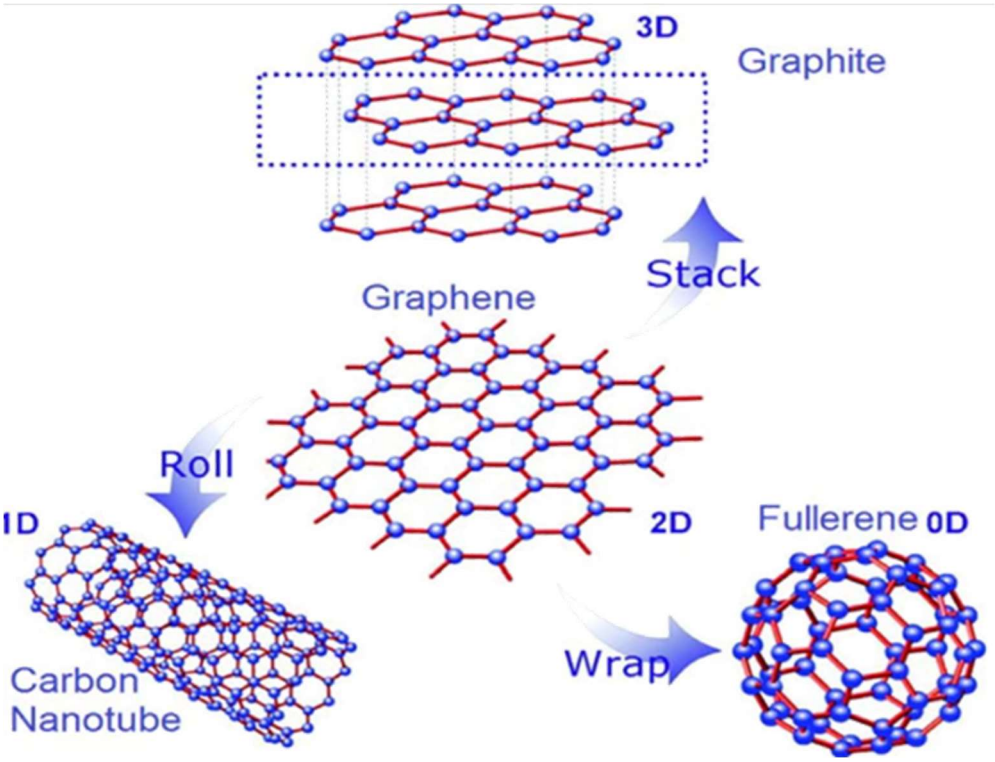

Figure 3.1: Graphene as the building block of other allotropes of carbon [48].

3.2 Structure of Graphene

Carbon has different allotropes. Graphite is one of the allotropes of carbon, made up of very tightly bonded carbon atoms organized into a hexagonal lattice. Graphene is a single atom thick basic building block of graphite. Its atomic thickness (0.345nm) and sp^2 hybridization makes graphene unique material with extraordinary properties like its conductivity, strength, thermal conductance, etc. The electronic configuration of 6 electrons in carbon atom is $1s^2 2s^2 2p^2$ ($1s^2 2s^2 2Px^1 2Py^1 2Pz^0$) out of which two electrons are present in the inner shell and four in the outer shell. In graphene, there are four orbitals for bonding, i.e., three sp^2 and one pz. Every carbon atom is bonded with three of its neighboring atoms through strong in-plane σ-bonds, formed from sp^2– hybridized orbitals. The interatomic length of the resultant covalent σ-bond is short ~ 1.42 Å, which makes graphene much stronger than the sp3 hybridized carbon-carbon bonds in diamonds. The out of plane unhybridized pz orbitals overlap to form π-bonds. The unit cell of graphene contains two π orbitals that disperse to form two π-bands. Half-filled π band is responsible for zero bandgap

between valence and conduction band which permits the free moving of the electrons. Weak van der Wal interaction between the layers of graphene in case of bilayer and multilayer is because of π-,bond.

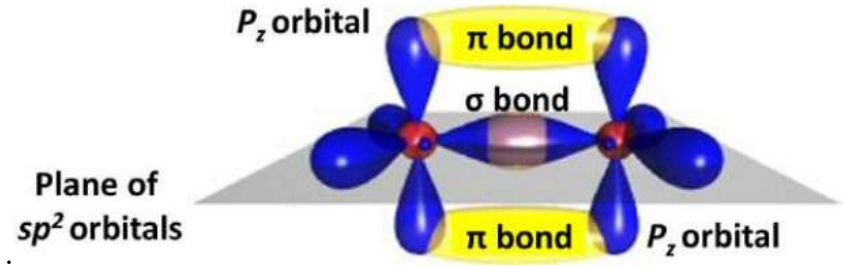

Figure 3.2: Sigma (σ) and pi (π) bonds in graphene schematic representation [8].

The carbon atoms form the hexagonal rings in the graphene and look like the honeycomb structure. This honeycomb lattice is not the bravais lattice because the neighboring atomic sites are not equivalent [50], [51] as can be seen Figure 3.3. Carbon atom located on the A sublattice and B sublattice have three nearest neighbors, as shown in Figure 3.3 (d). The a_1 and a_2 denote the real space lattice vectors in graphene. The distance between nearest-neighbor carbon atoms is 0.142 nm.

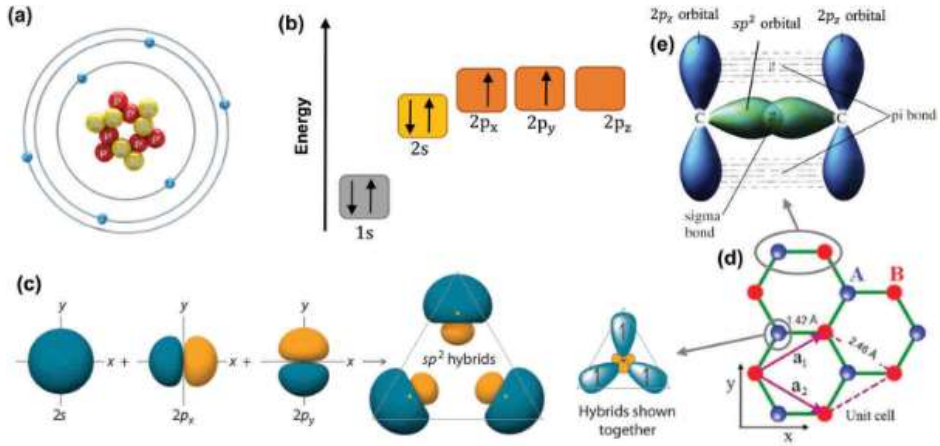

Figure 3.3: (a)Atomic structure of carbon atom (b) Energy levels of the outer electron in carbon (c) sp^2 hybridization (d) crystal lattice of graphene (e) sigma and π bond formed by sp^2 hybridization. (adopted from [10]).

3.3 Graphene Synthesis Techniques

There are several methods used for the synthesis of the graphene, some of the common methods are chemical vapor deposition (CVD), mechanical exfoliation, chemical synthesis, epitaxial growth on silicon carbide (SiC) [52]. Apart from these methods, many other methods were adopted

to get the graphene, e.g., unzipping nanotubes and pyrolysis of sodium ethoxide,[53] but these techniques are not well optimized so far. The most widely used method for synthesis of single-layer and multilayer graphene is the CVD, because of its capability to produce large scale high-quality graphene [54][55]. There is a huge amount of research focused on producing high-quality large-area graphene films. Different synthesis techniques that have been adopted so far can be divided into two main categories, i.e., top-down and bottom-up approach. The classification of techniques under these categories are mentioned in Figure 3.4.

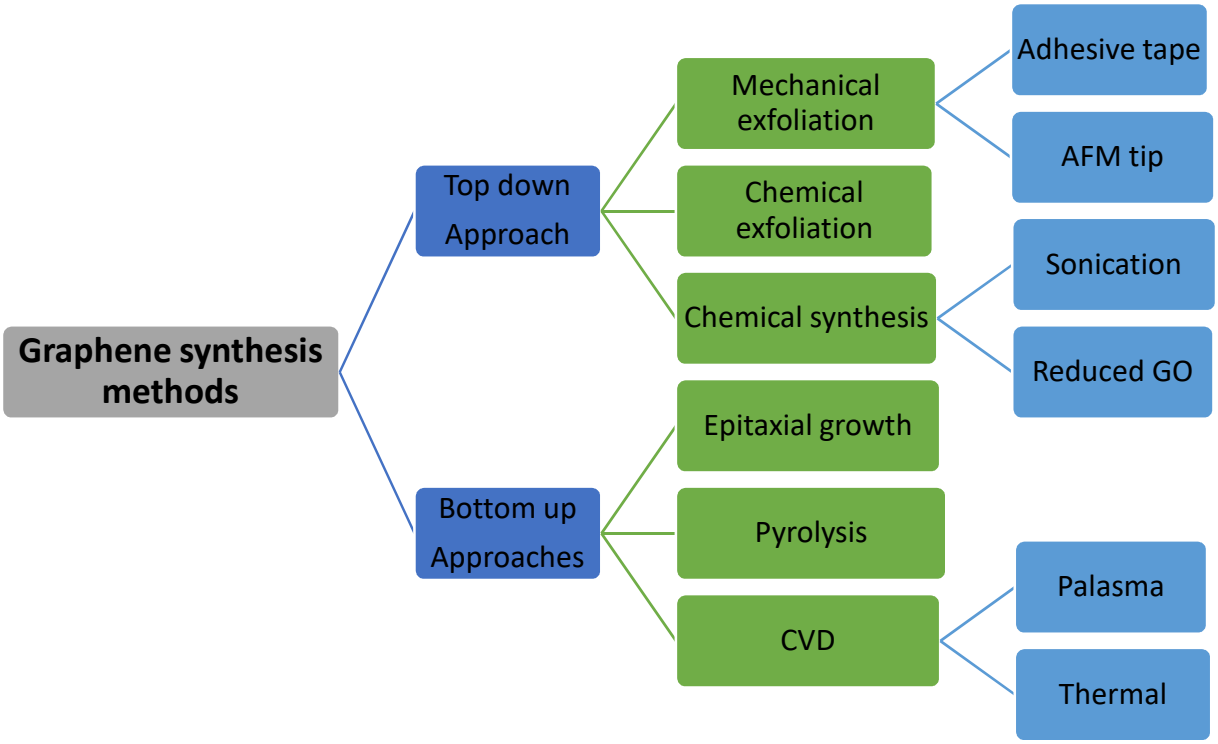

Figure 3.4: A schematic diagram represents the different types of classification for the methods of preparation of graphene [14].

3.4 Graphene: Corrosion and Oxidation Resistant Properties

An interesting and appealing property of the graphene is its ability of protection against corrosion and oxidation of the underlying substrate. However, it also proved that the ability of graphene as a protective coating strongly requires the defect-free sheet of graphene. Apart from the other outstanding electrical, mechanical, and optical properties of graphene, its corrosion-resistant property makes it a suitable and potential material for direct industrial application because of easy to implement procedure. The hexagonal structure of sp^2 hybridized carbon atoms is responsible

for the graphene to act as a shield against corrosion, oxidation and withstand the external forces of the ambient environment. The impermeability of the graphene against the gasses has already been proved by Bunch and co-workers [56], they also show that the graphene as a membrane can withstand the pressure difference of more than one atmosphere. Apart from the impermeability of the graphene, its anti-oxidation properties also proved experimentally by Chen et al. [6]. They validated that the graphene films grown by chemical vapor deposition on metallic substrates Cu and Cu/Ni alloy, protects against oxidation in an air environment. They used SEM, Raman, and XPS analysis to confirm that the metal surface is well protected from oxidation even after heating at 200 °C in air for up to 4 h. In addition to this, it was also shown that graphene provides effective resistance against hydrogen peroxide. Actually the impermeability of the graphene provides the protective barrier layer between the environment and protected metal. It is quite surprising that one atom layer of graphene prevents any oxide formation on the protected metal surfaces. Interestingly, a comparison was carried out between two penny coins (95%Cu/ 5%Zn) protected by graphene and bare one [6]. Both the coins were treated by hydrogen peroxide. The color change of the uncoated penny was observed because of the oxidation while the penny coated by graphene sustains its appearance like the original one, as can be seen in Figure.3.5. Liang et al. [20] also reported the corrosion protection of graphene-coated Cu by electrochemical corrosion tests. Apart from the Cu, corrosion resistant property of graphene also studied on mild steel substrate by S. Sai Pavan et al. [19], they observed the corrosion rate reduction of mild steel coated by 3- layer graphene up to 99%.

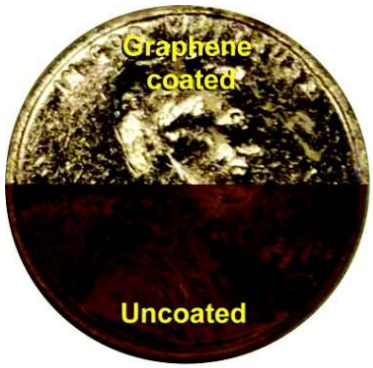

Figure.3.5: Comparison of penny coated and uncoated by graphene after H_2O_2 exposure [6].

However, the non-ideal performance of graphene against corrosion and oxidation is also reported in some literature. This was observed because of the presence of unavoidable defects in the

graphene sheet. In the ref [6], the authors suggested that defects in the graphene sheet mainly located at the grain boundaries, which are responsible for the local oxidation. The failures of graphene as anti-oxidation coating were further highlighted by Schriver et al. [59], through their long-term research. They found that graphene could offer effective short-term oxidation protection, but it played a reverse role over long time scales.

In the technological domain of using graphene as a protective layer/ coating, the most decisive factor is the quality of the graphene sheet. The amount of defects presents on the graphene sheet drastically affects the performance of graphene as a protective coating. However, the pristine hexagonal structure of graphene conforms a perfect impermeable barrier for material protection [60]. The ideal performance of graphene as a protective coating is associated with the defect-free graphene sheet (minimization of grain boundaries, minimization of impurities, large-area growth, etc.).

3.5 Mechanical Properties of Graphene

The exceptional mechanical properties of Graphene are because of the stability of the hexagonal lattice of the sp^2 bonded carbon atoms, which provides opposition to the in-plane deformation. Because of this fact, the defect-free sheet of graphene has been confirmed as the most durable material. Hone et al. [61] measured the elastic properties and intrinsic breaking strength of free-standing monolayer graphene membranes by nano- indentation in an atomic force microscope. They reported the intrinsic strength of the monolayer membrane to be 42 N/m, which equates to .an intrinsic strength of 130 GPa (highest ever value reported for real material). The experimental value of the elastic stiffness reported was 340 ± 50 N/m and Young's modulus of E = 1.0 ± 0.1 TPa, [61] assuming an effective thickness of 0.335 nm.

3.6 Optical Properties of Graphene

Majority of the research on the graphene has been focused on its remarkable electronic properties (conductivity) and mechanical strength. Apart from these, graphene possesses exceptional optical and optoelectronic properties that are suitable for many optoelectronic device applications [62], [63]. As discussed earlier, the σ -bond is responsible for most of the structural reliability and mechanical strength of graphene, whereas the π- bond is responsible for electronic and optical properties. The interesting interaction of graphene with electromagnetic radiation is because of the

exceptional band structure of graphene which is responsible for the two-dimensional confinement of the electrons. Graphene possesses the simplest band structure with zero bandgap. In the band structure of graphene, the conduction band and the valence band meet each other at a common point called Dirac point. Despite having an extremely small thickness of one atom, the graphene shows light absorption of 2.3% in the visible region [64] which is the evidence of strong light-matter interaction of graphene. Moreover, it is observed that the more graphene layers stacked together show more absorption of light, e.g., shown in the Figur.3.6 that for bilayer, the absorption is reported 2x (2.3%). [64]. Furthermore, the transmittance (T) of freestanding single-layer graphene can be expressed in terms of the fine-structure constant (α) as follows

$$T = (1 + 0.5\pi\alpha) - 2 \approx 97.7\% \tag{3.1}$$

Where

$$\alpha = \frac{e^2}{4\pi\varepsilon_o c} = \frac{G_o}{\pi\varepsilon_o c} \approx \frac{1}{137} \tag{3.2}$$

and the fixed universal optical conductance G_o is

$$G_o = \frac{2\pi e^2}{4h} \approx 6.08\times10^{-5}\Omega^{-1} \text{ [64]} \tag{3.3}$$

Moreover, the absorption spectrum of graphene is relatively flat for the spectral region (300-2500 nm), except at (~ 270 nm), which is due to the interband transition of the electrons [65][27].

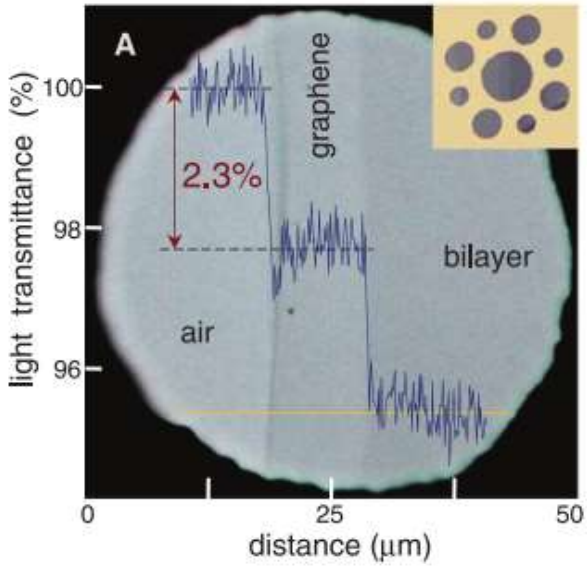

Figur.3.6: Transmittance through a 50 micrometer aperture partially covered by graphene and its bilayer. The line scan shows the intensity of the transmitted white light along the yellow line [64].

Despite being atomically thick, another interesting property of graphene is that it can be detected optically from the color contrast on top of a SiO_2/Si substrate [66] The color contrast of graphene can be adjusted by changing the SiO_2 thickness and switching the illumination wavelength [67] as can be seen in Figure 3.7.

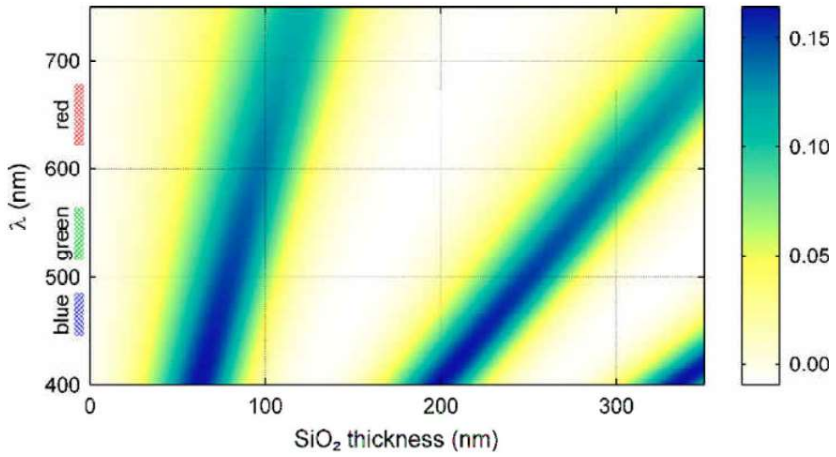

Figure 3.7: Color plot of the expected contrast as a function of wavelength and thickness of SiO_2. The Color grade shows the expected value of the contrast value with white (minimum) and blue (maximum) [67].

3.6.1 The Optical Constants of Graphene

The optical constants of the graphene have been studied extensively in the spectral region ranging from UV-Vis-IR by employing different techniques. However, because of the difficulty in the simultaneous determination of the thickness of graphene and refractive index, still the refractive index values of the graphene are debatable. From the literature, different values of the refractive index have been reported ranging from 2+ i1.1 to 2.69+ i1.6 that have been obtained from different experiments [68]–[72]. In the subsequent part of this section, we will briefly describe the literature review about the optical constants of graphene determined so far.

Bruna et al. [69] determined the optical constants of graphene in the visible region by using experimental reflectance spectra. The optical constants were retrieved by relating their consistency with universal optical conductivity and experimentally measured optical spectra, within the context of Fresnel coefficients calculation. The obtained complex refractive index allows for accurate prediction of the optical behavior of graphene in the visible range, from the two-dimensional limit of single atomically thick, i.e., graphene layer to the bulk limit, i.e., graphite. They used the experimental contrast and theoretical one in order to compare the behavior in case

of their extracted optical constants values in the visible spectral range. The optical constant value reported at 550nm in 3.0+ i1.15.

Gray et al.[71] investigated the optical properties of graphene in the spectral range 190–1000 nm by near-normal incidence reflectance measurements. They measured the reflectivity of graphite flakes having different thickness down to thickness of graphene, deposited on a SiO_2/Silicon substrate. In their study, they assumed that the optical constants are independent of thickness and can be parameterized with five Forouhi–Bloomer oscillators. The parameters of these oscillators and each thickness were fitted simultaneously to all the reflectance data. They reported the fitted thickness of graphene 0.38 nm.

Wang et al. [73] measured the optical properties of graphene in the spectral range 190-1000 nm by the combined use of reflectometry and ellipsometry techniques. The optical properties deduced from the multi-angle, polarized light measurements. They reported that multilayer graphite is a birefringent material with thickness-dependent optical properties.

Kravets et al.[74] also used spectroscopic ellipsometry for graphene on SiO_2(300nm)/Si, and on amorphous quartz. They reported the optical constants retrieved using the variable angle 45°–70° ellipsometry data by numerical inversion for the spectral range 240–750 nm for the amorphous quartz wafer and 240– 1000 nm for SiO_2 (300nm)/Si, assuming a thickness of 0.335 nm.

Weber et al. [72] Used the spectroscopic ellipsometry in combination with a B-spline parameterization to accurately determine the thickness and its Kramer-Kroning consistent optical constants for spectral range 210–1000 nm. They retrieved the thickness of graphene 0.34 nm.

Ni et al. [70] used the contrast spectra to calculate the number of graphene layers. Comparing the experimental contrast spectra with that of the calculated using Fresnel's equations and calculated the optical constants of graphene and reported the value 2.0+ i1.2.

Matkovic *et al*.[75] used imaging spectroscopic ellipsometry in the spectral range (360– 800 nm) to determine the optical properties of exfoliated graphene on a SiO_2/Si substrate. An optical model based on Fresnel coefficient was used to analyze the experimental data. The complex refractive index of graphene was retrieved by inversion of the ellipsometry data with the values of 3.0+ i1.5. They used the Fano line-shape to parameterize the optical properties.

X Wang et al. [68] used the Picometrology to measure the refractive index of graphene on thermal oxide on silicon. They found that the refractive index varies from n_g = 2.4+ 1.0i at 532 nm to n_g = 3.0+ 1.4i at 633 nm at room temperature. This dispersion is five times stronger than bulk graphite (2.67+ 1.34i to 2.73+1.42i from 532 nm to 633 nm).

A quick comparison of the optical constants values reported for graphene along with corresponding spectral region and experimental technique is also presented in Table 3.1.

Samples	**Technique**	**Spectral region**	**Optical constants (n+ik)**	**Reference**
1LG/SiO2/Si	Reflection spectroscopy	Visible region	3.0+ i1.15 (@550nm)	Bruna et. al [69]
1LG/SiO2/Si	Spectroscopic ellipsometry	360–800 nm	3.0+ i 1.5 (@ 500nm)	Matkovic *et al*. [75]
1LG/SiO2/Si	Reflection spectroscopy	400- 800 nm	2.0+ i1.1	Ni et al. [70]
1LG/SiO2/Si	Picometrology	532 nm , 633 nm	2.4+ i1.0 (@ 532 nm) 3.0+ i1.4 (@ 633 nm)	X Wang et al. [68]
1LG/SiO2/Si	Density functional theory	Visible region	2.79+ i1.48	M Klintenberg et. al. [76]

Table 3.1: Optical constants data of graphene reported in literature.

Chapter 4. Experimental Setup and Methodology

4.1 Introduction

Samples of (1LG/SiO_2/Si, 3LG/SiO_2/Si, and SiO_2/Si) were provided by Graphenea Inc. Monolayer graphene was grown on a Cu substrate by a chemical vapor deposition process (CVD). Then the monolayer graphene was transferred to SiO_2/Si substrate by wet transfer method. In case of three-layer graphene, transfer process was repeated three times to get the tri-layer graphene over SiO_2/Si substrate. The coverage of graphene on SiO_2/Si substrate is > 95% and grain size up to 20 μm.

The samples were characterized structurally and qualitatively by Atomic force microscopy (AFM), Raman spectroscopy and X-ray photoelectron spectroscopy (XPS). The optical characterizations of samples were performed using a tabletop EUV-VUV reflectometer facility located at CNR Padova and at BEAR beamline available at ELETTRA synchrotron in Trieste.

Experimental data were analyzed in terms of optical performances of the graphene (1L & 3L) and SiO_2 samples in VUV spectral region. Based on the experimental measurements performed, optical parameter (e.g., ellipsometric parameters, optical anisotropy, optical constants, Brewster angle) were deduced.

This chapter covers the description of the experimental setups used and all the experimental activities performed to achieve the research objectives related to optical properties of samples in VUV spectral region. However, a detailed discussion of results, analysis, and findings is discussed in later chapters.

4.2 The EUV-VUV Normal Incidence Reflectometer

The normal incidence reflectometer facility available at IFN Padova provides the opportunity of different measurements such as transmittance and reflectance over a wide spectral range from EUV-VUV spectral region. A schematic diagram of the facility is shown in Figure 4.1 There are four main parts of the facility, i.e., source, monochromator section (grating), focusing section and experimental chamber (sample holder and detector compartment). Deuterium lamp was used as a source in the experiment and connected to the entrance slit of the monochromator section. The

monochromator consists of a 600 groove/mm toroidal Pt-coated grating f/10 with the main radius of 0.5 at a subtended angle of about 25° between the entrance and the exit slits. The height of both slits is 3 mm, and the width is adjustable from zero to 650 µm by a micrometer. The grating is fixed on the rotating platform, which can rotate the grating step by step following a Johnson-Onaka configuration [1] to select the preferred spectral line at the output slit. There is a gate valve which can be used to isolate the monochromatic section from the focusing section. This valve is also used to block the radiation coming to the detector while measuring dark (background) signal. In the focusing section, a toroidal mirror working at a 45° incidence angle reflects the monochromatic radiation to the sample placed in the experimental chamber together with the detector. The sample holder is attached to the motor to change the incidence angle on the sample. The detector is also placed on the additional rotating mechanism in the experimental chamber to perform reflectance measurements in θ-2θ configuration.

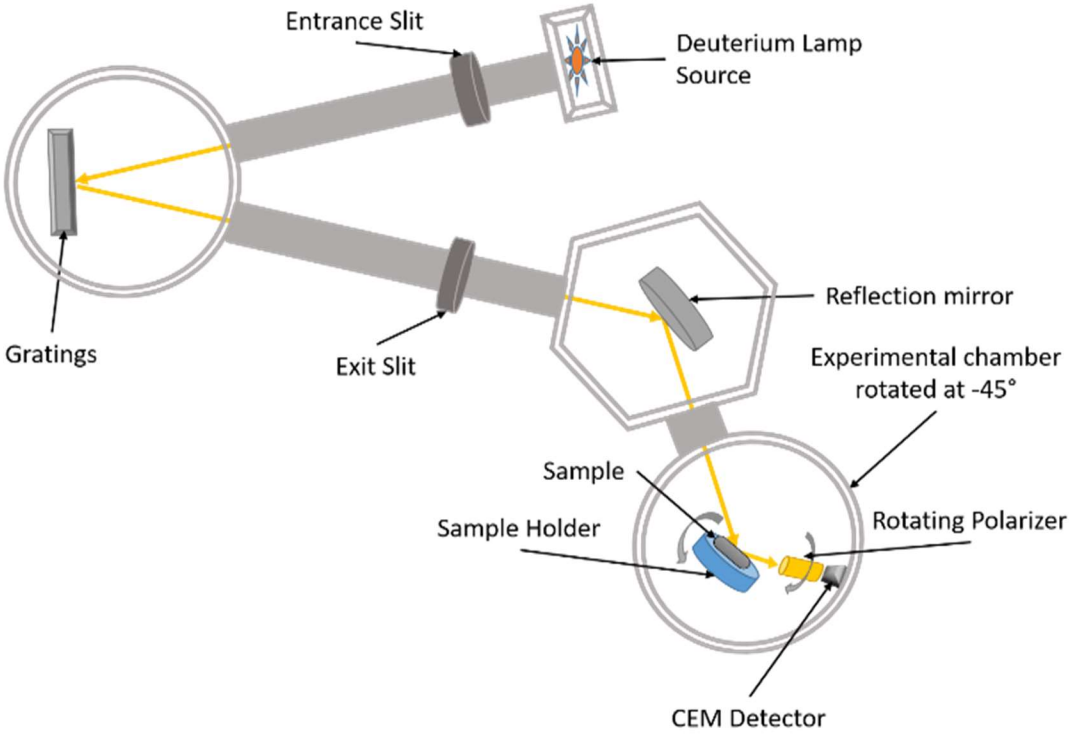

Figure 4.1: Schematic view of the EUV-VUV reflectometer available at CNR-IFN Padova.

There are two primary pumps (scroll pumps) and two secondary pumps (turbomolecular pumps) attached to the facility to achieve the chamber base pressure of ~10^{-7} mbar to avoid the absorption of radiation by air. The output radiation which reaches the sample is partially linearly polarized

because of the geometrical arrangement of a diffraction grating and toroidal mirror. The detector used in the setup is the channel electron multiplier (CEM KBL10/90) manufactured by Sjuts Optotechnik [78].

The degree of linear polarization of the incident light beam at 121.6 nm spectral line has already been measured using the four gold reflections based linear polarizer [36]. By using the mentioned polarizer as an analyzer, this facility can be converted into the EUV-VUV ellipsometer, and polarimetric measurements can be performed for spectral range 90-160 nm. Figure 4.2 shows the real view of the EUV-VUV reflectometer facility. A brief overview of the source of radiation, CEM detector used, and the linear polarizer is mentioned in the subsequent section.

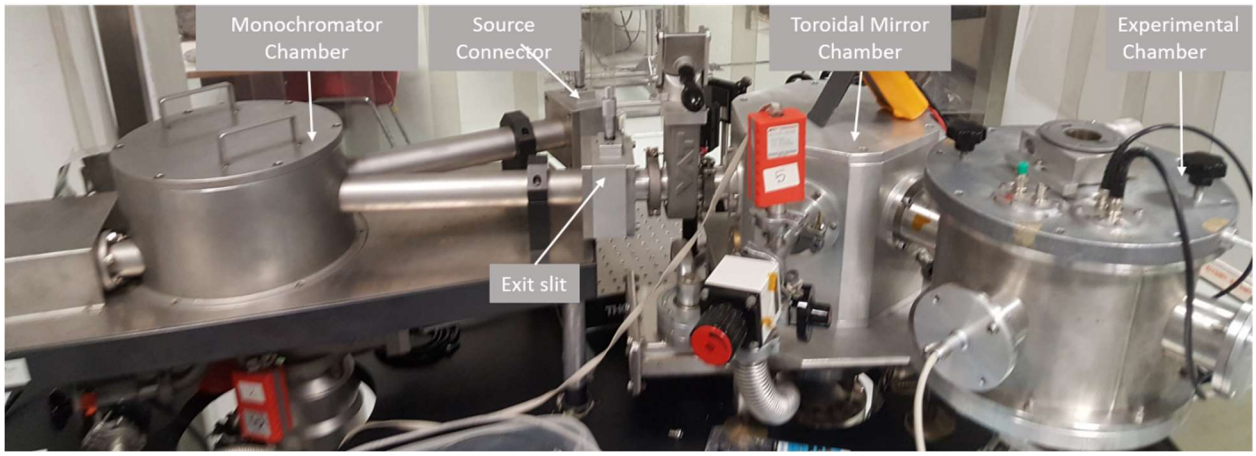

Figure 4.2: Real view of the EUV-VUV reflectometer facility available at CNR- IFN Padova

4.2.1 Deuterium Lamp

There are different light sources available at Luxor IFN Padova, covering EUV-VUV spectral region. For shorter wavelength EUV down to 30 nm, Hollow cathode lamp (HCL) is available as a source. For VUV spectral range the deuterium lamp is available as a source. The radiation source used in the experimental work presented in this thesis was the deuterium lamp.

Deuterium lamp is a continuous source of radiation with deuterium as a working gas. The spectral emission range of the deuterium lamp is 115- 400 nm depending on the transmissive window used. It consists of tungsten filament as the cathode and a thermionic anode in a nickel box with a small aperture for the emission of radiation. Deuterium gas molecules excited to higher energy states through an arc discharge current and de-excitation of the excited atoms of the deuterium gas atoms emits the characteristic radiations. The structure of the deuterium lamp is shown in Figure 4.3. The

lamp comes with different types of transmissive windows such as fused quartz, UV glass, or Magnesium Fluoride depending on the desired applications and working temperature. The spectral distribution of the deuterium lamp with different transmissive windows is shown in Figure 4.4.

In our experiment, the VUV radiation was produced by a deuterium lamp with a Magnesium Fluoride window manufactured by Hamamatsu [79]. The lamp shows two characteristic peaks corresponding to emission lines; 121.6 nm and 160 nm in case of the MgF_2 window. For higher wavelengths (>200 nm), the deuterium lamp comes with silica and glass windows [79]. The deuterium lamp used in the experiment discussed in this thesis came with a housing box which can be connected directly to the facility with vacuum seals to avoid absorption of radiation through the air.

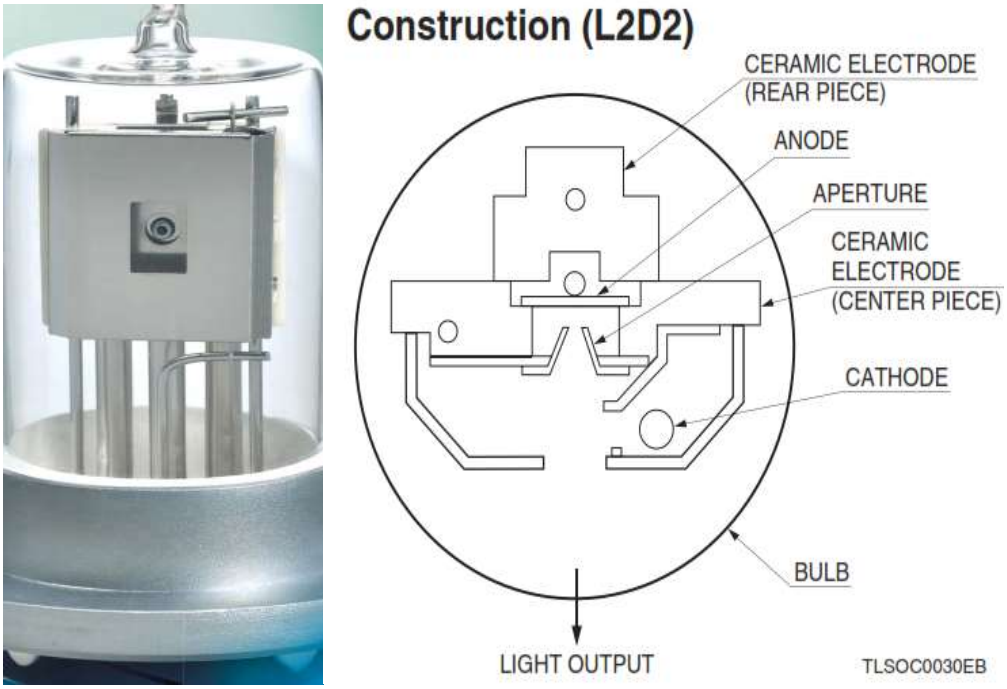

Figure 4.3: Hamamatsu Deuterium lamp [79].

There is a dedicated DC power supply manufactured by Hamamatsu [79] (model C9595). The power supply gives an output voltage between 85 and 90 V with a current intensity of 4 A. The lamp takes around 20 min to stabilize the lamp current and maintain its value.

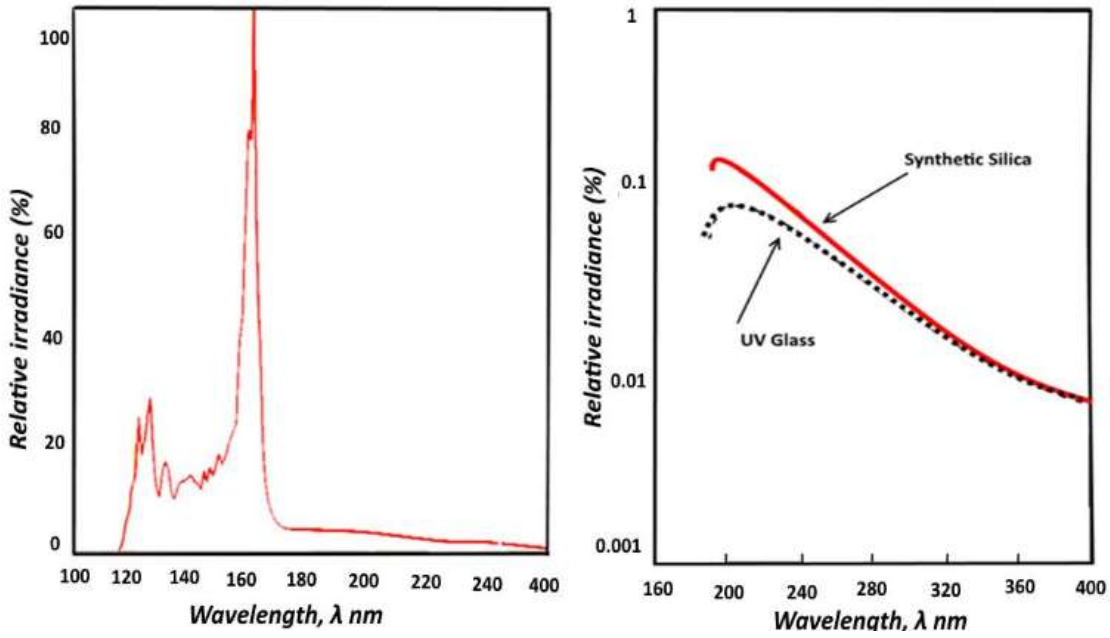

Figure 4.4: Spectral emission spectra of Deuterium lamp (left), spectral emission comparison of different transmissive windows (Synthetic silica, UV glass) (right) [79],

4.2.2 The Channel Electron Multiplier Detector (CEM)

Channel Electron Multipliers (CEMs) are detectors, which are used to detect charged particles, hard and soft X-rays, and ultraviolet radiations. CEM detector has a high surface resistance and acts as a continuous dynode when the potential is applied between the input and output ends. Figure 4.5 shows the CEM detector, its cross-sectional view, and its electrical connection diagram for a negative applied bias. When the primary particle or photon enters into the funnel-shaped aperture and hit the resistive surface, it emits the secondary electron through secondary emission process. Because of the applied bias, the secondary electron accelerated, and when it hits the interior wall, it generates further electrons. Accordingly, a single photon or particle initiate an avalanche process and produce a cloud of electrons. The electron cloud-accelerated towards the anode and output pulses detected easily by using a discriminator, a preamplifier and a counter or as an input current in the analog mode [78].

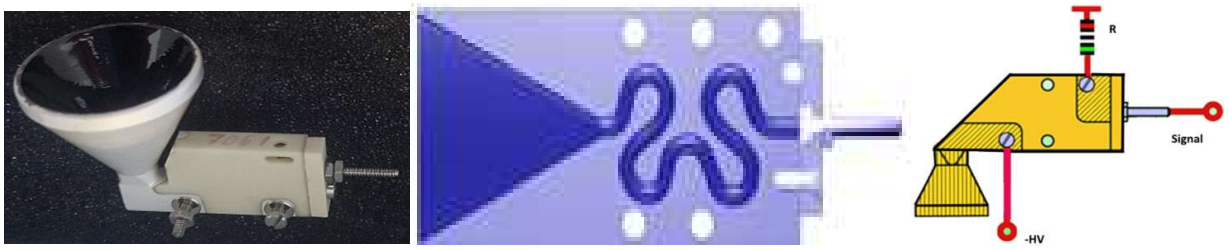

Figure 4.5: Channel electron multiplier (a) real view (b) cross-sectional view (c) he electrical connection diagram of CEM [9].

In our experiments, output signal was measured in terms of the number of counts. The CEM detector used in the experiment was (CEM KBL10/90) manufactured by Sjuts Optotechnik [78]. In order to avoid the short circuit between detector and the wall of experimental chamber, The detector was protected by mounting it inside the Teflon body. During the experiment, the detector was mounted on a movable holder in a θ−2θ configuration to allow angular reflectance measurements.

4.2.3 Four Reflections Linear Polarizer

A four reflections linear polarizer based on four gold-coated mirrors was used to convert the reflectometer into ellipsometer. The gold coating was used because it has good reflectivity for the chosen spectral range. Detailed design of the polarizer is mentioned in [36]. The polarizer designed such as to ensures that the performance of the polarizer is relatively good even over an extended spectral range from 60 to 160 nm. Four gold-coated mirrors were mounted on a specially designed holder to preserve the propagation direction of the incident beam after reflection [36]. A schematic diagram of the polarizer design is shown in Figure 4.6(a)

The polarizer is mounted on a vacuum compatible rotational stage with a minimum angular step size of 0.0025 [80]. Figure 4.6 shows the complete assembly of the polarizer combined with the rotation stage.

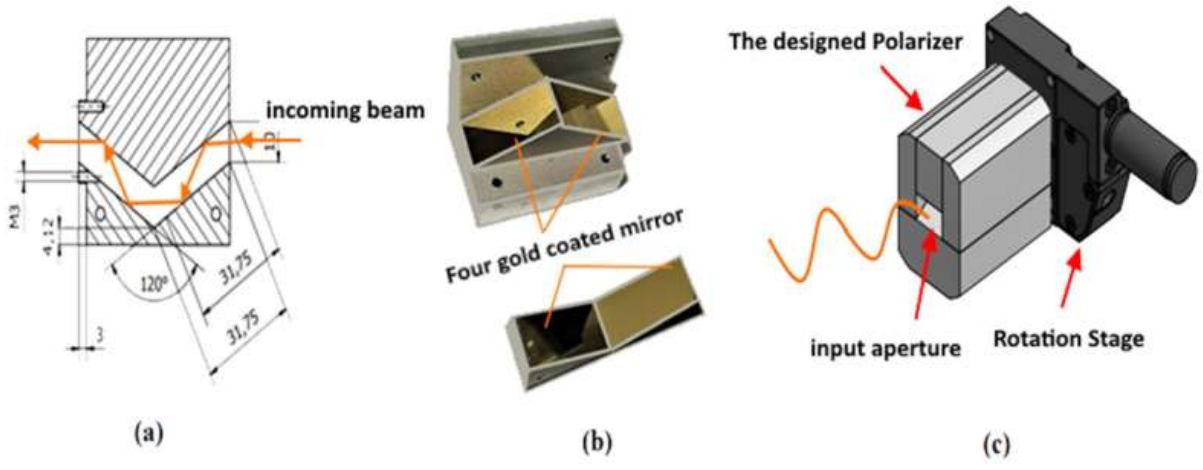

Figure 4.6: (a) Schematic design of polarizer (b) four gold-coated mirrors mounted on the polarizer assembly (c) polarizer along the rotation stage (adopted from[36]).

4.3 The BEAR Beamline

The full characterization of optical tools working in the EUV-VUV spectral ranges requires a suitable radiation source and instrumentation. The BEAR beamline at ELETTRA synchrotron located in Trieste Italy operates in a very wide spectral range from 443 nm wavelength down to soft x-ray at 0.775 nm. The optical layout of the BEAR beamline is shown in Figure 4.7. It consists of a Plane Mirror Plane Grating configuration (PMGM) [81][82]. At the beginning of the beamline, a photon beam position monitor (BPM) is installed which monitors the movement of the beam. A polarization selector device is also installed, in order to select the polarization of light. A Platinum coated mirror is used for collimating the bending magnet light beam on the monochromator. The monochromator has different channels working in parallel mode, i.e., the grazing incidence channel for (40-1600 eV) energy range, and the normal incidence channel for (3-50 eV) energy range. A second paraboloidal mirror P2 collects the monochromatized radiation coming from the monochromator focusing it onto the exit slits. The beam is focused on the sample by an ellipsoidal mirror (REFO). The monitoring of the beam intensity is routinely done by reading the current from the last platinum-coated REFO mirror. Rejection of the higher diffraction orders from the monochromator done by proper choice of the deviation angle and absorption filters (Pyrex, SiO_2, LiF, In, Sn, Al, Si, Ag). The end station is equipped with SXUV-100 photodiodes and Keithley Model 6517A ammeters [83].

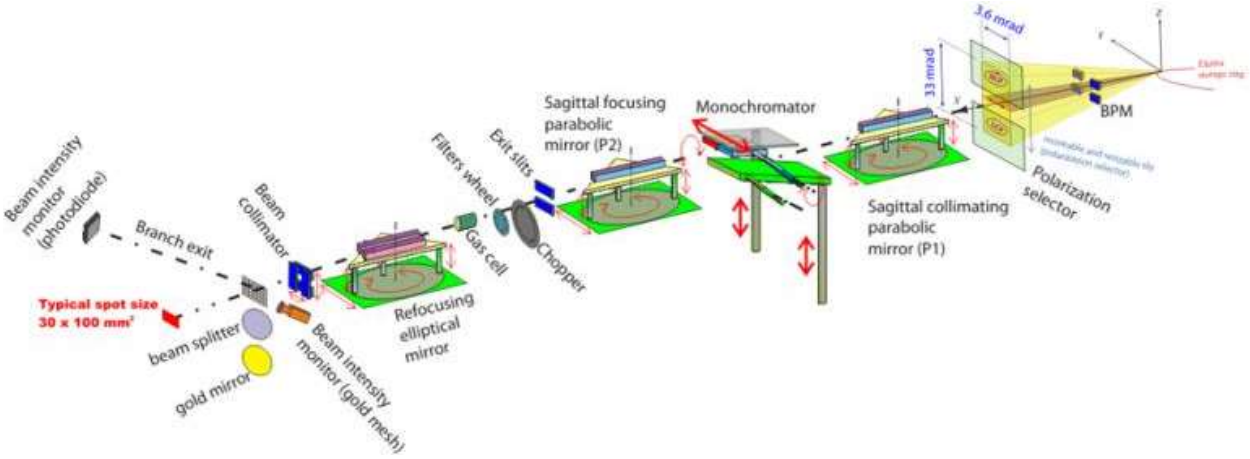

Figure 4.7: The layout of the BEAR beamline [81].

4.4 Atomic-Force Microscopy (AFM)

Atomic-Force Microscopy (AFM) is a technique mainly used to study surface morphology, surface roughness by acquiring the height maps of the area of interest. The working principle of the AFM is the interatomic interaction between the AFM tip and the sample's surface. A laser is focused on the cantilever and reflects any induced change in the frequency and amplitude of the cantilever tip on the detector. Figure 4.8 shows the schematics of the working principle of AFM.

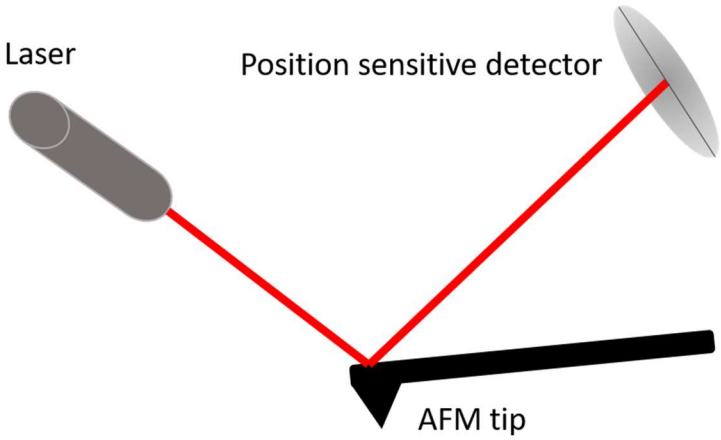

Figure 4.8: Schematic of the AFM measurement procedure.

As can be seen in Figure 4.8, a laser is focused on the back surface of the cantilever and reflected onto a detector (position-sensitive photodiode). By scanning the sample surface, the sharp tip of the cantilever bends as a result of the forces between the tip and the sample surface, which results in the shift of the laser beam on the photodiode and detected. A feedback mechanism maintains a constant force between the sample and tip during the raster scan. The voltage level used to keep constant cantilever tip and sample forces which in turn used to obtain the 3-dimensional image. The typical force-distance curve of AFM is shown in Figure 4.9.

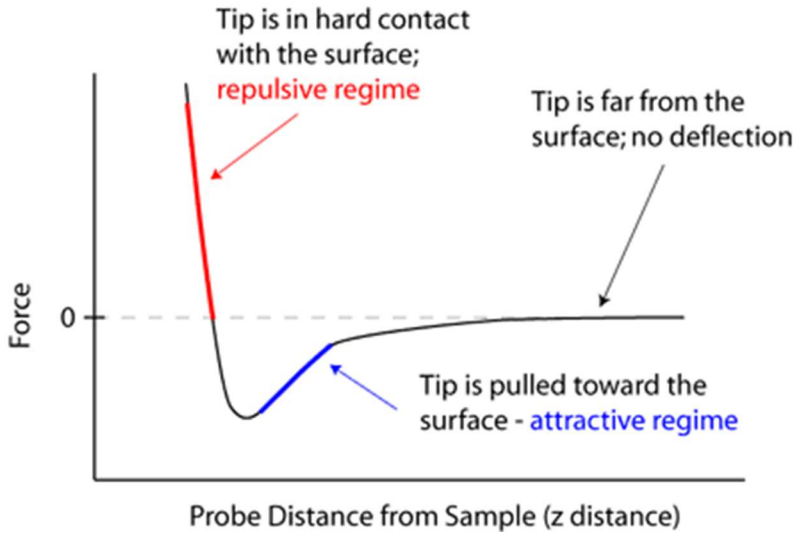

Figure 4.9: Force distance curve for Atomic Force Microscope [84].

Modes of AFM

There are three common modes of AFM operation, i.e., contact mode, non-contact mode, and tapping mode.

In contact mode the cantilever tip is in close contact with the samples and the force on the tip is in repulsive mode. This mode is used for high-resolution imaging because of the higher repulsive force regime. The drawback in this mode is the higher probability of sample damage as well as the tip of the cantilever. In non-contact mode, the cantilever tip floats 50- 140 A° above the surface of the sample. In this mode the force between the tip and the sample is attractive, which is weaker than in the repulsive regime. In tapping mode operation, the cantilever oscillates with its resonant frequency and taps the sample for very brief periods of time. In this mode the force between the cantilever and the sample is in the repulsive regime. In this mode also the high-resolution images obtained with less probability of damage of sample and tip.

The AFM setup used for the surface morphology analysis of the samples was a Park System 70 XE-series atomic force microscope (AFM) available at CNR- Institute for Photonics and Nanotechnologies (CNR-IFN) Padova, Italy. The measurements were performed in non-contact mode.

4.5 Raman Spectroscopy

Raman spectroscopy is used to detect rotational, vibrational, and other low-frequency modes in a system [85][86]. This technique is generally used to know the structural characteristics of the atoms and molecules. In this technique, the monochromatic light source commonly from the laser is used for inelastic scattering or Raman scattering. It investigates the molecular vibrations [87]. In Raman, a monochromatic light falls on the sample and upon interaction with the sample the light scatters in different directions. Most of the scattered light has the same frequency as of incident radiation and creates Rayleigh scattering. A considerably small fraction of scattered radiation has a frequency different from the frequency of incident radiation and constitutes Raman scattering [88]. This shift of the energy/ frequency detected by the detector and gives information about the vibrational modes in the material under test. The Raman spectra can be recorded over a range of 4000–10 cm^{-1}.

To study the 2D materials, especially graphene, Raman, is a well-known and reliable technique. It is a useful and direct procedure to determine doping, quality, and number of layers of graphene [89]–[92]. Generally, there are three main peaks in the Raman spectra of graphene, including D, G, and 2D bands. Based on these peaks, different characteristics of the graphene layers can be determined, e.g., D band to G band ratios can be used to identify the crystalline quality [93] and can be used for defect density determination in graphene. Raman spectroscopy was used in our experiment to study the quality and number of layers of graphene. Green laser was used in this experiment with excitation wavelength of 532 nm.

4.6 X-Ray Photoelectron Spectroscopy (XPS)

X-ray photoelectron spectroscopy (XPS) is the spectroscopic technique based on the classical photoelectric effect, used for the quantitative analysis of surface compositions. The main components of the XPS system are, a monochromatic X-ray light source (lab-based anode or synchrotron based), an ultrahigh vacuum chamber, and an electron analyzer.

A monochromatic beam of X-ray photons focused on the samples surface, as a result of the absorption of x-ray photons by the electrons in the sample, they are ejected from the sample with a specific kinetic energy. The ejected electrons analyzed by a detector based on their number and energy. Relationship of the energy of incident photon (E_{photon}), binding energy of electron ($E_{B.E}$),

kinetic energy of ejected electron ($E_{K.E}$) and work function (Φ) (the minimum energy required to eject an electron from an atom) is shown below.

$$E_{B.E} = E_{Photon} - (E_{K.E} + \phi)$$

The Φ and E_{photon} are known, and $E_{K.E}$ is measured by the detector. Only binding energy is unknown to be determined [94].

Electrons of different orbitals have different binding energy so on the basis of the XPS spectra composition of the material can be determined. Moreover because of the fact that binding energy not only depends on the orbitals of the electron, it also depends on chemical bonding of the atoms, chemical shift can also be determined by XPS. The peak intensities in the XPS spectra correspond to the percent composition of a material. However, peak positions correspond to the binding energy of the ejected electron, which gives information, from which orbital or shell electron is ejected. [94]

We used the synchrotron light based XPS setup available at BEAR beamline for study the quality of graphene samples and possible defects.

4.7 Experimental Activities

Various experimental activities were carried out during the Ph.D. period in order to achieve the research objective of detailed investigations of the optical properties of selected materials by utilizing different diagnostic setups. The experimental activities are divided into two main categories.

4.7.1 Optical characterization

4.7.2 Structural characterization

4.7.1 Optical Characterizations

Optical properties of the samples were determined by measuring polarization-dependent angular reflectance and angular polarimetric data. Angular reflectance measurements of the samples were performed using laboratory-based and synchrotron-based reflectometer facilities. Polarimetric measurements were performed using laboratory-based EUV-VUV reflectometer modified for polarimetric measurements. In the subsequent section, the experimental procedure and measurements are discussed in detail.

4.7.1.1 Angular Reflectance Measurements Using Tabletop EUV-VUV Reflectometer

Angular reflectance measurements of 1L-G/SiO_2/Si and SiO_2/Si samples were carried out using EUV-VUV reflectometer available at CNR-IFN Padova, detailed description of the table-top reflectometer setup is already discussed in section (4.1). The incident light impinging on the samples is partially linearly polarized with a degree of linear polarization (92%) [36] for hydrogen Lyman alpha (121.6nm). The reflectance measurements were performed in two configurations of the experimental chamber (up and down) by rotating the chamber around the direction of the propagating beam to change the angle between the incidence plane and polarization of radiation. The two configurations of the experimental chamber are shown in Figure 4.10. The resultant measured reflectance data corresponding to the orientation of the experimental chamber (up and down) hereinafter will be denoted by R_{up} and $R_{down,}$ respectively. To find out the reflectance w. r. t. s- and p- polarized light, the average reflectance, and the ratio of amplitude reflection coefficients (ρ) corresponding to measured data, the following mathematical expressions were used.

$$R_S = \frac{R_{up} + R_{down}}{2} + \frac{R_{up} - R_{down}}{2 \times f} \tag{4.1}$$

$$R_P = \frac{R_{up} + R_{down}}{2} - \frac{R_{up} - R_{down}}{2 \times f} \tag{4.2}$$

$$R_{avg} = \frac{R_{up} + R_{down}}{2} \tag{4.3}$$

$$ratio = \rho = \frac{r_p}{r_s} = \sqrt{\frac{R_p}{R_s}} \tag{4.4}$$

Where (f) is the degree of polarization of the incident beam already measured using four reflections based linear polarizer.

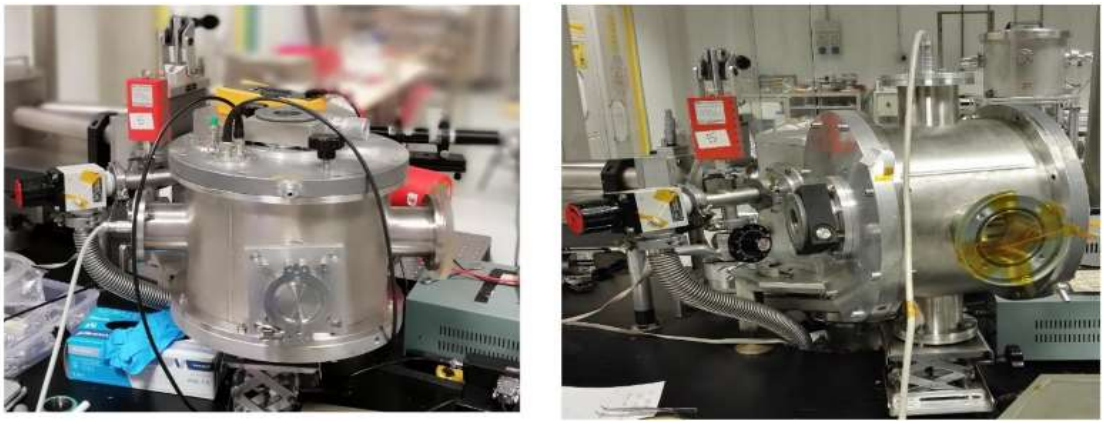

Figure 4.10: Two configurations of the experimental chamber; (left) up configuration (right) down configuration.

Angular reflectance measurements were performed in θ-2θ configuration for angular range 10º-80º. For each incidence angle, 10 data sets of measurement were recorded for statistical analysis (uncertainty and standard deviation) of the measured data. To measure the direct signal, the detector was aligned directly to the incident beam, and the sample was moved away from the beam path, and 10 sets of direct measurements were recorded for statistics. In order to take into account, any background signal, dark (background) signal measurements were performed and subtracted from the reflected and direct signal. The data measured as the number of counts and reflectance for each incidence angle was calculated by the following relation.

$$\text{Reflectance} = \frac{C_R - C_{BG}}{C_D - C_{BG}} \tag{4.5}$$

Where C_R, C_{BG}, C_D are reflected, dark (background) and direct counts. The errors associated with R_s, R_p, R, and ρ *(ratio amplitude reflectance coefficient)* were calculated by applying the propagation of the uncertainty relation by considering the statistical error and intrinsic error in the experimentally measured data R_{up} and R_{down}.

$$\Delta R_s = \frac{\partial}{\partial R_{up}}\left(\frac{R_{up}+R_{down}}{2}+\frac{R_{up}-R_{down}}{2f}\right)\Delta R_{up} + \frac{\partial}{\partial R_{down}}\left(\frac{R_{up}+R_{down}}{2}+\frac{R_{up}-R_{down}}{2f}\right)\Delta R_{down} \tag{4.6}$$

$$\Delta R_p = \frac{\partial}{\partial R_{up}}\left(\frac{R_{up}+R_{down}}{2}-\frac{R_{up}-R_{down}}{2f}\right)\Delta R_{up} + \frac{\partial}{\partial R_{down}}\left(\frac{R_{up}+R_{down}}{2}-\frac{R_{up}-R_{down}}{2f}\right)\Delta R_{down} \tag{4.7}$$

$$\Delta Ratio = \Delta \frac{r_p}{r_s} = \left| \frac{\partial}{\partial R_p} \sqrt{\frac{R_p}{R_s}} \right| \Delta R_p + \left| \frac{\partial}{\partial R_s} \sqrt{\frac{R_p}{R_s}} \right| \Delta R_s \tag{4.8}$$

4.7.1.2 Polarimetric Measurements Using Tabletop EUV-VUV Ellipsometer

Polarimetric measurements were performed by using the tabletop EUV-VUV reflectometer coupled with gold-coated four reflections based linear polarizer (used as an analyzer). The experimental chamber was rotated such as to make nearly linearly polarized radiation at -45° w.r.t. incidence plane (see Figure 4.11). The sample was placed at the desired incidence angle between 50° to 80°. At each incidence angle on the ample, the analyzer was rotated from 0° to 180° with the step of 10°; because of the symmetry, it was not necessary to perform measurements from 180° to 360°. For each step of the rotation angle, five measurements were recorded, then the average and standard deviation were calculated for each dataset.

The data were further analyzed with the help of Stoke's vector and Muller matrix formalism (see section 5.2). The polarimetric data allow estimating the ellipsometric parameters, amplitude ratio (ρ), and phase shift (φ), which were further utilized to extract optical constants by choosing an appropriate optical model.

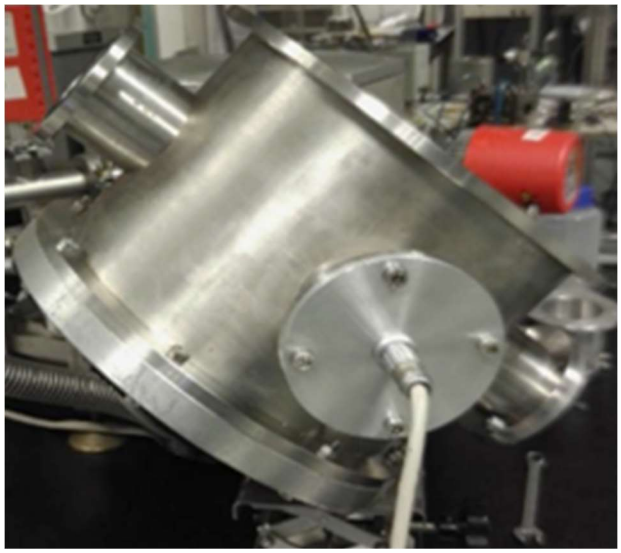

Figure 4.11: The rotated position of the experimental chamber 45-degree clockwise w.r.t. to the propagation direction of the incoming beam.

4.7.1.3 Angular Reflectance Measurements Reflectometer at BEAR Beamline

BEAR beamline at Elettra synchrotron being, highly accurate, complete, reliable, higher spectral and angular resolution is the highly suitable option to carry out the optical studies of materials like graphene which never been studied before in the EUV- VUV spectral region. Therefore, several experimental proposals were submitted for beam time at Elettra synchrotron facility to carry out the experimental activities. After successful proposal evaluations, beam time was assigned to carry out experimental activities at BEAR beamline, and VUV optical characterizations of the samples were performed. The detailed measurement procedure is discussed below.

Angular reflectance measurements of 1LG/SiO_2/Si, 3LG/SiO_2/Si, and SiO_2/Si samples were performed at the VUV spectral region. The measurements were carried out in θ-2θ configuration covering the incidence angle ranging from 3º - 85º with the angular resolution of 0.5º (3LG and SiO_2) and 1.0º (1LG). Reflectance measurements of SiO_2/ Si sample were carried out in order to compare the optical performances of the graphene (1LG and 3LG) samples with their bare substrate. The detail of the samples, along with measurement parameters, are shown in Table 4.1. Measurements were performed for the normal incidence channel by using plane grating GNIM with 1200 l/mm (for spectral range < 40eV). Different filters are available depending on the photon energy for higher-order rejections. For the reflectance measurements discussed in this thesis, Lithium Fluoride (LiF) window was used for higher-order rejections.

Samples were placed on the sample holder designed for BEAR beamline shown in Figure 4.12 and alignment of the samples w.r.t. incident beam and detector were performed by following the alignment procedure.

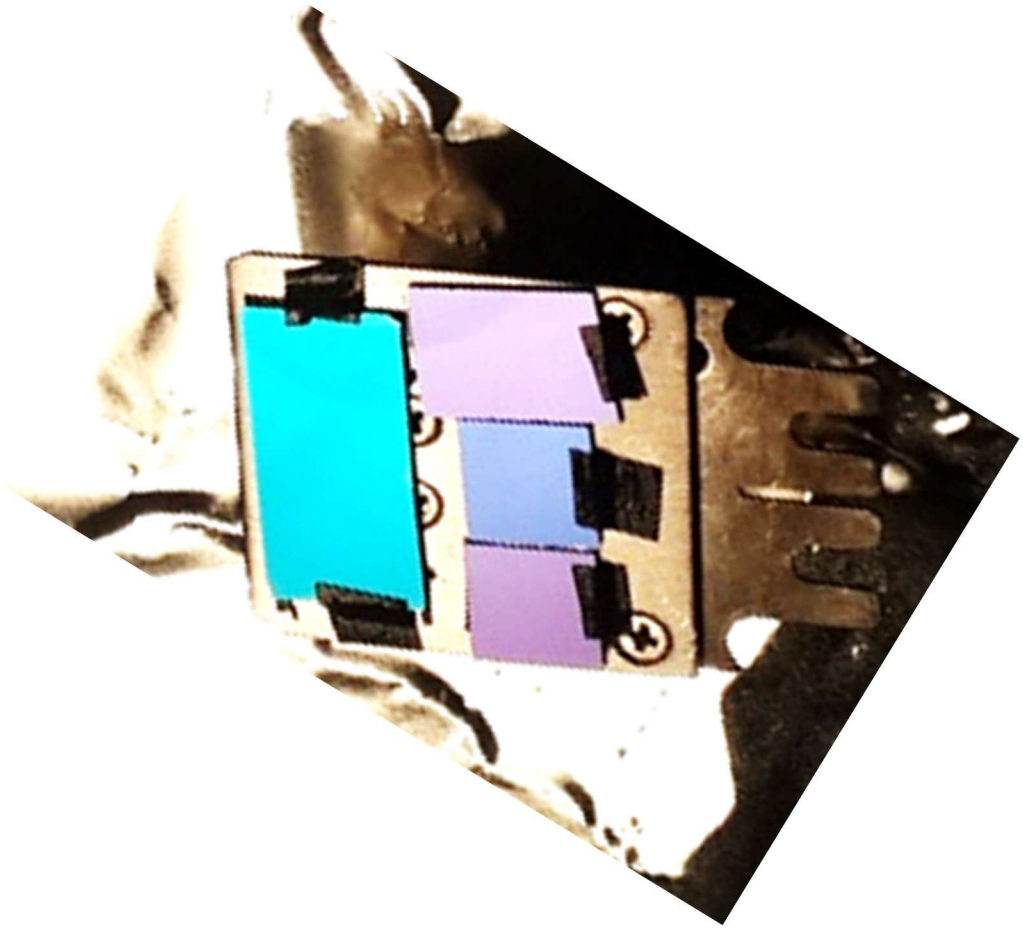

Figure 4.12: Samples mounted on the specialized sample holder at BEAR beamline

In order to calculate the reflectance of the sample for each incidence angle (θ) and photon energy at BEAR, four values are required to be measured, i.e. reflected intensity (from the sample), direct beam intensity (without the sample in the beam path) and two intensity monitor readings which correct for the instability of the beam with time. In addition, the dark current of the detector is also required to be measured in order to remove background noise from the signal. All the data were measured as per the prescribed procedure in the units of current. Using the measured data. reflectance at each incidence angle is calculated as follows.

$$\text{Reflectance} = \frac{\left(\frac{I_{sample} - I_{dark}}{I_{ref} - I_{ref\ dark}}\right)}{\left(\frac{I_{direct} - I_{dark}}{I_{ref} - I_{ref\ dark}}\right)} \tag{4.9}$$

Where I_{sample}, I_{direct}, I_{dark}, are the reflected signal from sample, direct signal, background signal (dark current) respectively at the detector. Where I_{ref} and $I_{ref\ dark}$ are the reference signal and background signal (dark current) respectively at the reference monitor.

The reflectance measurements (R_{up}, and R_{down}) were performed for two configurations of the experimental chamber (up and down) orthogonal to each other. As described earlier from the measured reflectance data (R_{up} and R_{down}) the reflectance for s- and p- polarized light (R_s and R_p), average reflectance (R_{avg}) and ratio (ρ) of amplitude reflectance coefficients can be calculated using eq. 4.1 to 4.4 respectively by knowing the degree of polarization (f) of incidence beam. The degree of polarization of the beam depends on the optical components of the experimental setup, polarization aperture, and the energy of the incident photon beam. Based on the available information about the degree of polarization of BEAR beamline for different polarization apertures and spectral region [83], the degree of polarization was estimated for selected experimental parameters as can be seen in Figure 4.13.

Sample	Angle range	Wavelengths	Configuration
1L G/SiO_2/Si	5-85° Step: 1.0º	121.6 nm	S- & P-configuration
3L G/SiO_2/Si	3-85° Step: 0.5º	121.6 nm	S- & P-configuration
SiO_2/Si	3-85° Step: 0.5º	121.6 nm	S- & P-configuration

Table 4.1: Samples details along with measurement parameters.

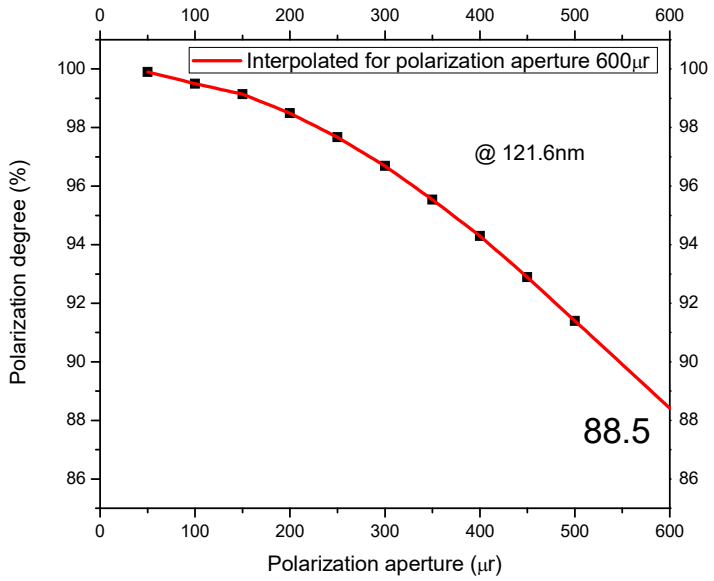

Figure 4.13: Degree of polarization of BEAR beamline estimated for 121.6 nm spectral line and polarization aperture 600 μr.

4.7.1.4 Uncertainty Calculations of BEAR Data

In order to be more precise in reporting the experimental findings, it is important to consider the experimental uncertainty associated with the experimental results. The uncertainty in the experimental data is the accumulative effect of a number of uncertainties, e.g., instrumental uncertainty (cumulative effect of the uncertainty associated to the different components of measurement setup), uncertainty associated to the alignment mechanism, detector noise (photon shot noise).

In the case of BEAR measurement at each instance, four photocurrent measurements were recorded, in order to consider the photon shot noise, responsivity data of each detector must be taken into account. Accuracy of the ammeter readings depends on the tool specifications of the ammeters, associated with this is called instrumental uncertainty. Another source of uncertainty related to the alignment procedure of the sample. The effect of this angular uncertainty on the reflectivity depends on the sample. However the angular accuracy of BEAR beamline limited to $\delta\theta \sim 0.1^{o}$.

The total uncertainty of the reflectivity result can be obtained by summing the three uncertainties in quadrature (as independent and uncorrelated uncertainties).

$$\delta R_{total} = \sqrt{(\delta R_{PSN})^2 + (\delta R_I)^2 + (\delta R_\theta)^2} \quad (4.10)$$

As a cumulative effect of these uncertainties, the BEAR data have the uncertainty (within 5%) in the experimentally measured data (R_{up} and R_{down}) [95]. In order to find the uncertainty in the R_s and R_p data, the propagation of uncertainty relation was used.

4.7.2 Structural Characterizations

The samples have been structurally characterized by Atomic force microscopy (AFM), Raman spectroscopy and XPS. Surface morphology of the samples was studied by using Park System 70 XE-series AFM available at (CNR-IFN) Padova, Italy. Surface morphology scans of different areas were performed for different locations of the samples in non-contact mode. The root-mean-square (RMS) and average surface roughness (Ra) were determined by using XEI data analysis software (Park Systems Corp). Measurements were carried out for graphene samples and also SiO_2 samples in order to compare results. AFM results and analysis are presented in subsequent chapters.

Raman spectroscopic measurements were performed to investigate the quality and number of layers of the graphene samples. Raman spectroscopy is very effective for quality and thickness assessment, especially for 2D materials. Measurements were performed using 532 nm laser from different locations of the samples in order to check the uniformity, especially in 3LG samples. The measured data were compared with the data available with literature in order to assess the quality of graphene films and to determine the number of layers of graphene. Detailed Raman data and analysis is presented in chapter 6.

Furthermore, in order to check the quality of graphene samples and possible contaminations on the surface of graphene samples the XPS measurements were performed at BEAR beamline. For the calibration purpose gold (Au) standard sample was used, and broad scan for the binding energy (B.E) 50-650 eV were carried. High resolution C 1s scan for B.E (275-305 eV) was measured in case of graphene. This scan confirms the presence of sp^2 bonding of carbon atoms which is the characteristic of graphene structure. This is another useful way to check the quality of graphene present on the surface and possible contaminations. The result and analysis of the measurements discussion in chapter 6.

XPS C-1s scan parameters
Photon Energy= 400eV
Initial K.E= 102eV
Final K.E=120eV
ΔE=0.038eV

Table 4.2: XPS scan type and parameters

Chapter 5. VUV Polarimetric Studies of Silicon Dioxide and Graphene

This work is partially based on the following publication which was awarded as **BEST STUDENT PAPER** at SPIE Optics+ Optoelectronics conference.

Nadeem Ahmed, P. Nicolosi, A. E. H. Gaballah, K. Jimenez, and P. Zuppella "EUV reflective ellipsometry in laboratory: determination of the optical constants and phase retarder properties of SiO_2 at hydrogen Lyman–alpha", Proc. SPIE 11032, EUV and X-ray Optics: Synergy between Laboratory and Space VI, 110320V (26 April 2019); https://doi.org/10.1117/12.2520834

5.1 Introduction

As mentioned in chapter 2, the study of the optical constants in EUV- VUV spectral range can be approached in several ways, by optimizing reflectance and transmittance data analysis, e.g., least-square curve fitting of reflectance [96] and using K–K relations [97], double K–K or interactive K–K [98][99]. Unfortunately, materials in the EUV- VUV experience several strong resonances affecting the reliability of the obtained results. The optical constants derived through the least square fitting of reflectance versus incidence angles at selected energies are not always reliable, showing that the reflectance alone is often not enough for a complete optical characterization of the specimen. An ellipsometric study of the sample is required, especially when the optical tools and the physical phenomena under investigation are polarization-dependent.

In this chapter, a novel approach is proposed for the direct characterization of the optical constants and structural properties of materials at a single wavelength. The method doesn't require the use of K–K relations and the optical characterization over an extended spectral range. Based on the combined use of EUV-VUV polarimetry and reflectometry, the technique was successfully applied to the study of SiO_2. The SiO_2 finds considerable applications in optical and electro-optical devices, including the development of photolithography mask for the semiconductor industry [100]. Whatever the application, a full optical characterization is required. Furthermore, the optical properties in the EUV-VUV spectral range are related to the electronic structure and interatomic bonding of the material. Pantelides *et al.* [101] compared optical and theoretical spectra of SiO_2

and concluded that electron-hole interactions produce an exciton at 10.4 eV and also substantially modify the interband continuum. The experiments discussed in this chapter were performed at 10.2 eV photon energy, very close in energy to the excitonic resonance peak in order to prove the robustness of the approach even in a region where the presence of resonances can affect the analysis accuracy.

The optical constants of the SiO_2 were determined by fitting the ellipsometric parameters, ratio (ρ), and phase shift (ϕ). It was also demonstrated that the reliable optical constants of such a material could not be determined only by reflectance fitting analysis. Moreover, the results show that the SiO_2/Si behaves as a phase retarder by introducing a phase difference between the s- and p-polarization components of the incident beam. The phase shift ranges from 18° to 160°, depending on the incidence angle. Effect of graphene as the capping layer on the polarimetric properties and optical throughput of SiO_2 also demonstrated in this chapter by comparing the polarimetric data of SiO_2 and 1LG/SiO_2.

The tabletop VUV ellipsometry arrangement used in this experiment has been already characterized [36]. The results discussed thereafter to confirm that it is sensitive and nondestructive equipment, powerful way to derive optical constants, films thickness, roughness, interfaces and intermixing layers of optical coatings. The system is complementary to the large-scale facilities like synchrotron light sources, where the access requires proposals approval and assigned beam time.

By summarizing, the experimental procedure includes two main–steps:

1. Polarimetric characterization of SiO_2/Si and 1LG/SiO_2/Si sample at different incidence angles and with nearly linearly polarized radiation at -45° w.r.t. incidence plane.
2. Angular reflectance measurements of SiO_2/Si and 1LG/SiO_2/Si samples for the two mutually orthogonal orientations of the plane of incidence hereinafter referred to as *up* and *down.*

The detailed experimental procedure for measuring the reflectometry data and the polarimetric data is described in section 4.7.1.1 and 4.7.1.2, respectively.

The results, the analysis, and the discussion are addressed in the subsequent sections of this chapter.

5.2 Polarimetric Data Analysis

The facility was fully characterized in terms of the Stokes parameters and polarization degree by using the linear polarizer and the detector [36]. These parameters are required for polarimetric data analysis of the samples.

The Muller matrix formalism based on the Stokes vector was used for the polarimetric data analysis. The polarization state of a source can be characterized in terms of the Stokes parameters representing the components of a vector $S = (S_0, S_1, S_2, S_3)$, where S_o is the total irradiance of the light beam, the parameter S_1 describes the amount of horizontal or vertical linear polarization, the parameter S_2 refers to the amount of +45° or −45° linear polarization and S_3 the amount of right or left circular polarization. When the beam goes through an optical element, its polarization can be modified [102]. The effect of optical elements can be described by the Mueller matrix *M(4x4)* associated to the system and applied to the Stokes vector *S* of the incoming beam.

$$S' = M \cdot S \tag{5.1}$$

where *S'* is the Stokes vector of the output beam, *S* represents the Stokes vector of the input light beam, and *M* is the Mueller matrix of the optical element. An instrument often consists of several optical elements, and its Mueller matrix is given by the product of the Mueller matrix of each element [102]. The Mueller matrix of the four reflections based Au polarizer used as analyzer is given by:

$$M_{FRP} = \begin{pmatrix} \frac{|r_s|^8 + |r_p|^8}{2} & \frac{|r_s|^8 - |r_p|^8}{2} & 0 & 0 \\ \frac{|r_s|^8 - |r_p|^8}{2} & \frac{|r_s|^8 + |r_p|^8}{2} & 0 & 0 \\ 0 & 0 & |r_s|^4 \ |r_p|^4 & 0 \\ 0 & 0 & 0 & |r_s|^4 \ |r_p|^4 \end{pmatrix} \tag{5.2}$$

Where r_s^2 and r_p^2 are the electric field amplitude of the reflection of the gold mirror, as the polarizer is consists of four reflection mirrors the terms r_s^8 and r_p^8 corresponds to that. Rotation of the polarizer must be included by multiplying the Mueller matrix with the matrix of a rotator with rotation angle θ.

$$R(-\theta)M_{FRP}R(\theta) \tag{5.3}$$

Where rotation matrix R(θ) is

$$R(\theta)=\begin{bmatrix}1 & 0 & 0 & 0\\ 0 & \cos\theta & \sin 2\theta & 0\\ 0 & -\sin 2\theta & \cos 2\theta & 0\\ 0 & 0 & 0 & 1\end{bmatrix} \tag{5.4}$$

The Muller matrix of the retarder is

$$\mathrm{M_{Retardar}}=\begin{pmatrix}\frac{|r_s|^2+|r_p|^2}{2} & \frac{|r_s|^2-|r_p|^2}{2} & 0 & 0\\ \frac{|r_s|^2-|r_p|^2}{2} & \frac{|r_s|^2+|r_p|^2}{2} & 0 & 0\\ 0 & 0 & |r_s||r_p|\cos\phi & |r_s||r_p|\sin\phi\\ 0 & 0 & -|r_s||r_p|\sin\phi & |r_s||r_p|\cos\phi\end{pmatrix} \tag{5.5}$$

Then the output signal of the beam impinging the sample and passing through the rotating polarizer (analyzer) in terms of Stokes parameters and Muller matrix can be calculated according to the following relationship:

$$\mathrm{S'=R(-\theta)\times M(FRP)\times R(\theta)\times}M_{\mathrm{Re}tarder}\times S \tag{5.6}$$

In our particular case, i.e., the emitted light from the source pass through the reflectometer and fall on the sample and then reflected, the reflected radiation then analyzed by rotating four reflection based linear polarizer. The detected intensity according to Stokes formalism and Mueller calculus in our case is described as following [103]:

$$S'_0 = \frac{1}{4}\begin{Bmatrix} \left(\left(|r_s|^8 + |r_p|^8\right)\left(|r_S^R|^2 + |r_p^R|^2\right) + \left(|r_s|^8 - |r_p|^8\right)\left(|r_S^R|^2 - |r_p^R|^2\right)\cos 2\theta\right) S_0 \\ + \left(\left(|r_S^R|^2 + |r_p^R|^2\right)\left(|r_S^R|^2 - |r_p^R|^2\right) + \left(|r_s|^8 - |r_p|^8\right)\left(|r_S^R|^2 + |r_p^R|^2\right)\cos 2\theta\right) S_1 \\ + 2\left(\left(|r_s|^8 - |r_p|^8\right) r_s^R r_p^R \cos\phi . \sin 2\theta\right) S_2 + 2\left(\left(|r_s|^8 - |r_p|^8\right) r_s^R r_p^R \sin\phi \sin 2\theta\right) S_3 \end{Bmatrix} \quad (5.7)$$

where:

- S_0' is the first term of the Stokes vector of the output light.
- S_0, S_1, S_2, and S_3 are the Stokes parameters describing the incoming light.
- r_s and r_p the reflection coefficients of the gold coating.
- r_s^R and r_p^R the reflection coefficients of the sample under study.
- θ is the rotation angle of the polarizer.
- ϕ is the relative phase of *s*-and *p*-reflected component.

A MATLAB code based on this formula was developed to retrieve the ratio (ρ) and the phase shift (ϕ) introduced by the samples.

5.3 Results and Discussions

The ellipsometric measurements of the SiO_2 were performed at six different incidence angles: 50°, 60°, 65°, 70°, 75°, and 80°. The experimental results (black) are shown in Figure 5.1, together with the fitted curves (red).

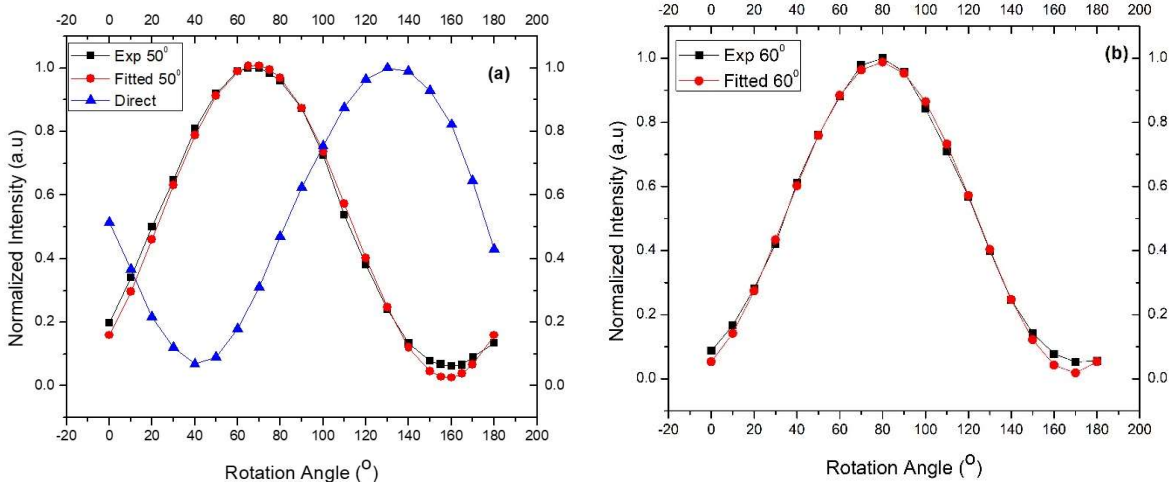

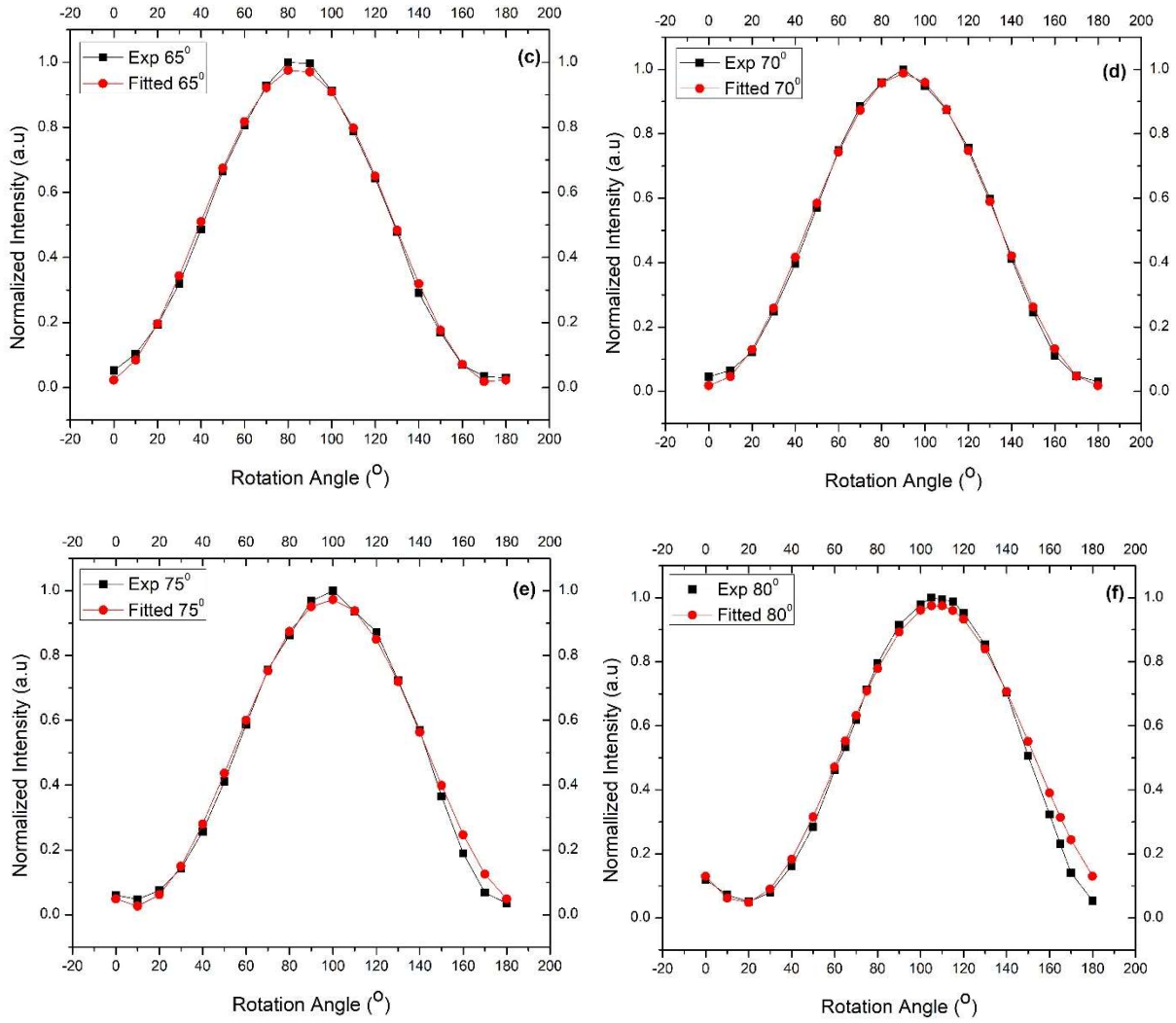

Figure 5.1: Ellipsometric measurements of SiO_2: experimental (black) and fitted (red) data against the incidence angle. Figure 5.1 (a) also shows the direct signal acquired by rotating the polarizer without the sample.

In addition, Figure 5.1 (a) (blue) shows the direct signal acquired by rotating the linear polarizer around the axis.

The insertion of the SiO_2 mirror changes the polarization state of the light delivered by the facility as it can be observed by comparing the direct beam signal with the other curves in Figure 5.1. It is worth noting that the polarization state of the output light and the ellipsometric parameters depend on the incidence angle of the beam impinging on the sample.

Figure 5.2 shows the *s*-and *p*-reflectance versus the incidence angle, error bars based on the propagation error of R_s and R_p by taking into account uncertainty in the experimental

measurements (R_{up} and R_{down}). The reflectance R_p and R_s were retrieved from the measured reflectance data (R_{up} and R_{down}) by using the relationship mentioned in eq. 4.1 and eq. 4.2.

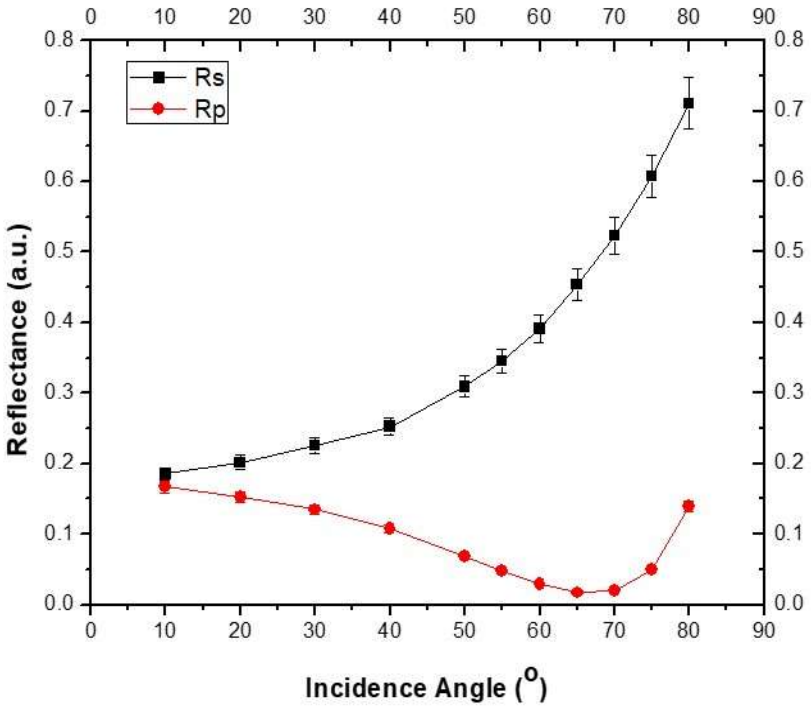

Figure 5.2: Experimental s- and p- reflectance of SiO_2 versus the incidence angle.

The results show a clear difference between the reflectivity in the two polarizations with a non-zero reflection minimum at around ~ 67.5° for the p-component, which is the pseudo-Brewster angle ($p\theta$) of the SiO_2 sample.

5.3.1 Extraction of Optical Constants of SiO_2

To find the optical constants (*n, k*) of SiO_2 at hydrogen Lyman alpha spectral line, we used the ellipsometric parameters, phase (ϕ), and ratio (ρ), retrieved by combining polarimetric and reflectance measurements in order to reduce the uncertainty of the approach. IMD software [104] provides a generic algorithm that was used to fit the experimental data accordingly to the sample's structure shown in Figure 5.3. The roughness was not considered in the model because we verified that it doesn't affect the fit.

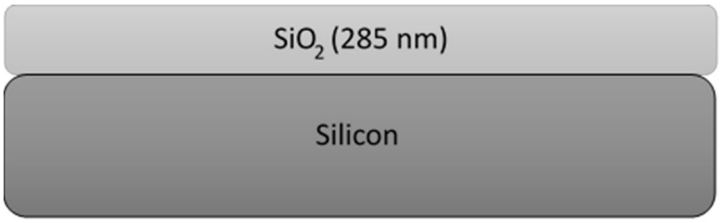

Figure 5.3: Structure of the sample used for simulation

Figure 5.4 shows the phase curve obtained by the ellipsometric analysis (black) and the fit of the data (red) by keeping (*n)* and (*k)* as free parameters. The error bars associated with the phase values are the standard deviation retrieved by polarimetric data analysis. The measurements are intrinsically affected by the uncertainty of the whole experimental arrangement. The source of errors is the uncertainty of the complex alignment of the polarizer and the uncertainty associated with parameter S_3.

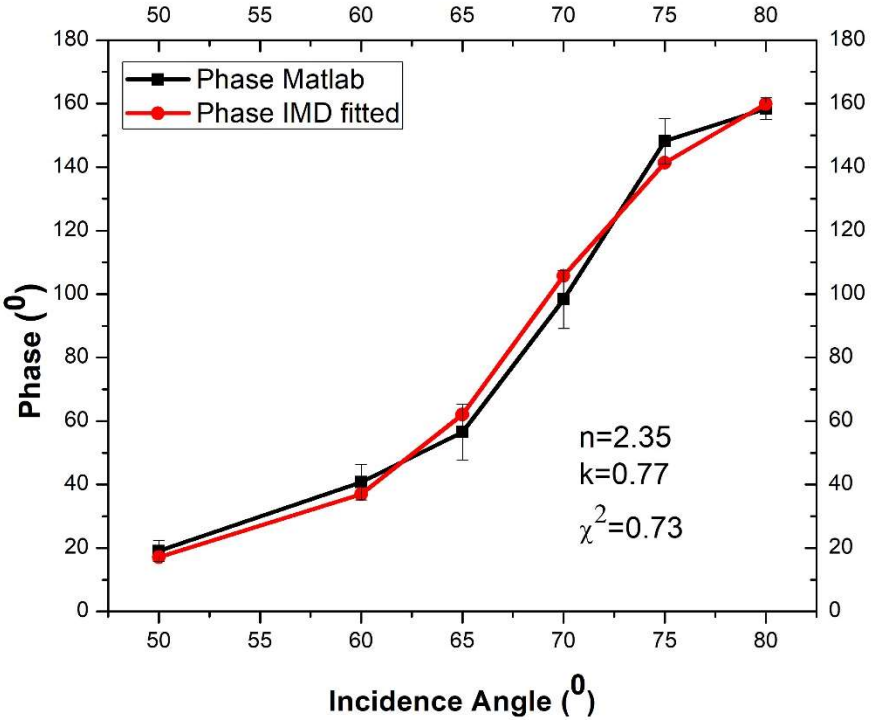

Figure 5.4: Phase difference retrieved by experimental data (black) and IMD fitting of the phase data (red).

Concerning the S_3 term, it cannot be directly measured in the present arrangement since such a measurement requires an additional optical element, for example, a phase retarder, inserted into the optical path. Polarizers and quarter-wave plates working in the EUV-VUV spectral range are not readily available, and their optimization is one of the scientific topics our group is working on.

Nevertheless, considering the experimental arrangement of the normal incidence reflectometer and the almost fully linearly polarized light delivered by the system, we already estimated that S_3 is relatively small [36].

While the phase (ϕ) requires polarimetric measurements to be determined, the ratio (ρ) can also be estimated by reflectance. The two ratio values obtained with the two methods, i.e., polarimetry and reflectance, differ especially at large incidence angles as it can be observed in Figure 5.5 (black for reflectance, blue for polarimetry). Considering the intrinsic uncertainties of both the experimental arrangements and particularly uncertainty associated with S_3 term in case of polarimetric measurement, we are confident that the ratio can be more precisely determined by reflectance in our experimental arrangement. Then, the ratio derived from the experimental reflectance was used for fitting the optical constants by IMD tool (Figure 5.5, red curve).

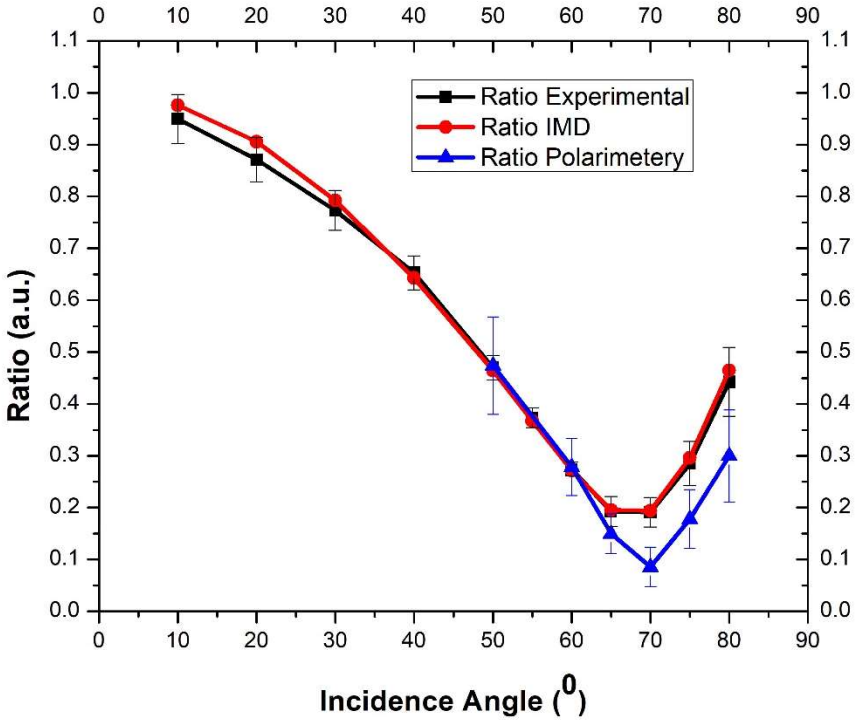

Figure 5.5: Experimental reflectance ratio (black), fitted (red) and experimental ratio by EUV polarimetry (blue) w.r.t. the incidence angle.

Fitted parameters	***n***	***k***	***chi^2***
Ratio	*2.33*	*0.732*	*0.22*

Phase	*2.35*	*0.77*	*0.73*

Table 5.1: Optical constants comparison retrieved by ratio and phase

Table 5.1: resumes the optical constants *(n)* and *(k)* of SiO_2 retrieved by fitting the phase (ϕ) and ratio (ρ), respectively. From *Table 5.1*, it is worth to note that the values of optical constants retrieved by fitting of the ellipsometric parameters measured by two independent measurements are congruent and consistent within 5% uncertainty at maximum. The unique set of optical constants were retrieved with chi^2< 1 shows the quality of fit in both cases. This somehow validates the tabletop VUV polarimetric setup and our approach to find the reliable, unique set of optical constants.

While reflectance data can also be used to derive the optical constants of SiO_2, it results that in this case, several sets of (n) and (k) seem to satisfy the fit (Figure 5.6, right). This is true in the case of R_s, R_p and R. Figure 5.6 (left) shows the R_s reflectance curves corresponding to 2 pairs of (n) and *(k)*. Figure 5.6 (right) shows several pairs qualitatively satisfying the fit and the corresponding chi^2. The problem of convergence shows that, in this case, the fitting procedure based only on reflectance values at various incidence angles is not enough to fully derive the reliable (n) and *(k)*. On the contrary, in the case of ratio and phase, the best fit gives a unique pair of (n) and *(k)*.

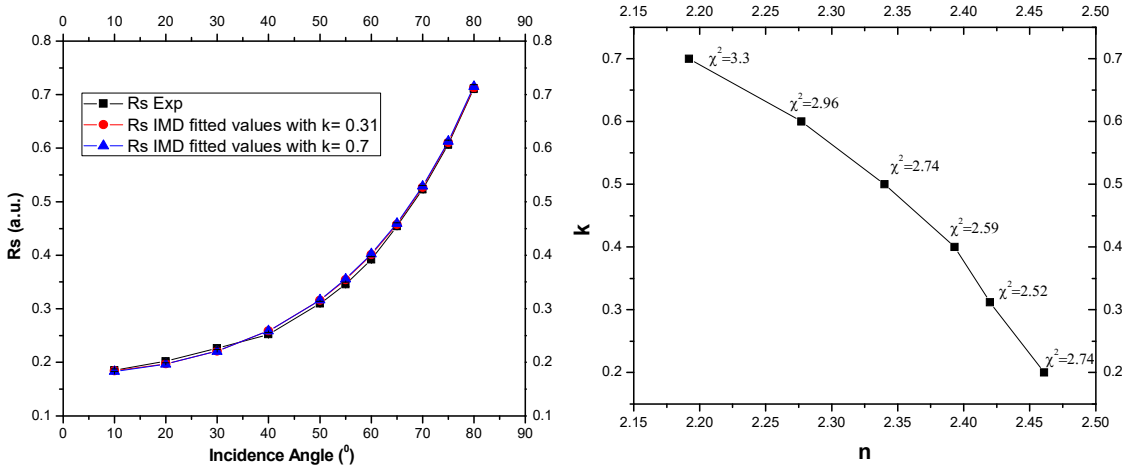

Figure 5.6: IMD fitting of SiO_2 Rs experimental data; (left) for 2 pairs of (n)and (k), (right) pairs of (n) and (k) qualitatively satisfying the fit and corresponding chi^2 values.

The method proposed in this chapter is a promising alternative, allowing to determine both (n) and *(k)*. Self-consistent optical constants of SiO_2 films have been obtained for their relevance from the

near-ultraviolet to the near-infrared spectral ranges [105]. Phillipp *et al*. [106], Tarrio and Schnatterly *et al.* [107], and Filtatova *et al.* [108] provided self-consistent data on the whole spectrum. The values reported by Palik for the silicon dioxide are n=2.24 and k=0.715, respectively [109].

5.3.2 Phase Retarder Properties of SiO_2

A further analysis concerns the properties of silicon dioxide as a phase retarder. The phase shift retrieved from the polarimetric data indicates that SiO_2 behaves as phase retarder by introducing a phase shift between the *s*-and *p*- polarization components of the incoming light. As can be seen from Figure 5.4, the phase difference ranges from 18° to 160° by varying the incidence angle on the sample between 50°- 80°. Angle-dependent phase retarder properties of the SiO_2 indicate its possible potential for utilization as a tunable VUV phase retarder w.r.t incidence angle at the cost of reflection efficiency. Being cheap, readily available, and resistant to a harsh environment, SiO_2 can be an excellent optical material to be considered for vacuum ultraviolet polarimetry.

5.3.3 Polarimetric Properties of 1LG/SiO_2/Si

The ellipsometric measurements of the 1LG/SiO_2/Si were also performed at six different incidence angles: 50°, 60°, 65°, 70°, 75°, and 80°. Figure 5.7 shows the polarimetric measured data for 0-180°rotation of linear polarizer at fixed incidence angles. It can be observed from Figure 5.7 the reflectivity increases when incidence angle approaches to grazing incidence. The polarimetric data were analyzed in a similar manner discussed for SiO_2 using Stokes vector and Muller matrix. The ellipsometric parameter, i.e., the phase difference (ϕ) between s- and p- components retrieved by polarimetric data and ratio (ρ) retrieved by reflectometry data were compared with that of the bare substrate (SiO_2) as can be seen in Figure 5.9 and

Figure *5.10* respectively.

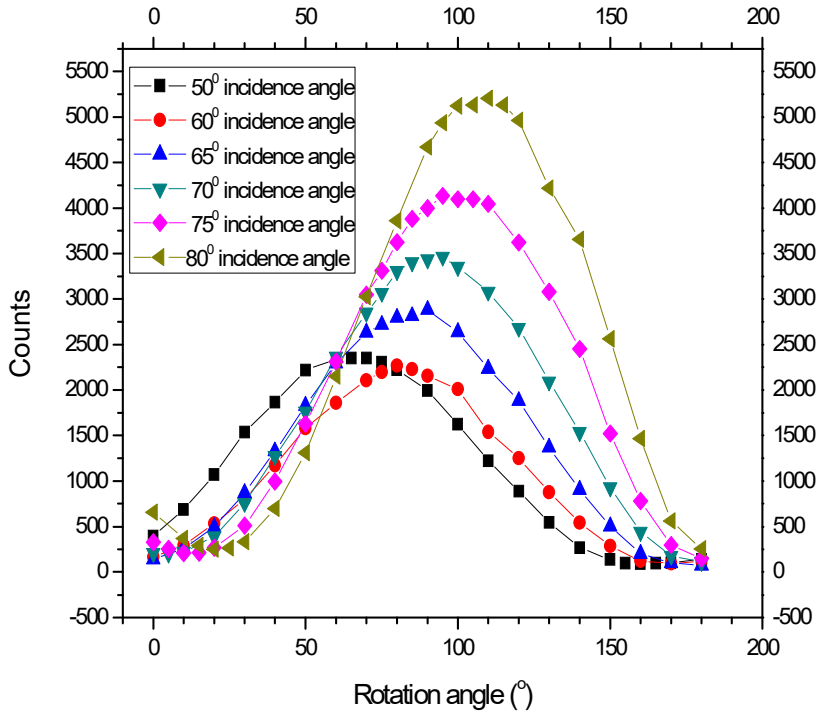

Figure 5.7: Polarimetric data of 1LG/SiO_2/Si at fixed incidence angles for rotating the linear polarizer from 0-180°.

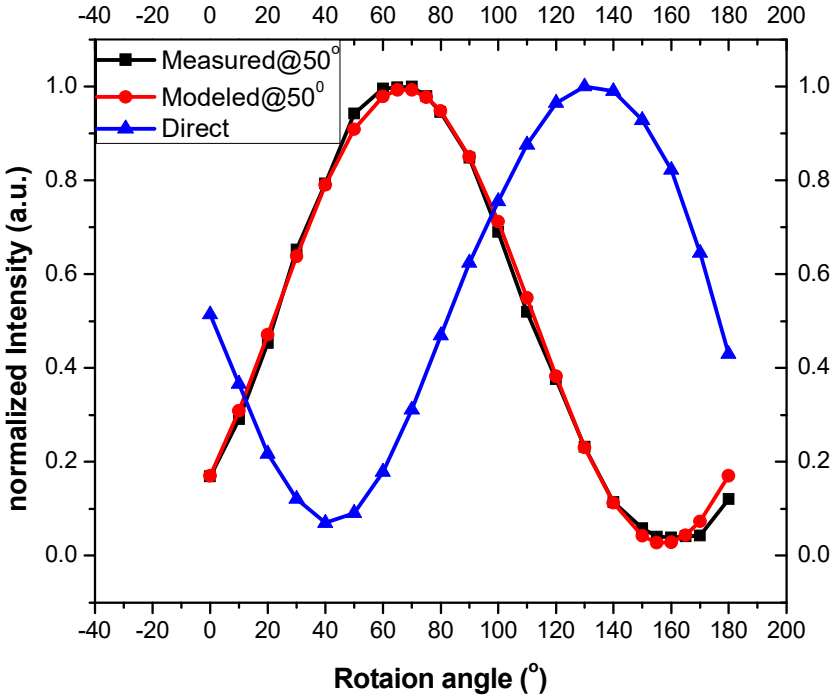

Figure 5.8: Ellipsometric measurements: experimental (black) and fitted (red) data at 50° incidence angle, (blue) shows the direct signal acquired by rotating the polarizer without sample.

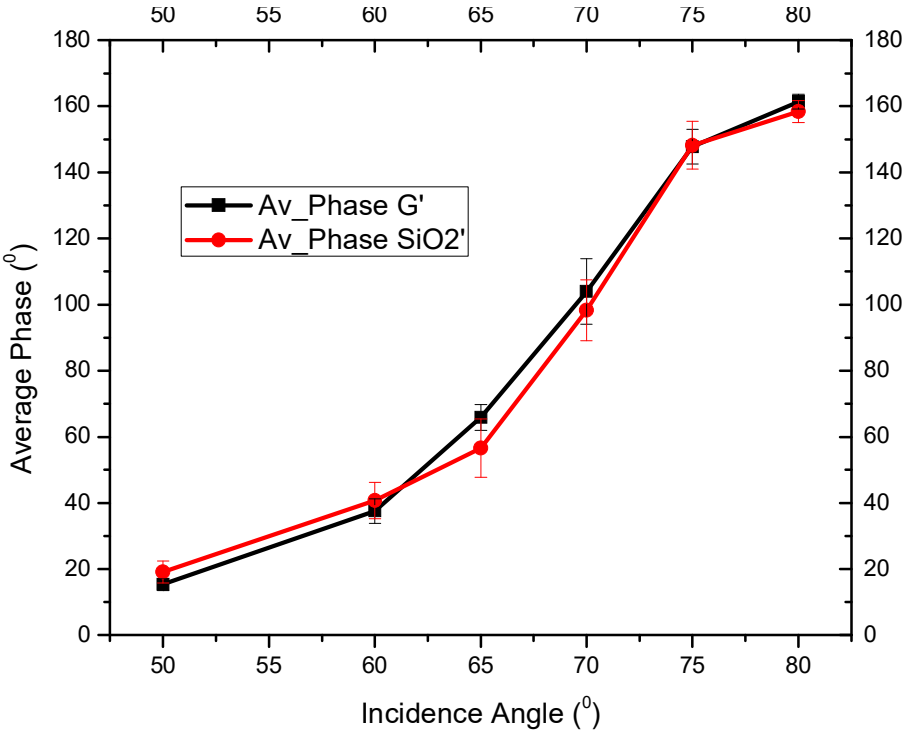

Figure 5.9: Comparison of phase difference retrieved by experimental data; 1LG/SiO_2/Si (black) and SiO_2/Si (red).

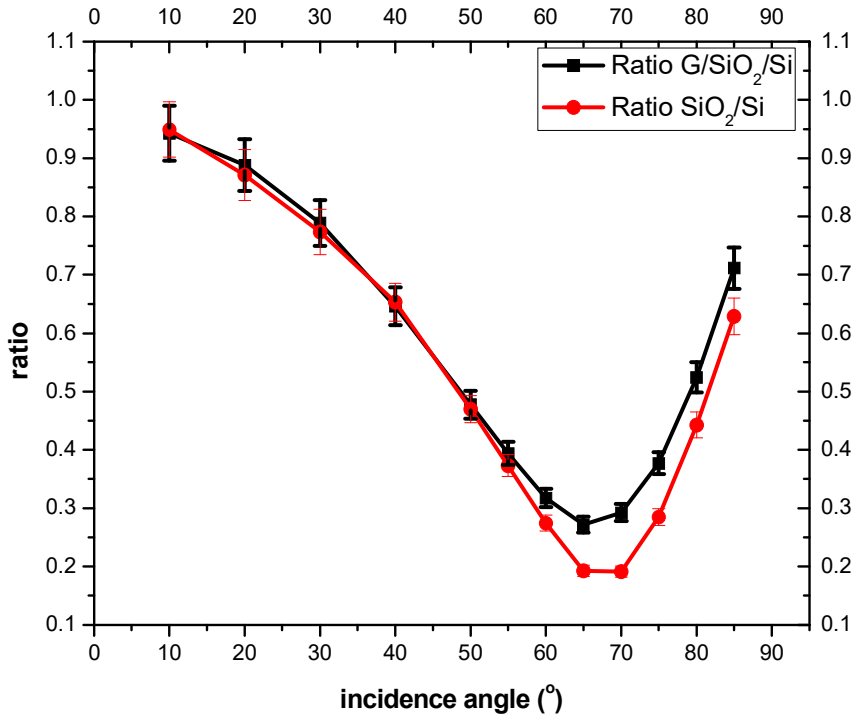

Figure 5.10: Comparison of the reflectance ratio of 1LG/SiO_2/Si (black) and SiO_2/Si (red).

Comparison of the data suggests that 1LG/SiO_2/Si behaves as a phase retarder nearly the similar manner as SiO_2/ Si does, without significantly affecting the phase retarder properties of SiO_2. Although from Figure 5.9, the slight deviation of the 1LG curve from SiO_2 curve near the pseudo-Brewster angle can be observed, it is within the experimental uncertainty. However, a clear difference of the ratio can be observed in

Figure *5.10* in case of bare SiO_2 and SiO_2 coated with monolayer graphene around the Brewster angle and higher incidence angles. It was not possible to calculate the reliable optical constants of graphene in a similar fashion as we did for SiO_2 because of the optical anisotropy of the graphene and atomic thickness. The detailed study about the influence of graphene on the optical properties of SiO_2 and retrieval of optical constants of graphene using angle-resolved reflectometry measurements is discussed in chapter 6.

5.4 Conclusions

The ellipsometric parameters (ρ) and (ϕ) were retrieved by EUV-VUV reflectometry and ellipsometry; then, the parameters were used to determine the optical properties of SiO_2 as a test case. A genetic algorithm of IMD software based on Fresnel equations was applied to fit the ellipsometric parameters by least-squares curve fitting method. It was found that in this case, reliable values of optical constants can be retrieved only by using ellipsometric parameters. It was observed that optical constants derived only by reflectance data fitting are affected by large uncertainty and consequently it was proved in this chapter that by using a tabletop system that combines VUV reflectometry and ellipsometry it is possible to find the reliable values of optical constants and the phase retardation properties of the isotropic material. Angle-dependent phase retarder properties of SiO_2 indicates its potential to be used for VUV polarimetry in technological domains.

The effect of the graphene as a capping layer on the polarimetric properties of SiO_2 substrate is also studied the first time as per our knowledge. It was observed that the presence of 1LG does not affect the phase retarder properties significantly, however, the value of ratio increases around Brewster angle in case of 1LG/SiO_2/Si which indicates the influence of 1LG on the polarimetric properties of SiO_2 at hydrogen Lyman alpha despite having atomic thickness. So the presence of graphene on top of SiO_2 improves the optical throughput of bare SiO_2. This is a significant

consequence and finding, which can prove to be beneficial for hydrogen Lyman alpha optics advancement.

Chapter 6. Optical Investigations of Graphene in the VUV Spectral Region Using Reflectometry

6.1 Introduction

To our knowledge, the optical properties of graphene have been already studied in the infrared (IR), visible (VIS) and ultraviolet (UV) spectral region [110][10][111]. For example, Gray et al. [110] reported the optical constants of graphene on top of SiO_2 (300 nm) in 190-1000 nm spectral range by using optical spectrophotometry and applying the Forouhi Bloomer dispersion relations for the extinction coefficient (k). P. Zuppella et al [10] studied the optical performance of graphene/SiO_2/Si at UV spectral lines (254nm, 280nm, 312nm) and Nelson et al. [111] studied the optical properties and calculated the optical constant of CVD grown and transferred graphene on glass substrate, using the spectroscopic ellipsometry in the IR-UV spectral range. However, no systematic optical analysis has been performed at the extreme ultraviolet (EUV) and vacuum ultraviolet (VUV) spectral bands where mainly the photoreduction induced by the radiation have been investigated [13]. Despite having a thin, nearly atomic thickness, it has been already reported that single-layer graphene absorbs 2.3% visible incoming light [112] and modifies the electrodynamical response of the underlying dielectric substrate SiO_2/Si by altering its Brewster angle in the visible region, [113]. B. Majérus et al. [113] demonstrate theoretically and experimentally that Brewster angle undergoes an upshift if the substrate is covered with a conducting 2D material, upshift of the substrate Brewster angle in case of 1LG, 2LG, and 3LG in the UV-NIR spectral region was demonstrated experimentally. The optical anisotropy of the graphene has been already reported in UV-Visible spectral region by several researchers, Yu-Lun Liu et al. [114] studied it as a quality factor for the rapid characterization of large-area films by developing the variable angle spectroscopic method. M Klintenberg et al. [76] evaluated the anisotropic dielectric constants of single layer Graphene (SLG) and few layers Graphene (FLG) theoretically. However, no experimental study related to optical anisotropic dielectric constants in the VUV has been reported. As the graphene is ultrathin and in order to evaluate the optical performances of the ultrathin films, widely used surface sensitive method is surface differential reflectance (SDR) [115] [116] [117]. However, this method requires carefully prepared samples

and very critical measurements.

In this chapter, the detailed investigations of the optical properties of the commercial monolayer (1L) and tri-layer (3L) graphene onto SiO_2/Si bilayer at 10.2 eV corresponding to the hydrogen Lyman-alpha emission line are discussed. The photons energy choice was dictated by the interest for spectroscopic diagnostics and the related development of suitably performing VUV optical coatings. Laboratory-based EUV-VUV reflectometer and synchrotron-based system (BEAR beamline–ELETTRA synchrotron Trieste) have been used. Angular reflectance measurements of the samples were performed for both polarizations of the incidence beam (s- and p- polarized). Reflectance data show evidence of interaction with atomically thin graphene layers by the change in the reflectance and the modification of the pseudo-Brewster angle of the bare substrate with higher shift for 3LG than for 1LG sample. Distinguishable optical performance was observed for both samples (1LG and 3LG) in spite of the ultra-thin thickness of the films. The detailed optical analysis revealed that graphene over SiO_2 behaves differently for s- and p-polarized light because of different orbital structure projection for different orientation of the graphene surface, this behavior was observed/ evidenced during the retrieval of the "effective" optical constants of graphene using IMD software based on the Fresnel equations for simulation of reflectivity. It is observed that experimental s- reflectance can easily be fitted by one set of optical constants but for p- reflectance the optical constants have angular dependence. Optical anisotropy of graphene and corresponding "effective" optical constants coupled with "effective" thickness was retrieved and studied for both polarizations of incident radiation. In order to qualitatively confirm the reliability of retrieved anisotropic optical constants, SDR data have been derived from reflectance measurements and compared with the theoretical approximation. Raman analysis, coupled with AFM measurements, have been used to confirm the quality of graphene samples and few-layer thickness. XPS data also confirmed the quality of graphene samples.

The results, the analysis, and the discussion are addressed in the subsequent sections of this chapter.

6.2 Results and Discussion

6.2.1 Structural Characterization of Graphene Samples (1LG and 3LG)

The samples have been structurally characterized by atomic force microscopy (AFM), Raman spectroscopy and x-ray photoelectron spectroscopy (XPS), detailed measurement parameters discussed in chapter 4.

In Figure 6.1. the AFM image of the CVD grown 1LG transferred on the SiO_2/Si sample is reported. Relatively uniform morphology of the 1LG sample evidenced in Figure 6.1, although few wrinkles are present but similar as reported in the literature [118]. The wrinkles formation might occur during the cool down process because of having different thermal expansion coefficients of graphene and metal substrate, or during the transfer process because of the surface morphology mismatch between growth substrate Cu and SiO_2/Si final transfer substrate [119][120].

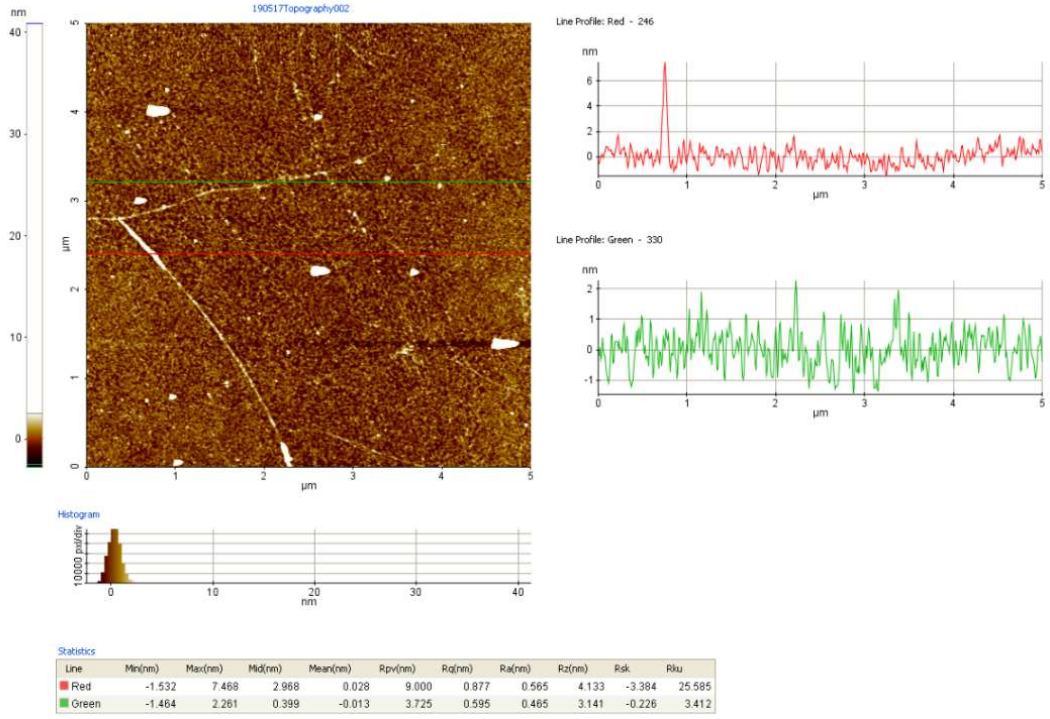

Figure 6.1: AFM image (5x5 µm) of 1LG/SiO_2/Si

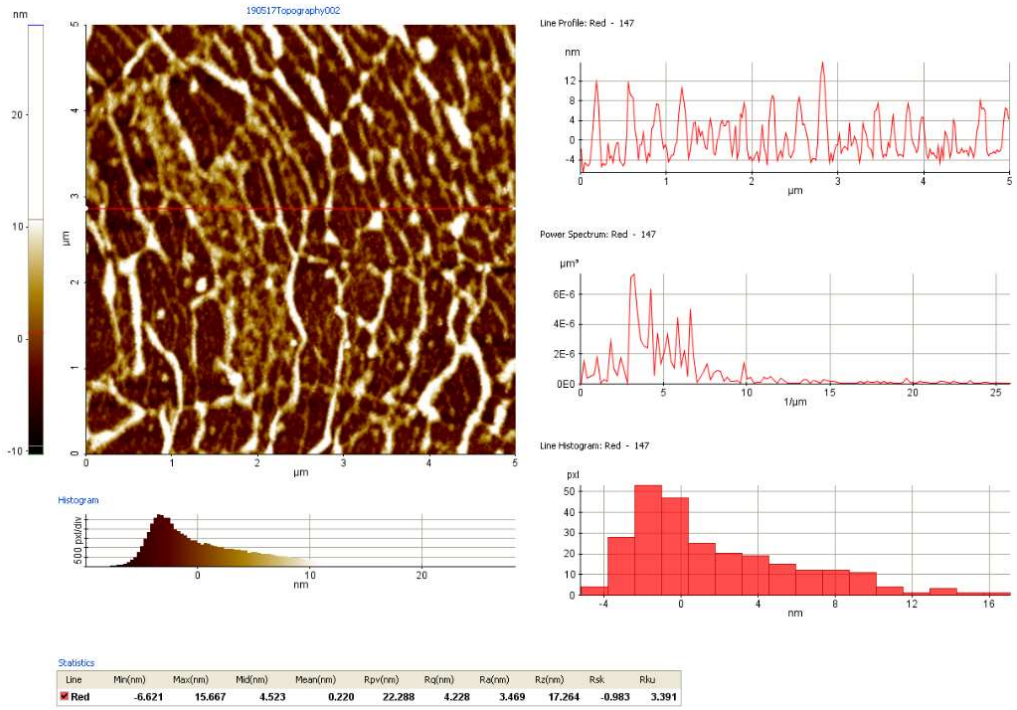

Figure 6.2: AFM image (5x5 µm) of 3LG/SiO_2/Si

Figure 6.2 shows the AFM image of the CVD grown 3LG transferred on the SiO_2/Si substrate. As can be seen from Figure 6.2, the sample has not uniform surface morphology showing a large density of wrinkles. This might be due to the repeated transfer process, followed in order to increase the number of graphene layers.

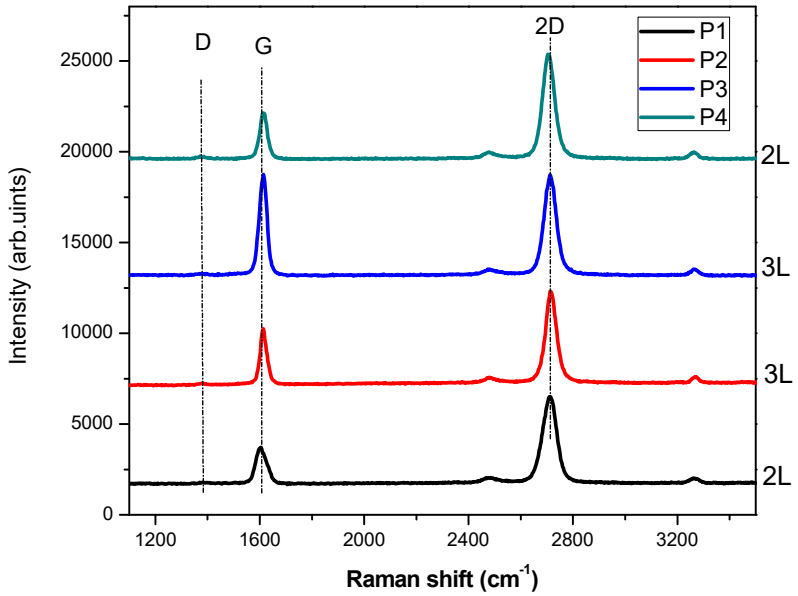

Figure 6.3: Raman spectra of 3LG/SiO_2/Si from four different locations

Raman spectra of the 3LG sample are reported in Figure 6.3 and show the characteristic peaks (D, G, and 2D). Raman spectroscopy was performed on different areas of the samples and it has been found that the sample shows some variations in the intensity of G and 2D peak however the ratio of peaks 2D/G (1.44- 1) confirms that a multilayer graphene film is covering the entire substrate with the thickness values ranging from 2LG to 3LG. The detected small D peak and small ratio of D and G peaks confirms that the sp^3 defects density is negligible. The Raman spectra confirms good quality of graphene coating.

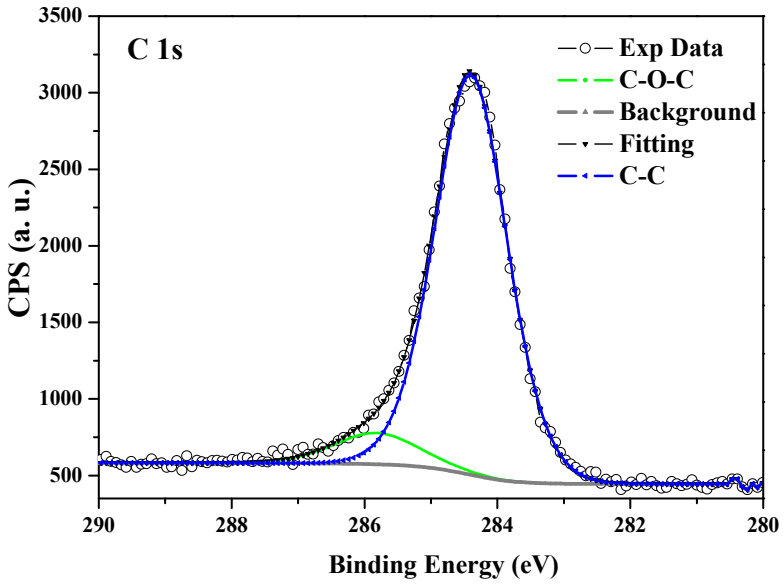

Figure 6.4: XPS (C 1s) spectra of 3LG sample measured at BEAR beamline.

Figure 6.4 shows the C1s spectra of the 3LG sample measured by XPS setup at BEAR beamline, Elettra synchrotron. The detailed measurement parameters are mentioned in Table 4.2. In order to interpret the measured spectra in terms of quality of graphene samples, chemical groups present, a well-known technique of deconvolution of XPS data was used. In order to take into account of the inelastic photoelectron, Shirley background was removed from the spectra. A well-known CasaXPS software [121] was used for analysis of the XPS data. It can be observed from Figure 6.4, C 1s spectrum is dominantly consisting of single peak (C-C) related to characteristic sp^2 structure of graphene, which shows the quality of the graphene films. The convolution and fitting of the data also shows some small contribution of (C-O-C) sp^3 structure peak towards the slightly higher binding energy. These results are consistent with the Raman spectra which also confirms the good quality of graphene with very small D correspond to the negligible sp3 defect density.

6.3 VUV Optical Properties of Graphene (1LG & 3LG)

VUV optical properties of graphene samples have been derived from reflectivity measurements performed for both polarizations of light, i.e., s- and p- polarization. The optical performance of the commercial 1LG and 3LG samples, taking into account the substrate SiO_2/Si has been studied in terms of reflectance, Brewster angle, effective optical constants, optical anisotropy, and surface differential reflectance. Detailed results and analysis are explained in the subsequent sections.

6.3.1 VUV Angular Reflectance Measurements and Analysis

Angular reflectance measurements were performed by using independent EUV- VUV reflectometer facilities, available at CNR-IFN Padova [36][37], and at BEAR beamline-ELETTRA synchrotron in Trieste. Measurements of bare substrate SiO_2/Si supplied together with the graphene samples were also performed for comparison of the optical performance. The brief description of the experimental setups used for the reflectivity measurements of samples is mentioned in chapter (4) under section (4.1) and (4.5) respectively. However, the detailed procedure of the experimental reflectance measurements and parameters is described in section 4.7.1.1 and 4.7.1.3.

The experimental uncertainty of the data is presented as error bars, detailed description of the experimental uncertainty in the data is discussed in the chapter (4) in addition to that there was some discrepancy of R_s and R_p BEAR data at normal incidence because of very low signal to noise ratio (SNR). The calculated amount of this discrepancy near normal incidence is nearly 10% of the experimental data while for the higher angles, the error bars were calculated based on the uncertainty associated with the BEAR data. Propagation of error technique was used to calculate the uncertainty in R_s, R_p, and SDR.

In Figure 6.6, the measurements for 1LG sample performed at BEAR and in the laboratory set-up are compared. The curves are superimposed well within the experimental uncertainty in the whole scanned angular range.

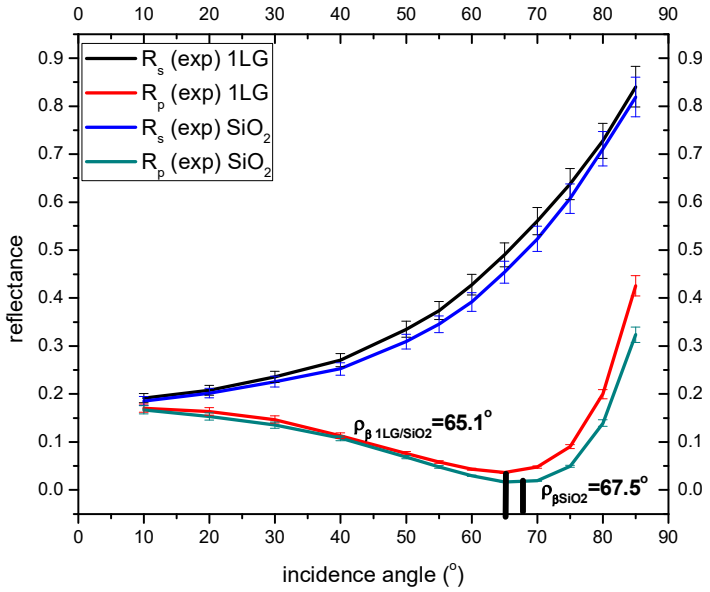

Figure 6.5: Comparison of s- and p- reflectance of 1L G/SiO_2/Si & SiO_2/Si measured at CNR-IFN Padova.

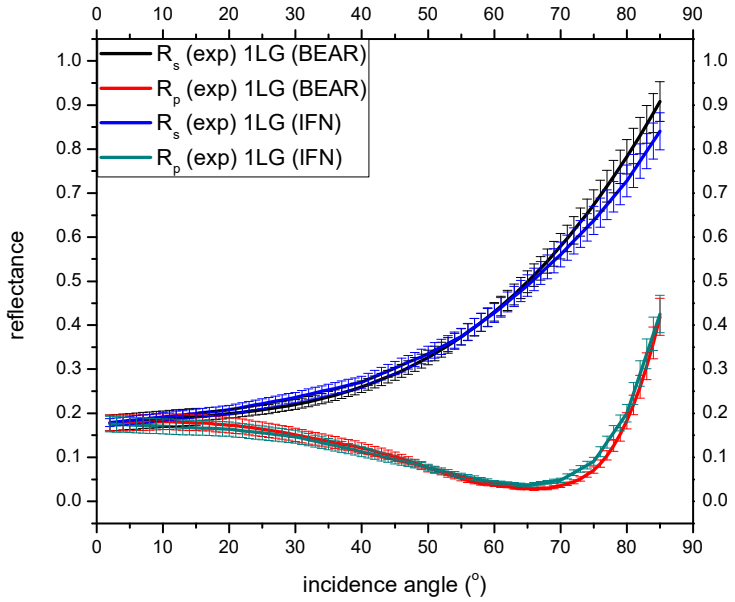

Figure 6.6: Comparison of s- and p- reflectance of 1LG/SiO_2/Si measured at CNR-IFN and BEAR beamline.

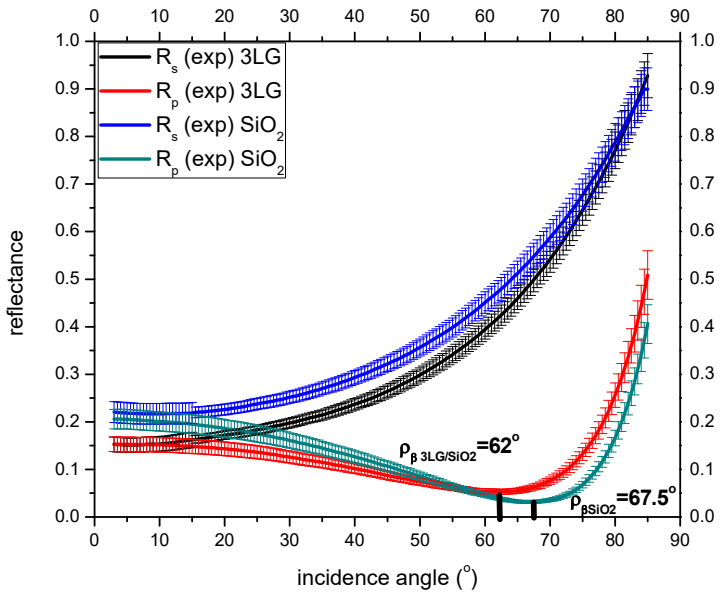

Figure 6.7: Comparison of experimental data; s- and p- reflectance of 3LG/SiO_2/Si and SiO_2/Si measured at BEAR beamline.

The comparison of the measurements of the s- polarized (R_s) and p-polarized (R_p) reflectance for 1LG/SiO_2/Si and 3LG/SiO2/Si with SiO_2/Si substrate are respectively reported in Figure 6.5 and Figure 6.7. The results show a clear improvement of reflectivity in spite of the nearly atomic layer thickness of the graphene films. In addition, the R_p data show a considerable shift of the angle corresponding to the minimum of the curves. The detailed description and analysis of the Brewster angle shift are discussed later in the relevant section. Change of optical properties (reflection/ transmission) of SiO_2 coated with graphene might be related to the fact that the presence of graphene on SiO_2 increases the charge density at the surface which affects the induced dipole moment on the surface of SiO_2. As the graphene is 2D material, so the increase in the charge density is in the tangential direction and also the induced dipole moment of SiO_2.

6.3.2 Optical Constants Extraction and Evidence of Optical Anisotropy of Graphene

To derive reliable values for the optical constants (n, k) of 1L and 3L graphene samples the experimental reflectivity measurements have been fitted by simulating the interaction of an electromagnetic wave with the structure of the sample. This procedure can't be followed without taking into account the various critical parameters that can affect the convergence of the fitting process to meaningful results.

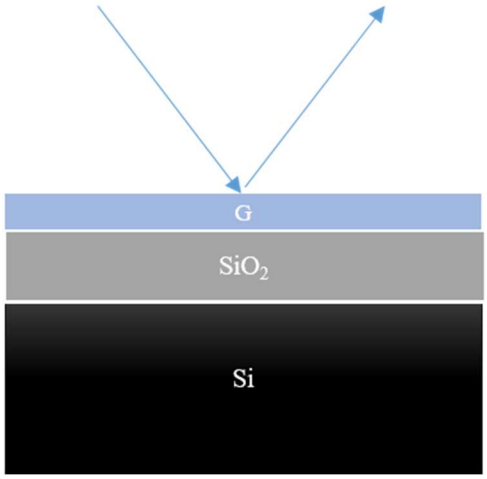

Figure 6.8: Three-layer optical model

The fitting procedure is based on the simulation of the sample structure by decomposing it into homogeneous layers corresponding to the elements, materials, and compounds constituting the sample, in this case from the bottom up to the surface exposed to the probing radiation: Si, SiO_2, G as shown in Figure 6.8. At each interface, the Fresnel coefficients for reflection and transmission of the incident fields according to the polarization state of the E.M. wave is recursively applied while the thickness of each layer is taken into account as a phase propagation and amplitude factor. IMD code [104] has been used for this purpose, assuming as unknown variables the real (n) and imaginary (k) coefficients of the complex refractive index. The code takes into account also the presence of non-ideal surface and interfaces through both a scattering coefficient affecting the amplitude of the fields for roughness and a refractive index continuous change between two adjacent layers for inter-diffusion and mixing. The fitting process is based on the Marquardt algorithm.

While the fitting procedure can be relatively straightforward in the case of ideal structures; however, in the present case, the nearly atomic layer thickness of graphene samples has to be properly considered. The E.M. wave interaction with 1LG and 3LG can't be simulated in principle by adopting a uniform homogeneous layer approximation since the atomic orbitals structure of the film plays a vital role for both interfaces and thickness. Keeping this fact in mind, we assumed that by the adopted approach we could derive only a sort of "effective refractive index" or better "effective optical thickness" where both material interaction thickness and refractive index are

included. Accordingly, the problem was to determine reliable, effective values both for the thickness and the refractive index being the two parameters strictly interrelated.

Graphene optical constants and the effective thickness of the layer have been derived by using the optical constants for Si layer reported in the IMD database and for SiO_2 layer those derived from recent independent measurements [122] discussed in chapter 5.

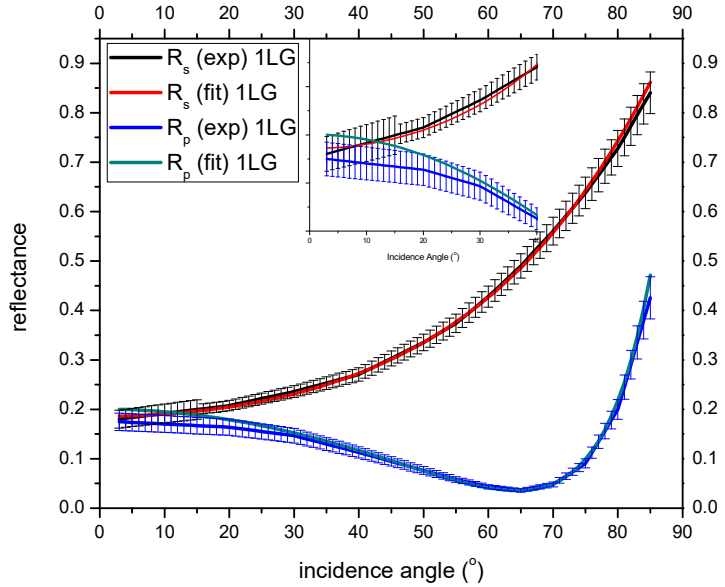

Figure 6.9: IMD fitting of 1LG/SiO_2/Si,s- and p- reflectance data measured for angle range (3-85°).

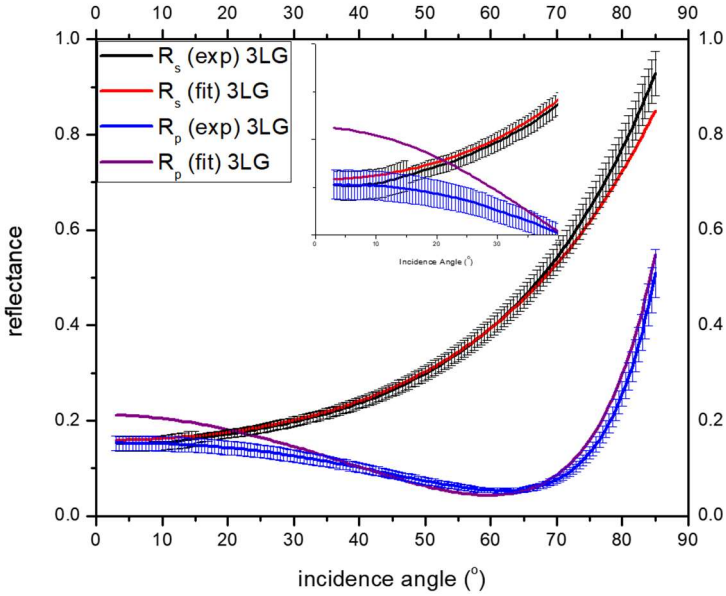

Figure 6.10: IMD fitting of 3LG/SiO_2/Si, s- and p- reflectance data measured for angle range (3-85°.)

Real (n) and imaginary (k) part of the graphene optical constants have been left free as fitting parameters for different fixed values of layer thickness. The best assessment of the thickness of graphene was based on the results derived from Raman spectroscopy data analysis and on the comparison of near-normal incidence fitting results, since the optical constants derived for s- and p- polarized radiation respectively should not depend on the polarization state for small incidence angles. By the mentioned analysis, the derived effective thickness range was for a 3LG sample within 1.4- 1.7 nm and 1LG sample within 0.34- 0.5 nm. Values of the effective optical constants corresponding to the reported effective thickness of 1LG and 3LG samples for s- polarized light are reported in Table 6.1. The different optical constants retrieved for the two 1LG and 3LG samples indicate clearly that the layer atomic orbitals structure strongly drives the interaction with the E.M. field; consequently, the two coatings can't be assumed like uniform homogeneous layers of different thickness of an optically "equal" material. In Table 6.1, effective optical constants values are reported along with uncertainty, which is directly associated with the uncertainty of thickness of graphene layers, the real part of the refractive index (n) values greater than 2 are associated with the negligible imaginary part of the refractive index (k) values. Figure 6.9 shows the s- and p- polarized reflectance experimental and fitted curves of 1LG for 0.34 nm effective thickness, and Figure 6.10 shows s- and p- polarized reflectance experimental and fitted curves of 3LG for 1.7 nm effective thickness. It can be observed that reflectance data are well fitted in the whole angle range (3-85°) in case of s- polarized reflectance with the same set of optical constants. The slight deviation of s- reflectance data for grazing incidence values observed in BEAR data for both samples, can be due to some alignment and related radiation scattering problem affecting the measurements.

Sample	n_s	K_s
1LG	2.65± 0.25	$<10^{-5}$
3LG	2.48± 0.14	$<10^{-5}$

Table 6.1: Optical constants retrieved from experimental data Rs of 1LG and 3LG for angle range 3-85°.

The fitting procedure in the case of p- polarized radiation does not converge with the unique derived set of optical constants in the whole angular range as can be seen in Figure 6.9 and Figure 6.10 the inset of both figures shows the problem in the fitting. Accordingly, the angular range was divided into several suitable smaller intervals, wide enough to allow reasonable confidence in the

convergence of the fitting procedure. This was the first indication of the optical anisotropy with a considerably more significant effect in the case of the 3LG sample. To the best of our knowledge, this is observed first time at hydrogen Lyman alpha in our study.

In fact, in the case of 1LG sample was enough to decompose the whole angular interval in just two angular segments; 3-40º & 40-85º, while for 3LG sample it was necessary to decompose it in seven intervals: 3-15º, 12-30º, 25-40º, 35-50º, 40-55º, 55-70º, 70-85º in order to get reasonably good fitting. In Figure 6.11 and Figure 6.12, the p- polarized reflectance fitting obtained for 1LG and 3LG samples are respectively reported. Extracted effective optical constants values corresponding to the fitting of 1LG and 3LG samples are respectively reported in Table 6.2 and Table 6.3. The value of n_s for 1LG reported in Table 6.1 and n_p (3-40º) reported in Table 6.2 is slightly different because the angle range is too big for near-normal approximation even though the values are within the uncertainty limit. It is evident for 1LG sample the considerable change for both the real and imaginary part of refractive index between the two angular segments, with a lower (n) and higher (k) values for grazing incidence angles showing greater absorption with lower refraction at the vacuum interface. However, in case of lower angles towards normal, 1LG sample shows no absorption as, (k) values approaches to zero. Thickness range was assumed from 0.34 nm to 0.5 nm for the fitting of 1LG data. For 3LG samples similar to the thinner 1LG sample, the (n) and (k) values remain respectively above 2 and negligible up to 40° incidence angle. For larger incidence angles, the (k) values progressively increase while the (n) values are significantly lower around the Brewster angle region.

Sample	$\boldsymbol{n_p}$	K_p
1LG (3-40°)	2.95± 0.25	$<10^{-5}$
1LG (40-85°)	0.19± 0.05	0.62±0.07

Table 6.2: Optical constants retrieved from experimental Rp data 1LG by IMD fitting for two different angular segments.

Angular segment	$\boldsymbol{n_p}$	K_p
3LG 3-15°	2.51± 0.14	$<10^{-5}$
3LG 12-30°	2.33± 0.11	$<10^{-5}$

3LG 25-40°	2.13± 0.09	$<10^{-5}$
3LG 35-50°	1.83± 0.05	$<10^{-5}$
3LG 45-60°	0.37± 0.035	0.64± 0.01
3LG 55-70°	0.51± 0.06	0.78± 0.01
3LG 70-85°	0.54± 0.06	0.82± 0.05

Table 6.3: Optical constants retrieved from experimental Rp data 3LG by IMD fitting for different angular segments.

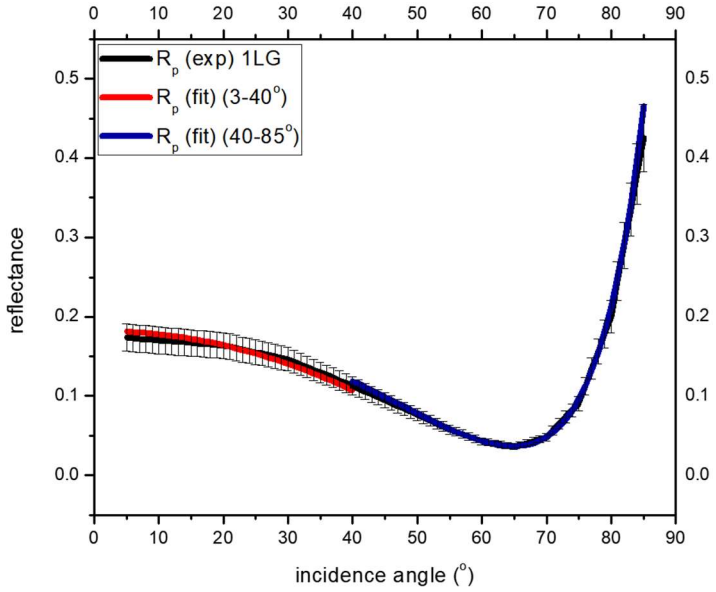

Figure 6.11: Comparison of IMD fitting of 1LG p- reflectance for different angular segments.

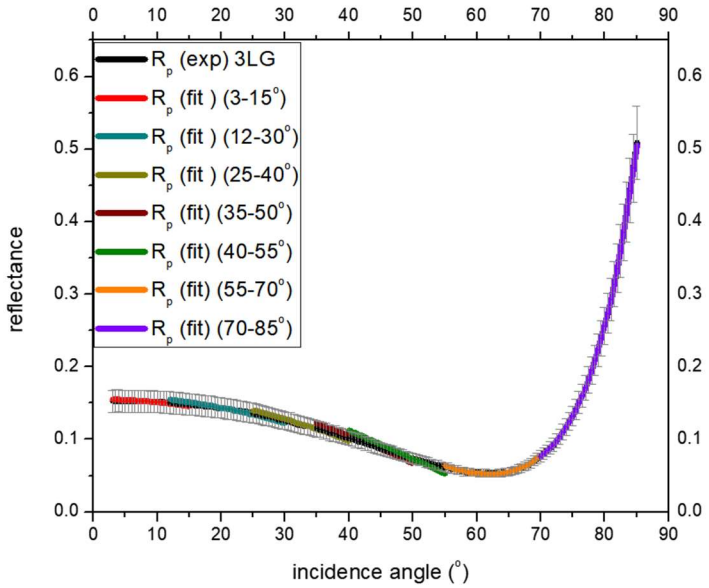

Figure 6.12: Comparison of IMD fitting of 3LG p- reflectance for different angular segments.

6.3.3 Qualitative Assessment of Data by Surface Differential Reflectance (SDR) Analysis

The problem emerging from these results is related to the quantitative estimation of the effect due to a very thin layer on a surface acting as a vacuum interface. This kind of problem is often treated as due to surface modification of the layer complex dielectric constant by using surface differential reflectance measurements (SDR). However, this technique, although very sensitive, need carefully prepared dedicated samples and very critical measurement. [123].

Although in this study case the SDR measurements were not performed directly due to the lack of suitable samples, the reflectance measurements have been compared in order to derive an indicative SDR curve and estimate the quality of results by comparison with theoretical predictions. Theoretically, SDR related to the film parameters by rather complicated mathematical expressions, especially in the case of anisotropic films. Thanks to the ultrathin thickness of graphene, it is possible to simplify the theoretical treatment significantly by applying a long-wavelength approximation (i.e., $d<<\lambda$). These relatively simple analytical relationships are especially beneficial for the determination of parameters of an ultrathin film based on SDR measurements. For the qualitative assessment of the retrieved (n) and (k) SDR for each polarization was calculated by following two ways and compared,

- using reflectance data of SiO_2/Si, $1LG/SiO_2/Si$, and $3LG/SiO_2/Si$

- using theoretical relations by incorporating retrieved optical constants.

The mathematical relations to derive SDR from the reflectance measurements for s- and p-polarized radiation are presented in eq. 6.1 and eq. 6.2 respectively. Correspondingly the SDR theoretical predictions derived from references [32] and [124] and given below in eq. 6.3 and eq. 6.4 corresponding to s- and p- polarization, respectively.

$$(SDR)_s = \left(\frac{\Delta R}{R}\right)_s = \frac{R_{sG} - R_{sSiO_2}}{R_{sSiO_2}} \tag{6.1}$$

$$(SDR)_p = \left(\frac{\Delta R}{R}\right)_p = \frac{R_{pG} - R_{pSiO_2}}{R_{pSiO_2}} \tag{6.2}$$

$$(SDR)_s = \left(\frac{\Delta R}{R}\right)_s = \frac{8\pi n_o \cos\theta_{in}}{(\varepsilon_o - \varepsilon'_{SiO_2})^2 + \varepsilon''^2_{SiO_2}} \left[(\varepsilon'_s - \varepsilon_o)\varepsilon''_{oG} - \varepsilon''_{SiO_2}(\varepsilon'_{oG} - \varepsilon_o)\right]\frac{d}{\lambda} \tag{6.3}$$

Where

$\theta_{in} = Incidencea\ angle$

$\varepsilon_o = 1 =$ Dielectric constant *of Vacuum*

$\varepsilon'_{SiO_2}, \varepsilon''_{SiO_2}$; Real and imaginary part of dielectric constant of SiO_2 respectively

$\varepsilon'_{oG}, \varepsilon''_{oG}$; Real and imaginary part of dielectric constant of graphene for ordinary wave (s- polarized)

As

$\varepsilon' = n^2 - k^2$ and $\varepsilon'' = 2nk$

$\Rightarrow \varepsilon'_{SiO_2} = n^2_{SiO_2} - k^2_{SiO_2}$ *and* $\varepsilon''_{SiO_2} = 2n_{SiO_2}k_{SiO_2}$

$\varepsilon''_{oG} = 0$; the imaginary part (k) for graphene ~ 0 *at* λ=121.6nm in case of ordinary wave,

$\varepsilon'_{oG} = n^2_{oG}$; n_{oG} = Real part of refractive index of graphene for ordinary wave

For p- polarized SDR theoretical approximation is written as

$$(SDR)_p = \left(\frac{\Delta R}{R}\right)_p = \frac{8\pi n_o d \cos\theta_{in}}{\lambda} \mathrm{Im}\left\{\left(\frac{\varepsilon_G - \varepsilon_{SiO_2}}{\varepsilon_a - \varepsilon_{SiO_2}}\right)\left[\frac{1 - (\varepsilon_o / \varepsilon_G\varepsilon_{SiO_2})(\varepsilon_G + \varepsilon_{SiO_2})\sin^2\theta_{in}}{1 - (1/\varepsilon_{SiO_2})(\varepsilon_o + \varepsilon_{SiO_2})\sin^2\theta_{in}}\right]\right\} \tag{6.4}$$

Where

$\varepsilon_{SiO_2} = \varepsilon'_{SiO_2} - i\varepsilon''_{SiO_2}$; *Dielectric* constant of SiO_2

$\varepsilon_G = \varepsilon'_G - i\varepsilon''_G$; Dielectric constant of graphene

$\varepsilon'_G = n^2_{pG} - k^2_{pG}, \quad \varepsilon''_G = 2n^2_{pG}k^2_{pG}$

Where; n_{pG}, k_{pG} are the optical constants of graphene retrieved by R_{pG} fitting by IMD

SDR experimental data have been derived from reflectance measurements of graphene coated and bare SiO_2/Si substrates for s- and p- polarized reflectance respectively. Experimental SDR data have been compared with theory by using the complex dielectric constants derived from the measured optical constants.

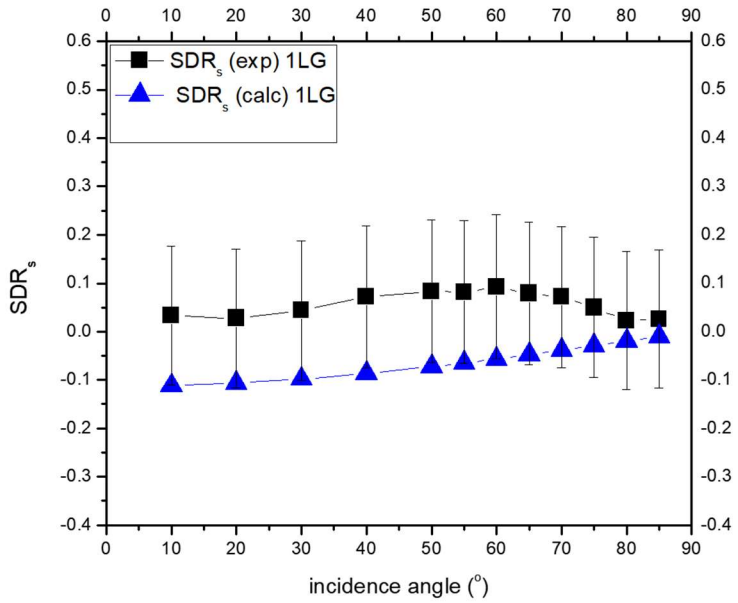

Figure 6.13: Comparison of 1LG (SDR)s experimental along with error bars and (SDR)s calculated theoretically using the retrieved optical constants of 1LG for thickness 0.34 nm.

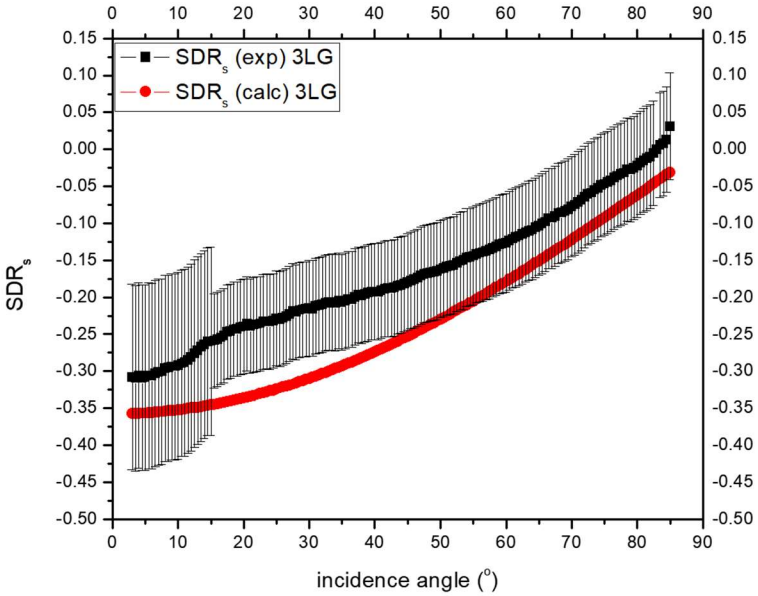

Figure 6.14: Comparison of 3LG $(SDR)_s$ experimental along with error bars and $(SDR)_s$ calculated theoretically using the retrieved optical constants of 3LG for thickness 1.7 nm.

The results are reported in Figure 6.13 and Figure 6.14 respectively for 1LG and 3LG s-polarized SDR comparison and in Figure 6.15 and

Figure *6.16* for p-polarized SDR for 1LG and 3LG, showing quite good agreement within the estimated uncertainty derived from the experimental source data, supporting in this way the approximation of the effect induced by the Graphene coatings with "effective" optical parameters. There is some discrepancy near the Brewster angle in case of 3LG experimental and theoretical SDR for p- polarization which might be because 3LG are expected to deviate considerably from the required ultrathin approximation for large incidence angles.

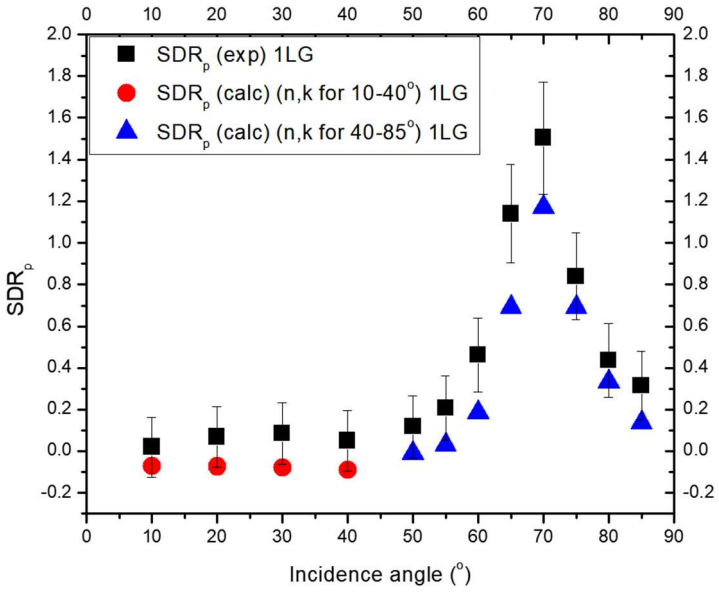

Figure 6.15: Comparison of 1LG $(SDR)_p$ experimental along with error bars and $(SDR)_p$ calculated by using the retrieved optical constants for specific angular segments of the reflectance data of 1LG for thickness 0.34 nm.

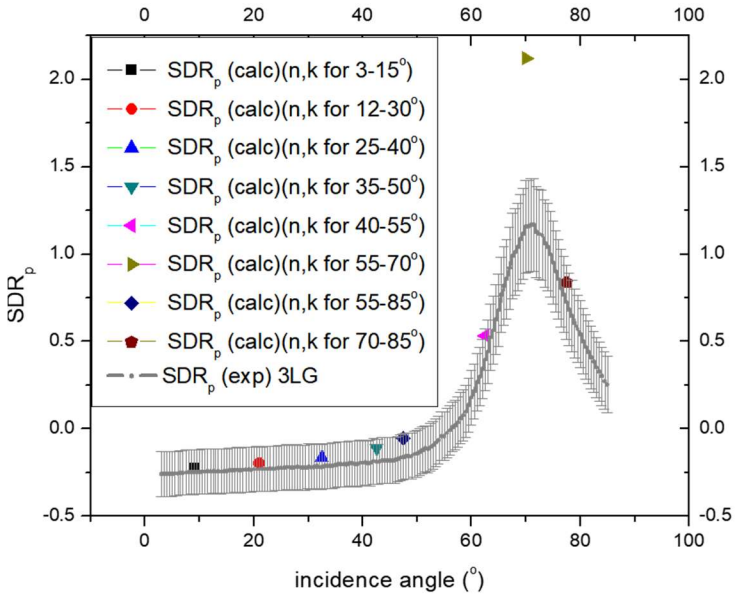

Figure 6.16: Comparison of 3LG $(SDR)_p$ experimental along with error bars and $(SDR)_p$ calculated by using the retrieved optical constants for specific angular segments of the reflectance data of 3LG for thickness 1.7 nm.

6.3.4 Brewster Angle Measurements and Analysis

It is observed in our study that the pseudo-Brewster angle of the bare SiO_2 differs from that of the substrate with graphene on top of it, which indicates the optical impact of atomically thin graphene on the optical properties of the underlying substrate. This phenomenon is technologically important and is used in Brewster windows for gas lasers, for photography and photographic glasses. As can be seen in Figure 6.5 and Figure 6.7, the downshift of the pseudo-Brewster angle of the substrate introduced by atomically thin layer (s) of graphene present on the substrate. Figure 6.6 indicates larger downshift in case of 3LG as compared to 1LG. As can be seen in Table 6.4, 1LG introduces ~1.5° downshift, and 3LG introduces ~5° downshift in the pseudo-Brewster angle at hydrogen Lyman alpha (121.6 nm). The downshift of the Brewster angle introduced by graphene is being reported first time in this study at hydrogen Lyman alpha. The shift in the Brewster angle of the dielectric substrate is because of the conductive nature of the graphene, which affects the polarization density and directions of the dipoles present in the dielectric substrate. As a result, the interaction of the substrate with the electromagnetic radiation modified. Schematic description of the classical Brewster effect and modified Brewster effect can be seen in Figure 6.17. [113]

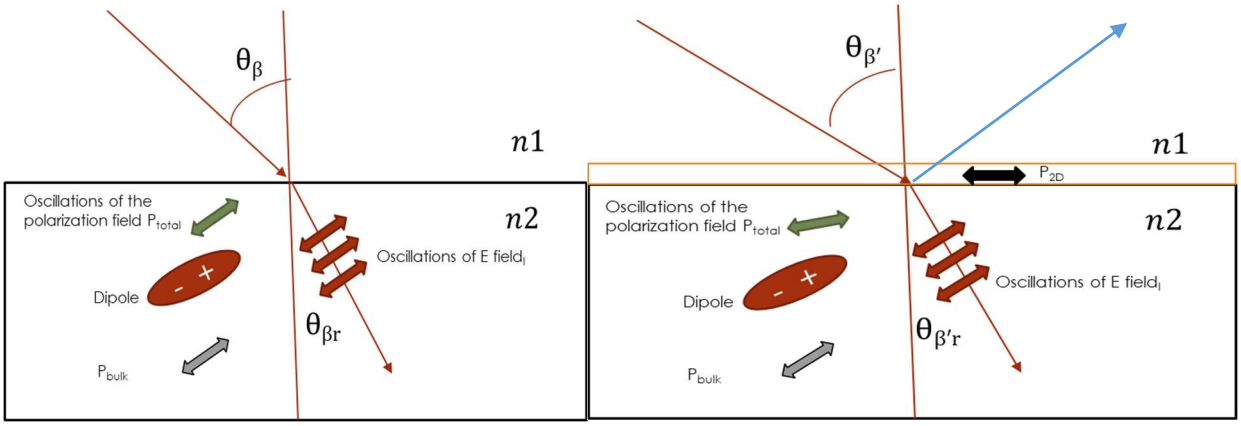

Figure 6.17: Microscopic explanation of classical Brewster effect (left) modified Brewster effect (right).

There is literature available describing the shift of the pseudo-Brewster angle in the presence of conducting 2D material on the dielectric substrate, but all these studies were in the UV/IR region [113], [125], according to our knowledge there is no data available in the VUV spectral region. In reference [113], the authors describe theoretically and experimentally the modification of the substrate Brewster angle in the presence of graphene and its relation with the conductivity of the 2D materials. Some authors in reference [125][126], showed that the real part of the graphene conductivity shifts p- reflection minima of the silicate glass 0.5° towards a wider angle. The small imaginary part of the conductivity take part and makes non-zero reflection minima resulting in the pseudo-Brewster angle of silicate glass. It is also showed in the literature that shift in the Brewster angle can be tuned by changing the Fermi level [113].

S. No.	Sample	Pseudo Brewster Angle
1.	SiO_2/Si	67.5°
2.	1LG/SiO_2/Si	65.1°
3.	3LG/SiO_2/Si	62.5°

Table 6.4: Pseudo Brewster angle comparison.

Larger downshift of the Brewster angle in case of 3LG is because of the higher conductivity (σ_g) 3LG than 1LG [127] [128].

In our study, interestingly downshift of the pseudo-Brewster angle was observed contrary to the reported upshift in the literature; however, in literature, it is reported for the different spectral region (UV- IR). The reason for downshift might be related to the spectral response and corresponding conductivity of graphene at the selected spectral line. As discussed in chapter 2 the

Brewster angle is related to direction or alignment of the electric dipoles present in the dielectric material with the incident light ray. Graphene present on the surface of dielectric modifies the direction of electric dipoles which results in the modification of the Brewster angle. The downshift might be because of the different interaction of light wave with the graphene orbital structure in case of VUV spectral region then in UV/IR spectral region We are working on this point to figure out the concrete justification of this and will report our findings to the scientific community.

6.4 Conclusions

Optical properties of monolayer and few-layer graphene over dielectric substrate were investigated experimentally at hydrogen Lyman alpha spectral line of VUV region, important for solar applications. The optical performance of the graphene samples over the dielectric substrate (SiO_2) was studied in terms of reflectance, Brewster angle, and effective optical constants corresponding to effective thickness of graphene layers. Optical anisotropy with the axis of symmetry nearly perpendicular to the surface and coherently related to the p- orbitals structural orientation has been demonstrated first time in this study at hydrogen Lyman alpha line. Optical anisotropy was explored in the case of both samples (i.e., 1LG and 3LG); however, relatively higher anisotropy was observed in case of the 3LG sample as compared to 1LG. Anisotropic 'effective optical constants' corresponding to the effective thickness of both samples of graphene (1LG and 3LG) determined first time to the best of our knowledge. Furthermore, the reliability of retrieved optical parameters was qualitatively analyzed by using surface differential reflectance analysis, which results in the good agreement of the retrieved data. Influence of the atomically thin graphene on the optical properties of the underlying dielectric substrate was evidenced in terms of modification of reflectance of SiO_2 and significant modification of pseudo-Brewster angle (-5° in case of 3LG and -1.5° in case of 1LG) of the dielectric substrate. Optical data analysis suggests, 1LG and 3LG samples are independently different materials because electromagnetic wave interacts with 1LG and 3LG differently.

Chapter 7. Time-Resolved Colliding Plasma Spectroscopy at The Collision Front of Two Colliding Plasmas

7.1 Introduction

Since the discovery of the Laser, it has been utilized for different applications. Being a focused high power source, it is the best tool to produce plasma by laser-matter interactions. Laser-produced plasmas (LPPs) have been the focus of substantial research interest since the 1960s [129]. LPPs have been used for a wide range of applications, e.g. material composition analysis by laser-induced breakdown spectroscopy (LIBS) [130], material deposition by pulsed laser deposition (PLD) [131], as a short wavelength light source [132], high harmonic generation, [133] and laboratory-scale demonstration of astrophysical plasmas [134]. These applications of LPPs have provided great opportunities for research in the advancement among the mentioned areas. Since all stars are made up of plasma, the study of the LPP expansion helps to understand some astrophysical phenomena. The subdomain of the LPP is the colliding laser-produced plasmas (CLPP) which opens up new and improved opportunities to utilized LPP in different technological domains. CLPP aroused interest because of the need to understand the collision processes that occur in space, e.g., collisions of stars, galaxies, etc. at the laboratory scale. Moreover, it is proved that the possibility of plasma collision and interaction of the two plasmas causes the improved application of LPP, e.g., it has been shown in ref [135] by using CLPP the deposited film quality improved in PLD. It is also demonstrated that reheating of the plasma created by the pre-pulse increases the signal to noise ratio as well as the emission in the spectral area of interest in LIBS [136]. Reheating the already created plasma by another laser pulse also shows improvements in the plasma characteristics, because of the fact that the free electrons present in the already created plasma absorb laser light and have better light coupling and as a result, energy, and temperature of the plasma increases. In the subsequent sections, there is a brief description of different LPP applications.

7.1.1 Laser-Induced Breakdown Spectroscopy (LIBS)

Among the variety of different technological areas where LPP is being utilized the most extensive use of LPP is in laser-induced breakdown spectroscopy (LIBS) [137]. It is the spectroscopic technique to study the material composition using the emitted light from the laser-produced plasma. In LIBS a laser is focused on the material to be investigated to produce plasma, and the light emission from plasma is focused on to the spectrometer to spectrally resolve the emission lines of the plasma. As the spectral lines are the characteristics/ fingerprint of the elements of the target material by analyzing them, the composition of the material can be determined. Apart from the composition analysis, LIBS can also be used for the quantitative studies of the elements of the target material. This can be achieved if the spectrometer is already calibrated w.r.t. intensity by known concertation of the interested elements. In this way by comparing the measured spectrum with the known spectrum the mass ratios between different elements can be determined. At the industrial scale, this technique can be useful for quality control processes. LIBS is a very useful technique and has a great potential for space applications and has already been used on the Curiosity Rover on Mars, to study the composition of the material during space missions.

7.1.2 Laser Produced Plasma as A Light Source

The laser-produced plasma consists of several ionization stages of elements and emits characteristics spectral lines depending on the target materials, laser energy, pulse duration, etc. This creates an excellent opportunity to use plasmas as a light source of the desired spectral wavelength. This can be achieved by detailed studies of laser-plasma spectroscopy of different materials. One of the most important applications of LPP is the generation of short-wavelength (EUV) light source for EUV lithography [132]. As the atoms in a neutral state cannot emit in the EUV, the hot dense plasma can be an excellent source of multi-charged ions which can produce EUV radiation. As mentioned at the start of this thesis that most stable and reliable sources of short wavelength are the Synchrotron light sources which are huge facilities and used for the study of fundamental science. To use the short-wavelength for industrial and laboratory applications, LPP is the most suitable option and has made EUV lithography commercially viable. High reflective optics containing Mo/Si multilayer mirrors for 13.5 nm wavelength have been developed for this purpose. EUVL industry set a requirement for the source of maximizing emission centered at 13.5 nm within a 2% bandwidth [131]. LPP studies of Tin (Sn) shows promising results for EUVL

industry because of having unresolved transition arrays (UTA) in the wavelength region of interest as a result of Sn VII - Sn XIV ions contributing in the 2% band at 13.5 nm. The conversion efficiency (CE) of the LPP created by a 10 ns, Nd: YAG laser, focused to 60 μm onto a Sn target is reported to be 2.04% [138]. CE is the ratio of energy emitted in the 2% bandwidth to the input energy of the laser.

The lower value of the CE is because of the fact that the ions absorb the EUV light they emit, and neutralization of ions by electrons in the plasma to lower charge states. As a result, the efficiency of light generation for lithography is reduced at higher plasma power density.

To achieve high CE, different techniques were adopted, e.g., reheating of the already created plasma by a longer wavelength laser proved better results in conversion efficiency. An example of this technique is demonstrated in [139], where an increase of CE was achieved by focusing the CO_2 laser into a plasma created by a Nd: YAG. It has been shown that reheating of the stagnation layer, rather than the typical pre-pulse plasma, can lead to a higher CE (3.6%) [140]. The stagnation layer was achieved as a result of the collision of two plasmas generated by splitting the Nd: YAG into two parallel pulses. The second laser was focused into the stagnation layer to get the improved CE. The experiment arrangement discussed in this section has a similar experimental procedure without reheating the stagnation layer.

Apart from lithography, the short-wavelength light sources are also beneficial in microscopy to resolve smaller features. A spectral region famous for the study of biological samples is called the water window (2.33- 4.4 nm). In this spectral region, the light is absorbed by carbon but not by oxygen which results in a good absorption contrast for biological samples.

7.1.3 Pulsed Laser Deposition (PLD)

Pulsed laser deposition is the physical vapor deposition process for thin films. In this process, a laser is focused onto a target material, and the plasma generated because of the laser-matter interaction expands in space, and the material is deposited on the desired substrate [141]. In this process only a small fraction of material is ablated in response to each laser pulse; resulting better control of material deposition on the substrate. Moreover use of second laser in the PLD process shows improved material properties of the deposited films, as the second laser additionally evaporate smaller nanoclusters in the laser-plasma [142].

7.2 Colliding Laser-Produced Plasmas (CLPP)

When two plasmas expand in space in close proximity, they interact with each other through collisions, and two possibilities of interaction exist, i.e., interpenetration and formation of stagnation layer. Stagnation layer is the region formed by the accumulation of the plasma plume material at the collision front of two counter-propagating plasmas. If the two seed plasmas have relatively large velocity and modest density at the region of collision the two plasma plumes tend to interpenetrate. However, if the relative collision velocity of the two counter-propagating plasmas is small, the constituents of the plasma plume tend to decelerate quickly at the collision area, which results in the accumulation and formation of stagnation layer [143]. The crucial factors or features describing the plasma within this region include the density, temperature, geometry, composition, and dynamics. The stagnation layer of the two counter-propagating plasmas offers improved control over the plasma characteristics (density, temperature, etc.) as compared to a single seed plasma [144] [143]. It is reported that the temperature of colliding plasma stagnation layer is slightly higher than the single seed plasma at a same delay time after laser shot [144]. The electron density is more uniform than in the case of a single plasma [143].

The interaction of the two plasmas depends on their separation, d, and the ion-ion mean free path, λ_{ii}, of the ions within the plasmas. The two plasmas can either interpenetrate without interaction, or they can collide and form a stagnation layer. The result will depend on the collisionality parameter [145]:

$$\xi = \frac{d}{\lambda_{ii}} \tag{7.1}$$

It is necessary to distinguish between two different ion-ion collision mean free paths, for ions inside the same plasma, $\lambda ii\ (1 \rightarrow 1)$, and for ions in the two plasmas which are colliding, $\lambda_{ii}(1 \rightarrow 2)$. The ion-ion mean free paths are given by [146]:

$$\lambda_{ii}(1 \rightarrow 1) = \frac{(kT_i)^2}{4\pi Z^2 e^4 n_1 \ln \Lambda_{11}} \tag{7.2}$$

$$\lambda_{ii}(1 \rightarrow 2) = \frac{(m_i \upsilon_{12}^2)^2}{4\pi Z_1^{\,2} Z_2^2 e^4 n_2 \ln \Lambda_{12}} \tag{7.3}$$

where T_1 is the plasma temperature, Z is the average charge stage, n_1, n_2 are the respective plasma densities, and $\ln\Lambda_{11}$ is the Coulomb logarithm of the plasma. The Coulomb logarithm is defined as $\ln\Lambda = b_{max}/ b_{en}$, a ratio of the small impact parameter for large-angle scattering b_{min} and large impact parameter for small-angle scattering b_{max}. It is a good approximation to take the maximum distance at which a particle is scattered to be the Debye length, $b_{max} = \lambda D$, and for b_{min} the distance of closest approach for the scattering of two ions. In this case, the Coulomb logarithm can be expressed as [147]:

$$\ln \Lambda_{12} = 43 - \ln\left[\frac{Z_1 Z_2 (M_1 + M_2)}{M_1 M_2 (\upsilon_{12}/c)^2}\left(\frac{n_e}{T}\right)^{\frac{1}{2}}\right] \tag{7.4}$$

with M_1 and M_2 being the atomic masses of the ions colliding, v_{12} the relative velocity of ions colliding, c the speed of light, Z the charge stage, n_e the electron density (cm^{-3}) and T the temperature. The strength of the effects in the stagnation layer depends on the collisionality parameter. The collisionality parameter is highly dependent on the relative velocity of the collision of two seed plasma and comparatively less dependent on the mass of ions. Therefore, it is possible to tune the collisionality parameter by two different approaches, i.e., the angle between the two seed plasmas and changing the target materials [143]. When fast-moving plasmas of low density collide, they interpenetrate, and collisions between ions of the different plasmas are negligible. Time-resolved fast imaging is very useful for study the dynamics and characteristics of the stagnation layer or colliding plasma of different materials [148].

7.3 Time-Resolved Plasma Spectroscopy Experiment

Time-resolved plasma spectroscopy of the colliding plasma stagnation layer is very useful to study the dynamic processes occurring in the plasma. This spectroscopic technique can give detailed information about the plasma's properties. Spectral line identification gives information about the different charge states present in the plasma, which in turn can give information about the temperature of the plasma. Using time-resolved spectroscopy the time evolution of the different charge states which are present in the plasma can be studied. The line width of the spectral lines is also useful to study the plasma characteristics in detail. In this chapter, the results of the time-resolved plasma spectroscopy of Al-Al, Al-Si by using flat and wedge-shaped targets will be discussed in the subsequent sections.

7.4 Experimental Setup and Methodology

The time-resolved plasma spectroscopic experiments were performed in a cylindrical vacuum chamber of 50 cm diameter, with 8 equidistant ports on the wall of the cylinder. In order to perform the experiment in a vacuum, the chamber was connected with a rotary pump (Leybold D8B) and a turbomolecular pump (Edwards EXT 250). With the help of these pumps, the base pressure of the chamber was maintained at 3 x 10^{-6} mbar. Inside the chamber, there is a laser focusing lens attached to the translational stage to focus the laser on the target material. Figure 7.1 shows the photograph of the cylindrical chamber with the labeling of the main components. The target holder is attached with three linear stages and Zaber actuators in order to have motion of the target holder in x-y-z-direction. Inside the chamber apart from the x-y-z translation stage target holder and laser focusing lens, there is another lens which focusses the plasma onto the spectrometer slit. This lens position is very critical because a minute misalignment can change the results drastically. This lens position is adjustable with a micrometer screw gauge. There is a dove prism in between the stagnation layer focusing lens and the slit of the spectrometer. The purpose of the dove prism is to invert the stagnation plasma on the slit as can be seen in Figure 7.2.

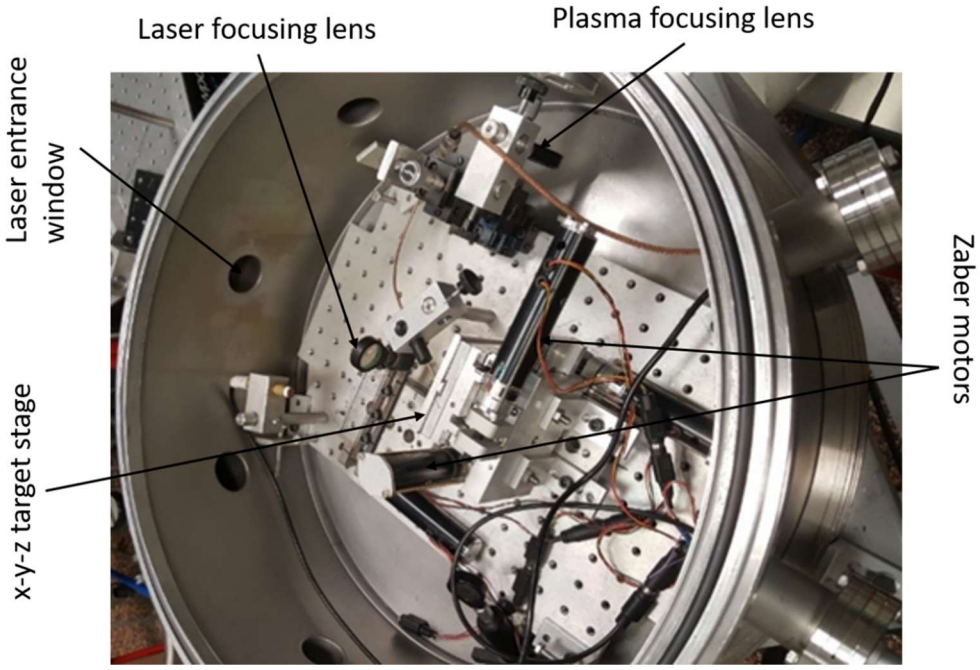

Figure 7.1: Picture showing the real view of the experimental chamber used for CLPP spectroscopy experiment.

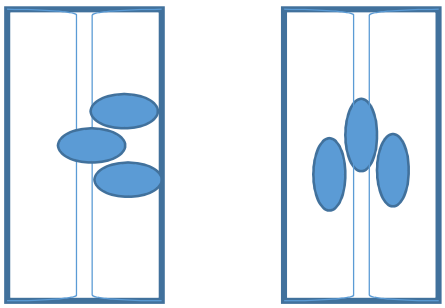

Figure 7.2: Function of dove prism: schematic view of the plasmas at the entrance slit of the spectrometer; (left) without dove prism (right) with dove prism.

A 2º wedge prism is used to split the laser pulse into equal half intensities; this wedge prism is placed outside the experimental chamber before the entrance window. The schematic of the wedge prism is shown in

Figure 7.3 . Its alignment is also critical, and it is aligned carefully to split the laser beam equally in two parts. The energy of the laser pulse before the wedge prism and after it was split into two beams was measured using a Litron Energy Monitor.

An EUV reflectometer is connected at 45° w.r.t to the target for EUV spectroscopy experiment. A visible spectrometer is placed just outside the experimental chamber perpendicular to the target. A high-speed ICCD camera was placed at the focus of the spectrometer for plasma spectral imaging. The schematic of the complete experimental setup is shown in Figure 7.4.

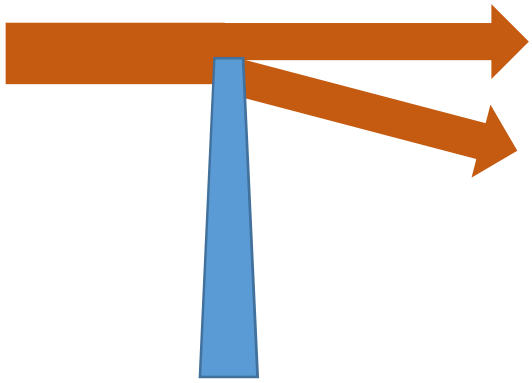

Figure 7.3: Schematic of the wedge prism showing its function.

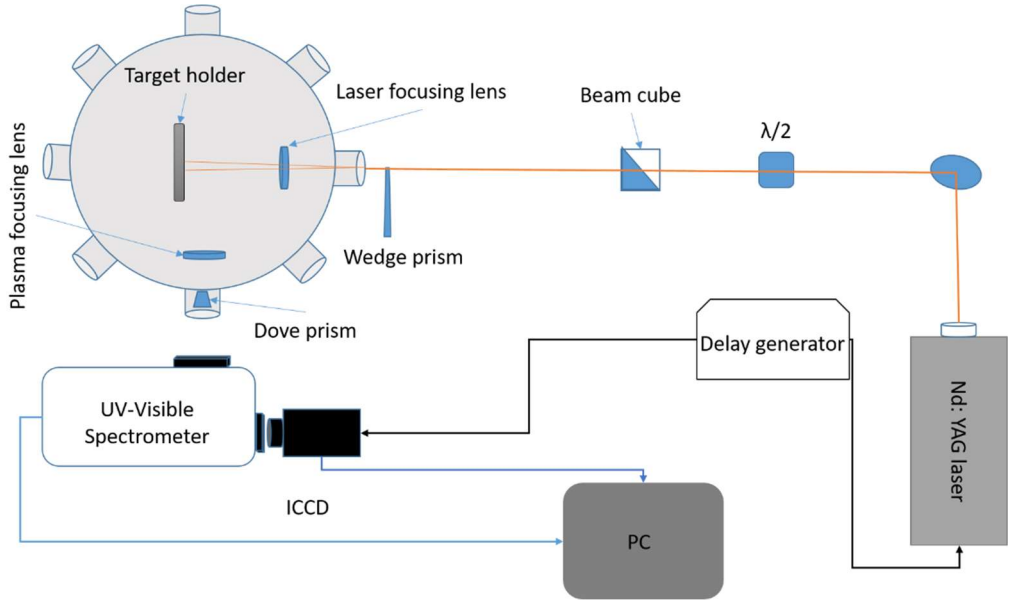

Figure 7.4: Schematic of the complete experimental setup used for CLPP spectroscopy experiments.

The software used to control the actuator movements was an in-house made Visual Basic code. The software recognizes the maximum travel of the connected actuators in mm with the startup of the software and gives information about the position to the user.

7.4.1 The Laser System

Nd: YAG Continuum Surlite III-10 [24] laser was used for the experiments. It is a Q-Switched nanosecond laser system. The Nd: YAG laser is based on neodymium-doped YAG (yttrium aluminum garnet) crystals as a gain medium. A Kr or Xe flash lamp excites atoms to higher energy levels, where they quickly relax to an intermediate level with a much longer lifetime. A simple level diagram of a 4 level laser system is shown in Figure 7.5. To achieve lasing, spontaneously emitted photons need to pass through the medium where population inversion has been created. The gain medium is put into a cavity, which ensures many passes of the photons through the gain medium and maximizes the energy output of the laser. The typical pulse energy of the laser system is ~ 1000 mJ and pulse duration is 6 ns. The pulse energy can be controlled by varying λ/2 plate angles. The laser energy used in the experiments discussed in this chapter was around 480 mJ which was equally divided into two beams of around 240 mJ each colliding laser plasmas.

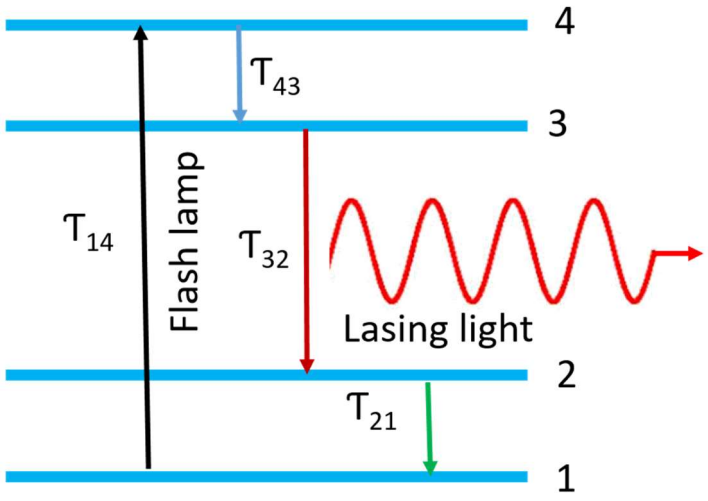

Figure 7.5: Energy level diagram of the laser.

The laser pulse was passed through a λ/2 plate, which rotates the polarization of the pulse by 2θ, where θ is the angle between incoming polarization and polarization plane of the plate. The pulse then passed through a polarized beam cube which is a beam splitter that transmits p- polarized light and reflects s- polarized light.

7.4.2 Hamamatsu ICCD

A Charge-Coupled Device (CCD) is a very sensitive photon detector. In a CCD, the photodetector is divided into a large number of small parts known as pixels which can be used to create an image of the scene of interest. Charged-couple devices (CCDs) are light detectors made by using semiconductor technology. When light falls onto a pixel, it creates electrons that sit in the potential well of the given pixel. An applied voltage to each pixel gate allows the transfer of electrons in the well to a readout unit. The voltage is applied in a specific order across all the pixels, which makes it possible to read each pixel individually and record the number of electrons produced within each pixel. In this way, it is possible to spatially resolve the intensity of the light falling onto the CCD. There are some limitations to CCDs, i.e., speed of CCD readout, the efficiency of conversion of photon into electrons. In order to take the measurements of very short readout times or low-intensity light signal, intensified charged couple devices (ICCDS) are used. An ICCD detector is basically the CCD detector with an image intensifier added in front of the CCD. An image intensifier contains a photocathode, multichannel plate (MCP), phosphor screen and a fiber optic bundle which is used to carry the light from the phosphor screen to the CCD device. The

electrons created at the photocathode are accelerated towards the MCP because of the reverse bias applied between the photocathode and MCP with a square pulse. These electrons are then amplified and hit the phosphor screen. The created light signal at the phosphor screen is then transferred to the CCD detector through optical fibers. The duration of the applied square voltage pulse determines the gate time of the camera, or shutter speed, thus enabling very short snapshots. A schematic example of the image intensifier is shown in Figure 7.6. In work presented within this thesis, a Hamamatsu C7164-03 ICCD camera was used [25]. The camera was externally triggered using the same delay generator that was used to trigger the laser. By changing the delay time between the laser trigger and the camera trigger signals it was possible to temporally move the start of the camera gate.

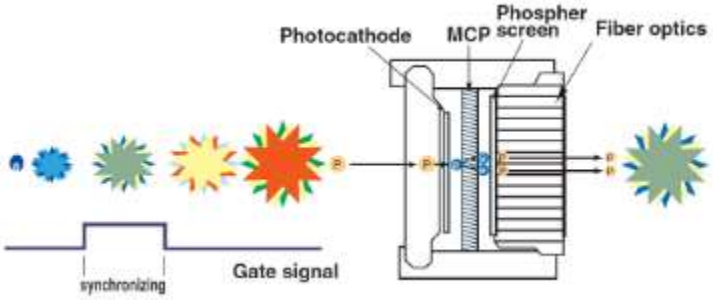

Figure 7.6: Schematic of the ICCD process [149].

The spectral emission from the laser-produced plasma after passing through the UV/ visible spectrometer was imaged onto the Hamamatsu ICCD camera.

7.4.3 UV- Visible Spectrometer

Time-resolved plasma spectroscopy of LPP experiments was performed using Acton SP-2756 UV-Visible spectrometer of Princeton Instruments [25]. The spectrometer is based on a Czerny-Turner configuration, with two spherical mirrors and a symmetric design. The light from the plasma was focused onto the entrance slit of the spectrometer using an uncoated BK7 Plano-convex lens with a focal length of 100 mm. The entrance slit of the spectrometer can be varied using a micrometer screw guage, thus enabling control of the instrumental broadening. Throughout the experiments, the entrance slit was kept fixed. After passing through the slit, the light was reflected onto a spherical collector mirror, which collimate the input light onto a grating. The aperture ratio of the system was f/9.7, and the grating size was 68x68 mm. The spectrometer had 3 different gratings, 300 grooves per mm, 1200 grooves per mm and 2400 grooves per mm. In this work, only the 300

grooves per mm gratings were used, and wavelength range 370-426 nm was covered. After falling on the grating, the light dispersed onto the second spherical mirror which focused the light towards the exit port of the spectrometer. At the focal plane of the second mirror, the Hamamatsu ICCD was placed as a detector. A diagram of the spectrometer is shown in Figure 7.7.

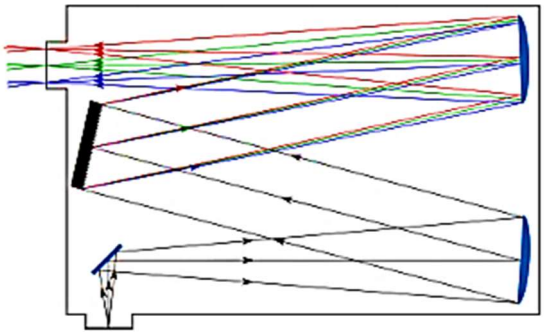

Figure 7.7: Schematic of the UV- visible spectrometer.

A mercury lamp was placed at the entrance of the monochromator to align the Hamamatsu camera and the monochromator. The zeroth-order diffraction was used to place the camera in the focus position of the second spherical mirror of the monochromator. The spectrometer is stigmatic, which thus gives us the spatial resolution of the emitting plasma.

7.4.4 Plasma Alignment With the Spectrograph

The alignment of the colliding plasma stagnation layer with the spectrograph was done using the plasma focusing/imaging lens. The alignment procedure was done in the air instead of vacuum in order to avoid opening the chamber to break the vacuum and close again at each step. Figure 7.2 shows how the dove prism was used to align the expanding plasma relative to the slit. The focusing lens was scanned horizontally in order to see the three plasmas step by step. First, the lens was positioned in such a way that the seed plasmas were just to one side of the slit. The lens scanning was performed in very small steps with the help of a micrometer screw gauge. By moving the lens position, we reach at a point where the first seed plasma appears. By moving further, we reach a point where we see only the stagnation layer, this position was marked. By moving the focusing lens further, we reach a point where we observed the second seed plasma. All the positions were marked for further verification in vacuum. The scanning was carried out in small steps, and at each step the spectral image was taken. The sequence of images on the Si-Si flat target taken during scanning the plasma focusing lens is shown in Figure 7.8. The alignment was also verified in the

vacuum configuration by fixing the focusing lens at the marked position of all three plasmas. Before each experiment these steps were repeated in order to confirm the alignment.

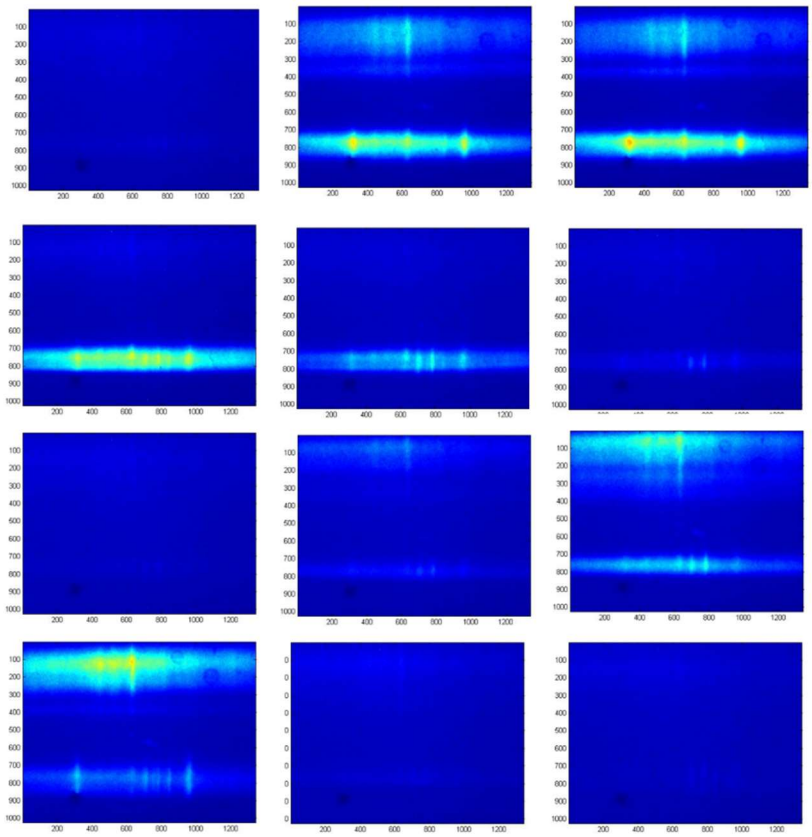

Figure 7.8: Spectral images taken during scanning of the plasma imaging lens which focuses the stagnation layer on the entrance slit of the spectrograph. In each case, the upper spectrum is caused by air plasma.

7.5 Results and Discussion

The time-resolved colliding plasma spectroscopy experiments were carried out using the experimental setup discussed earlier. In this experiment, two plasmas of elements (Al or Si) were produced in close proximity so that they collide as they expand and form a stagnation layer at their collision front. As well as using different target materials, two different geometrical configurations of the target, i.e., flat and 90° wedge were used to study the dynamics of plasma and stagnation layer. Target detail (material, shape, etc.), laser measurement parameters are represented in Table 7.1

S. No	Samples	Target shape	Camera Integration time	Delay Time scan
1	**Al-Al**	**Flat**	50 ns	150- 500 ns
2	**Al-Al**	**Wedge**	50 ns	150- 500 ns
3	**Si-Al**	**Flat**	100 ns	150- 500 ns
4	**Al-Si**	**Wedge**	100 ns	150- 500 ns

Table 7.1: Target material along with the experimental parameters.

Figure 7.9: Wedge target holder used in experiments.

Wedge target holder, which was used in experiment, is shown in Figure 7.9. All the measurements were carried out in a vacuum and using 300 grooves/mm grating. With this grating a spectral window of~56 nm can be observed, so the experiments were performed for the spectral window (370- 426 nm) containing a number of prominent lines in Al and Si. All the spectral images were recorded for delay time scan (150- 500 ns) relative to the laser pulse with a step of 10 ns delay at fixed integration time in order to study the time evolution of different ion stages.

The spectral data were calibrated using the available NIST database. Some of the possible ion stages of Silicon and Aluminium in the spectral range 370-426 nm from NIST database are presented in Table 7.2 and Table 7.3, respectively. The spectral curves were retrieved from each image data by summing up its rows using Matlab code. In the subsequent sections, the spectral data retrieved from the time-resolved spectral imaging is presented. Analysis of the data in terms of spectral assignments, time evolution of different ion stages and their comparison w.r.t. target

geometry is presented. Moreover, the electron number density is also estimated, and comparison is also discussed later in this chapter.

Ion stage	Wavelength (nm)	Ion stage	Wavelength (nm)
Si IV	376.24	Si III	392.44
Si IV	377.31	Si IV	408.88
Si III	379.14	Si IV	411.61
Si III	379.61	Si II	412.80
Si III	380.65	Si II	413.09
Si II	385.60	Si II	418.33
Si II	386.26	Si II	419.07
Si I	390.55	Si II	421.24

Table 7.2: Some of the possible Silicon ion stages present in the spectral range 370-426 nm taken from the NIST database [150].

Ion stage	Wavelength (nm)	Ion stage	Wavelength (nm)
Al III	370.21	Al I	396.15
Al III	371.31	Al III	398.01
Al IV	372.59	Al II	399.63
Al II	373.80	Al II	400.57
Al II	375.31	Al II	402.65
Al IV	380.58	Al III	408.86
Al II	385.93	Al III	415.01
Al II	386.61	Al III	418.97
Al II	390.06	Al IV	419.04
Al IV	391.39	Al II	422.75
Al I	393.56	Al II	424.07

Al I	394.40	Al I	425.51

Table 7.3: Some of the possible Aluminium ion stages present in the spectral range 370-426 nm taken from the NIST database [150].

7.5.1 Comparison of Time-Resolved Colliding Plasma Spectroscopy of Al-Al Flat and 90° Wedge Target

In this section, the comparative study of Al- Al stagnation layer in case of a flat target and wedge target is presented.

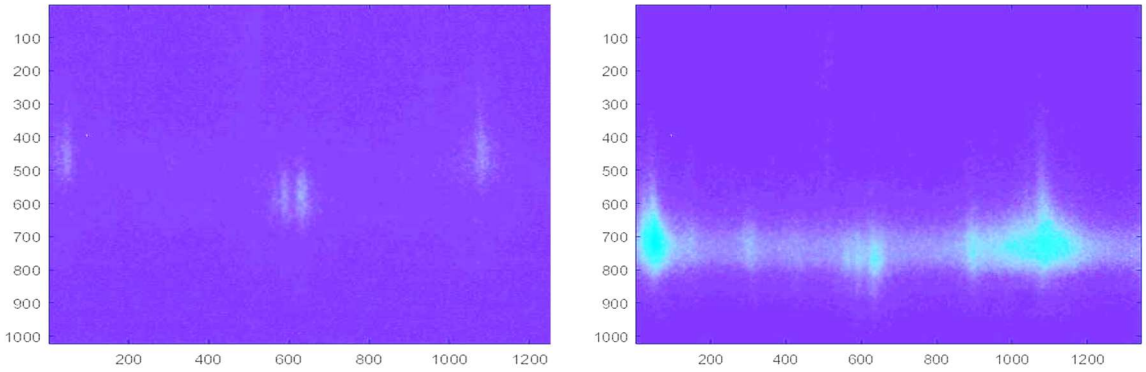

Figure 7.10: ICCD images of the Al-Al stagnation layer at delay time 340 ns and integration time 50 ns; (left) flat target (right) 90° wedge target..

The raw ICCD images of the stagnation layer of Al- Al flat and wedge targets for the same delay time are presented in Figure 7.10 which clearly indicates the emission is more intense in the case of wedge shaped target as compared to flat target.

Figure 7.11 shows the spectral data of the Al-Al colliding plasma in the case of flat and wedge targets for delay times of 340 ns and 440 ns along with the spectral assignments of the emission lines. By comparing it is clear from Figure 7.11, the spectral emission in the case of a wedge target is more intense than in case of the flat target. As expected, higher ionization appears in earlier times and decreases as emission from the lower ion stages increases.

Figure 7.12 and Figure 7.13 show the comparison of the Al-Al flat and wedge target time resolved spectroscopic results plotted as two different types of plots in order to clearly observe and present the time evolutions of different ion stages. From the time-resolved spectroscopic results of the stagnation layer of Al-Al- flat target, it can be observed that higher ionization stages (Al III @

371.3 nm, Al III @ 415 nm, Al IV @391.3 nm) appears at earlier times along with Al-I triplet and grows until 340 ns delay time and then fade out with time. However lower ionization Al-I triplet (Al- I @ 396.1 nm, Al- I @ 394.4 nm, Al-I @ 393.5 nm) appears at earlier times along with Al-III and keep growing until 440 ns and then start decreasing but remain dominant.

However, in case of Al-Al wedge target, it can be observed from the above data that at earlier times the higher ionization stage Al III at 415 nm appears first, grows and peaks at 340 ns and then decreases rapidly. It is entirely absent at 500 ns while emission from Al I at (393-396 nm) is still very much present. While these neutral lines do appear at early times also they are not as intense as the ion lines and indeed do not peak until the later time of 440 ns. Over all emission in the case of the wedge targets is much stronger than the flat target which is also clearly evidenced in Figure 7.10.

In Figure 7.14, the peak emission of selected ion lines is tracked over the time period concerned and then plotted as peak intensity against time. This clearly demonstrates how one ion stage grows at the expense of another and that higher ion stages appear earlier.

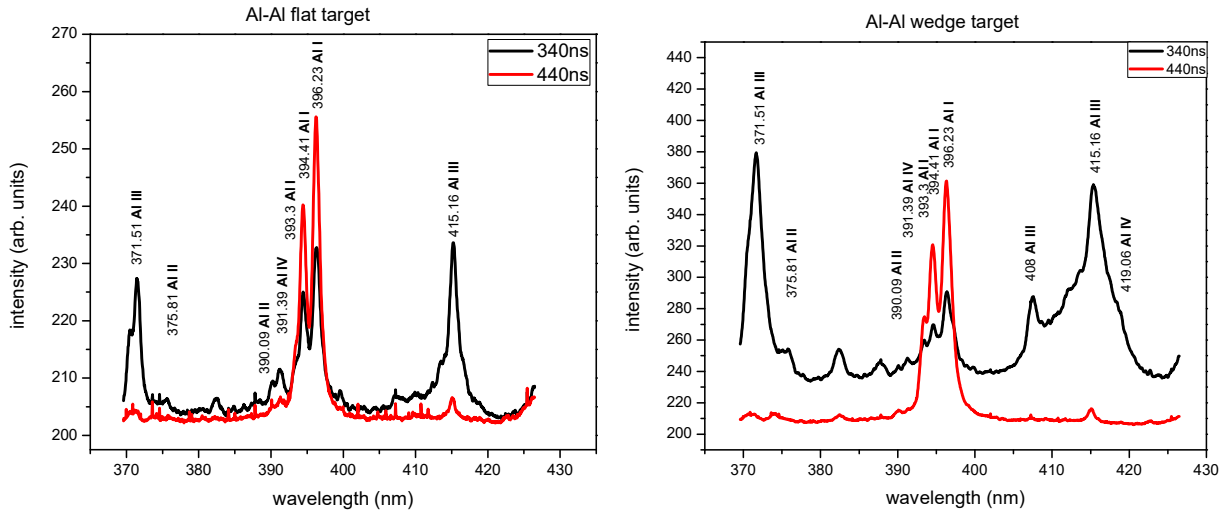

Figure 7.11: Comparison of UV- Visible time-resolved spectrum of the Al-Al stagnation layer for delay time 340 ns and 440 ns: (left) flat target (right)90° wedge target.

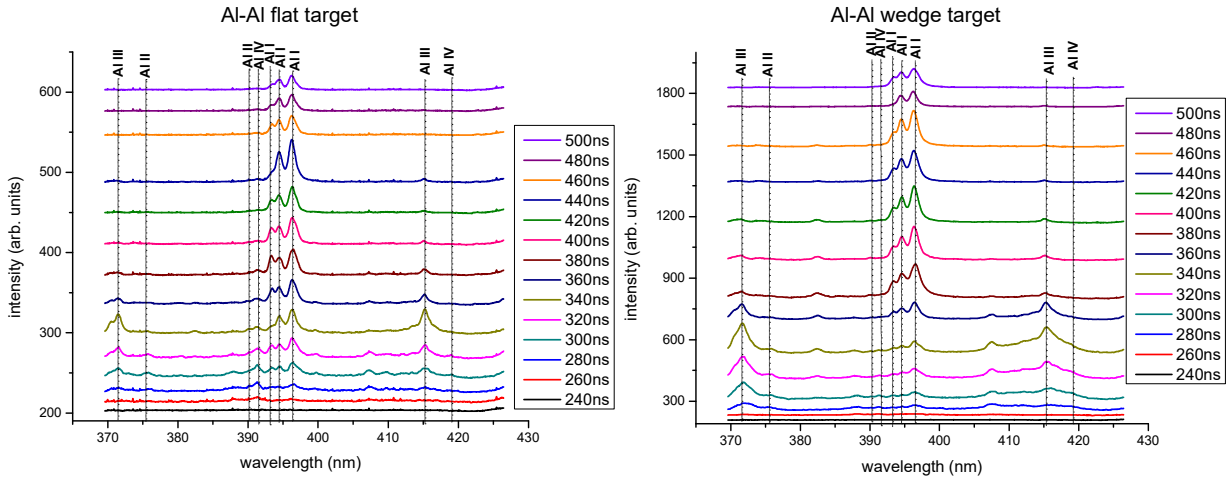

Figure 7.12: Layer plot: UV- Visible time-resolved spectrum of the Al-Al stagnation layer for delay time 240-500 ns at integration time 50 ns; (left) flat target (right)90° wedge target.

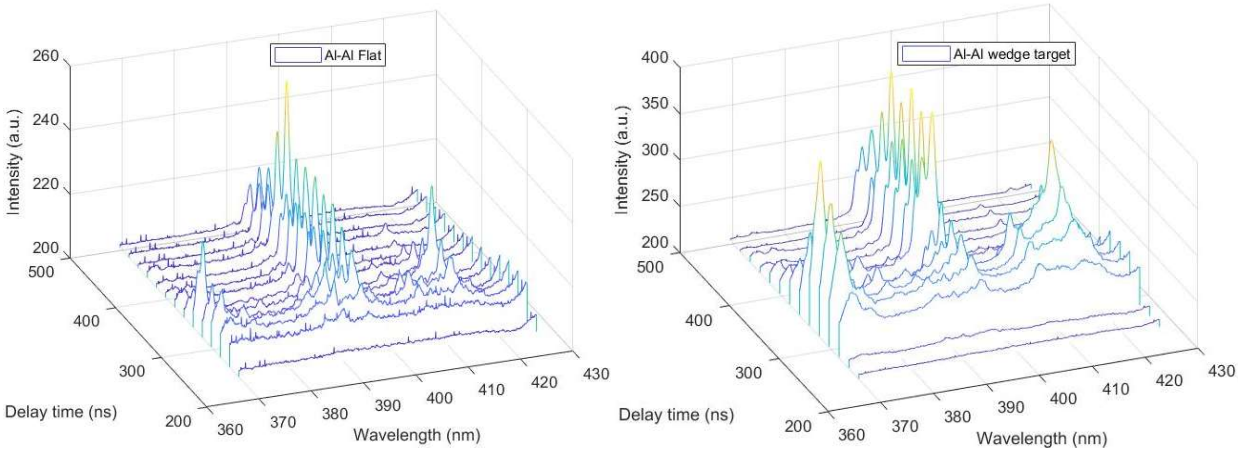

Figure 7.13: Waterfall plot: UV- Visible time-resolved spectrum of Al-Al stagnation layer for delay time 240-500 ns at integration time 50 ns: (left) flat target (right) 90° wedge target.

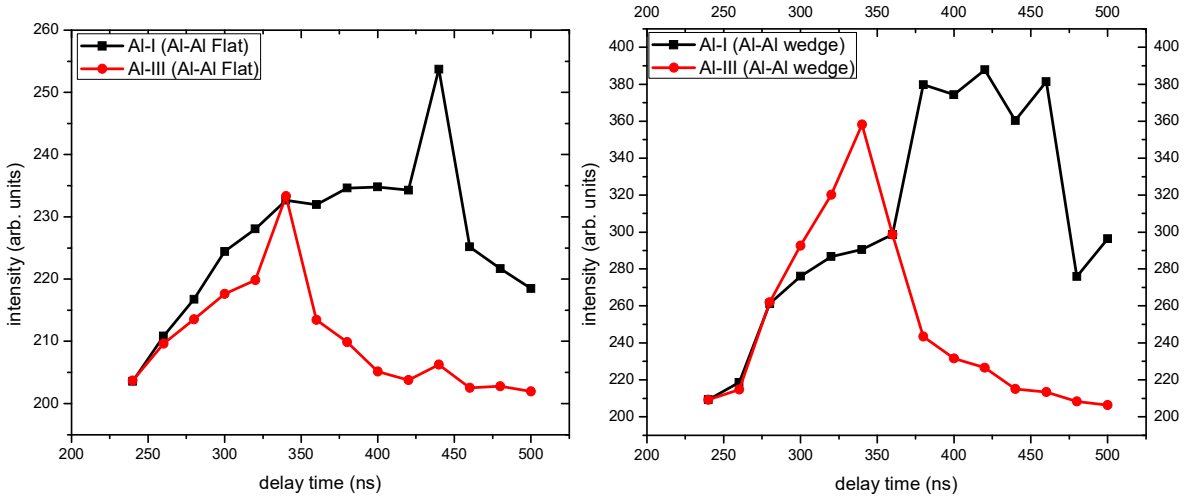

Figure 7.14: Time evolution of Al-I and Al-III ion stages at the collision front Al-Al colliding plasmas; (left) flat target (right) wedge target.

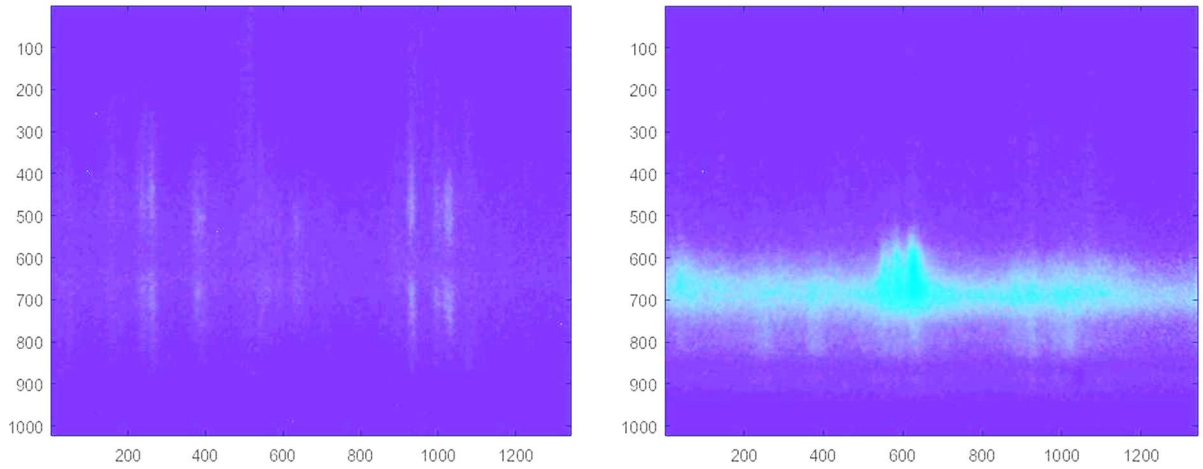

7.5.2 Comparison of Time-Resolved Colliding Plasma Spectroscopy of Al-Si Flat and 90° Wedge target

In this section, the detailed analysis of the time-resolved spectroscopic data of the Al-Si colliding plasmas at the collision front in case of flat and wedge target is discussed. Different types of plotting the data are presented in order to observe and present the time evolution of different ion stages present in the stagnation layer of Al-Si targets in different configurations. The raw spectral CCD images of the stagnation layer of Al-Si flat and wedge targets for the same delay time are presented in Figure 7.15 which clearly indicates the emission is stronger and brighter in case of the wedge-shaped target as compared to the flat target.

Figure 7.15: ICCD images of the Al-Si stagnation layer for delay time 300 ns at integration time 100 ns; (left) flat target (right) 90° wedge target.

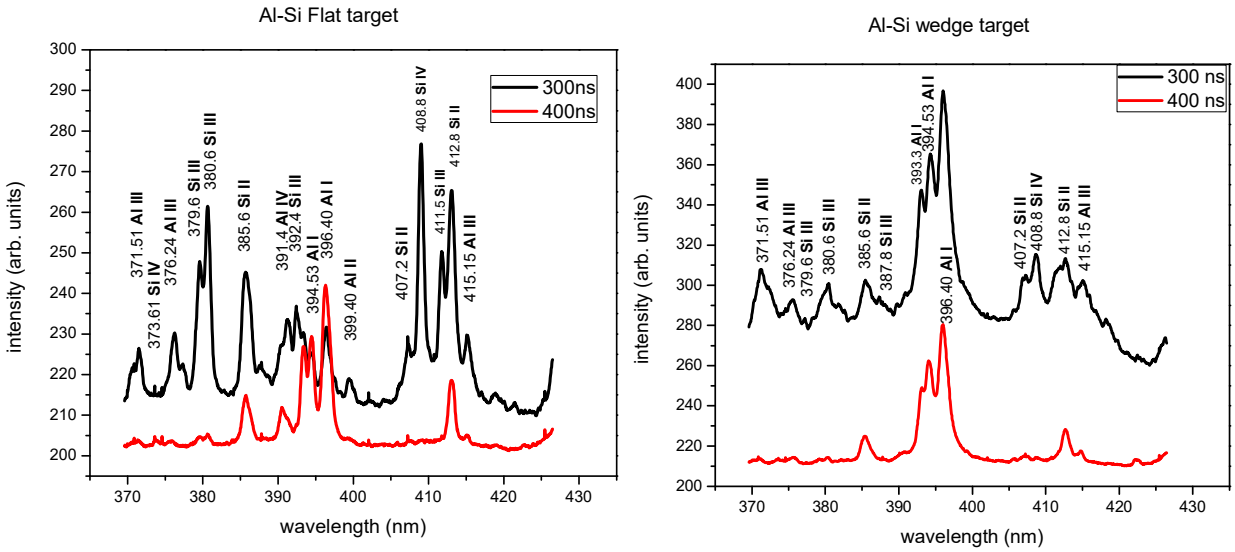

Figure 7.16:Comparison of UV- Visible time-resolved spectrum of the Al-Si stagnation layer for delay time 300 ns and 400 ns; (left) flat target (right) 90° wedge target.

Figure 7.16 shows the spectral data of Al-Si colliding plasma stagnation layer at delay time 340 ns and 440 ns for fixed integration time along with the spectral assignments from the NIST database.

Over the region of interest here (370 - 426 nm), emission is generally dominated by aluminum ion and neutral lines. The neutral silicon line at 390 nm is difficult to separate from an Al II line at a similar wavelength. Once again we can see that the wedge shaped targets produce much brighter spectra. It is interesting that for the heterogeneous targets (Al + Si) the Al IV line at 391 is much weaker in the wedge shaped targets compared to the flat targets. This was not the case for the homogenous targets (Al-Al). In fact, the wedge shaped target generally produces a spectrum where the emission from higher ion stages are significantly weaker than their counterpart's in the flats targets. Figure 7.17 and Figure 7.18 shows how the different ions and neutrals evolve over time. As before the higher ion stages appear at earlier times and then fade out as the emission form lower ion stages increases. Figure 7.19 and Figure 7.20 attempts to show this by tracking the emission over time for selected lines in each ion stage. As we can see the Si IV line emission peaks first, then Si III and finally the Si II emission peaks and persists for longer than the higher ion stages.

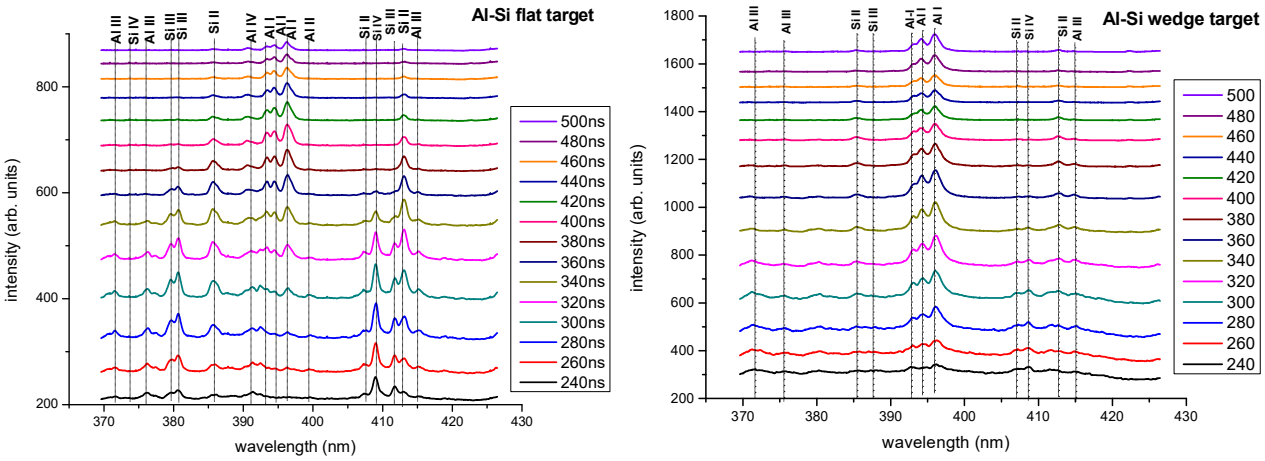

Figure 7.17: Layer plot: UV-Visible Time-resolved spectrum of the Al-Si stagnation layer for delay time 200- 500 ns at integration time 100 ns; (left) flat target (right) 90° wedge target.

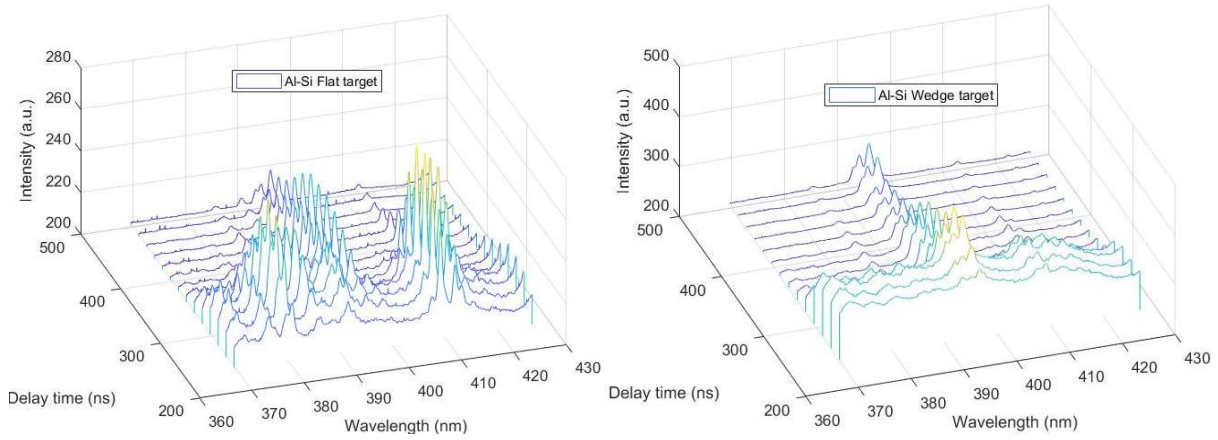

Figure 7.18: Waterfall plot: Time-resolved spectrum of the Al-Si stagnation layer for delay time 200- 500 ns and integration time 100 ns; (left) flat target (right) 90° wedge target.

The time evolution of Al-I, Al-III ion stages are in case of flat target are presented in Figure 7.19. which indicates Al-III emission is stronger in earlier times and then fadeout however Al-I have much longer lifetime. There is a noticeable difference to the profile compared to the heterogeneous targets Figure 7.14, where now the peaks occur earlier but overall the emission is more evenly distributed in the case of the neutral lines. This may indicate the heterogeneous plasmas are more uniform then the homogeneous one.

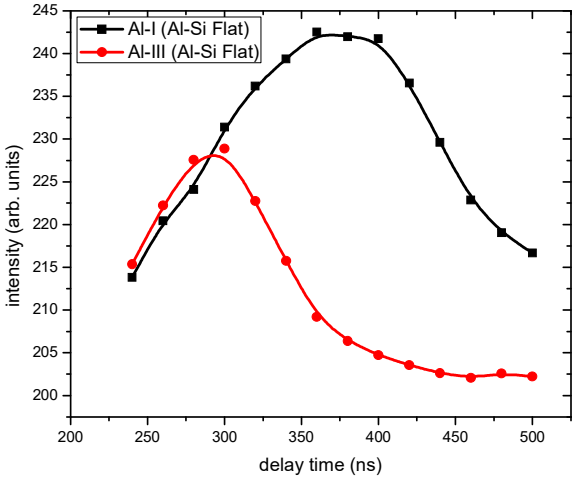

Figure 7.19: Time evolution of Al-I and Al-III ion stages at the collision front of Al-Si colliding plasmas in case of flat target.

The silicon emission over time is tracked in Figure 7.20. We can see how each ion separates out in time with the lower ion stages persisting for longer. The peaks in silicon occur at earlier time scales compared to aluminum in the heterogeneous targets Figure 7.19 perhaps reflecting the fact that these are slightly higher ion stages than in the case for aluminum in both the homogenous and heterogeneous targets. The persistence of the silicon lines is not as noticeable in the wedge shaped target as it was for aluminum.

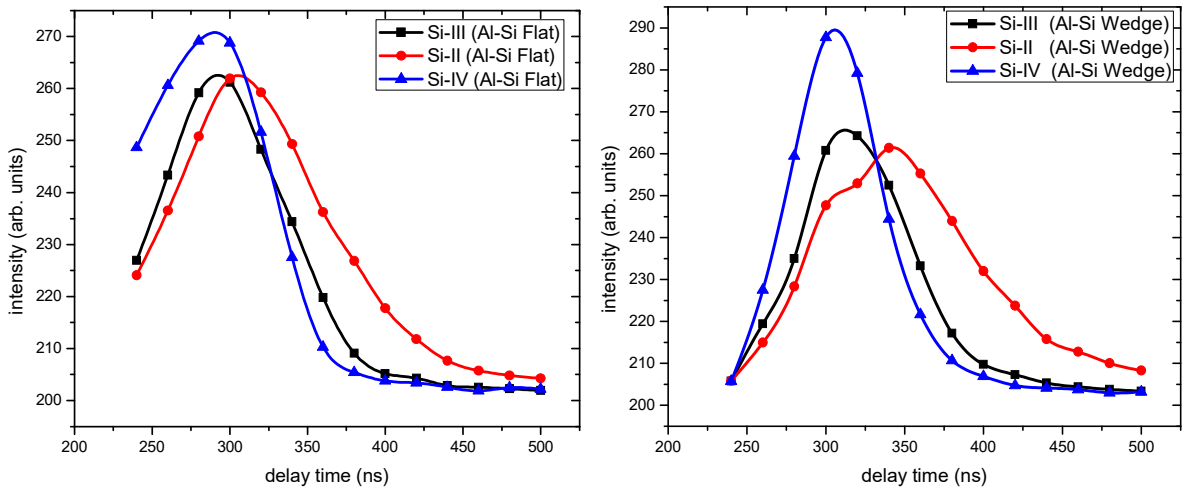

Figure 7.20: Time evolution of Si-II, Si-III and Si-IV ion stage at the collision front of Al-Si colliding plasma; (left) flat target (right) wedge target.

7.5.3 Electron Number Density

In order to estimate the electron number density of the colliding plasma stagnation layer, the spectral data were fitted using Voigt functions (convolution of Lorentzian profile and Gaussian profile) in order to retrieve the line width of some specific lines. Which is required in order to estimate the electron number density. The full width at half maximum (FWHM) of the spectral line is related to the electron density through the following relation with an assumption that the ion field contribution to the broadening is negligible.

$$\Delta\lambda_{1/2} = 2w\left(\frac{n_e}{10^{16}}\right) \tag{7.5}$$

$$n_e = \frac{\Delta\lambda_{1/2} \times 10^{16}}{2w} \tag{7.6}$$

Where (w) is the stark broadening parameter and (n_e) is the electron density and $\Delta\lambda_{1/2}$ is the FWHM of the spectral line profile. A Matlab code based on the Voigt function with input as the spectral image of the ICCD camera was used. The emission lines of Al and Si with longer lifetimes were used to fit with Voigt function, and the FWHM of the selected lines were retrieved for the time delays for which the spectral line has appeared. These FWHM values were used to estimate the electron density of the plasma. As for Al, the strong emission line which remains for longer time was Al-I and for Si, the emission line with longer time was Si-II so these lines were used for fitting and FWHM was calculated for these lines.

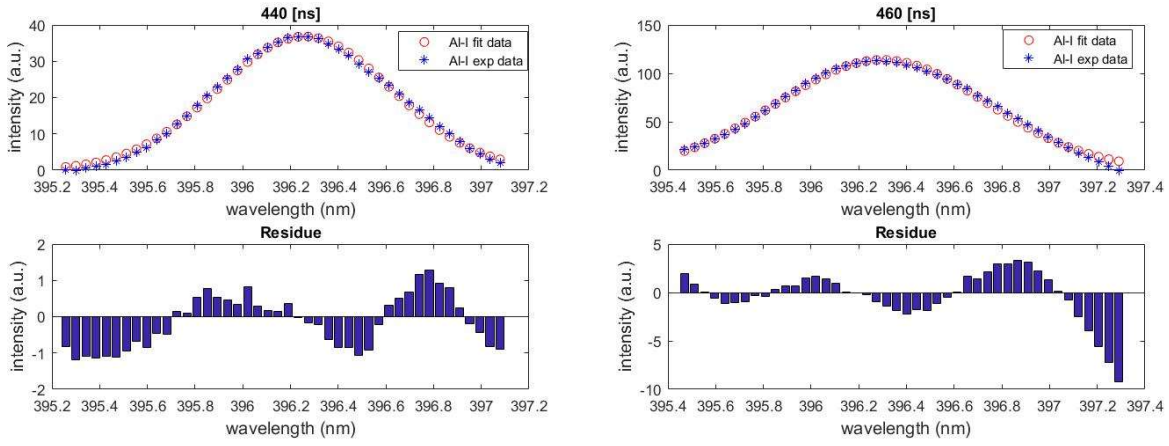

Figure 7.21: Voigt fitting of the Al-I emission line; (left) Al-Al flat target (right) Al-Al wedge target.

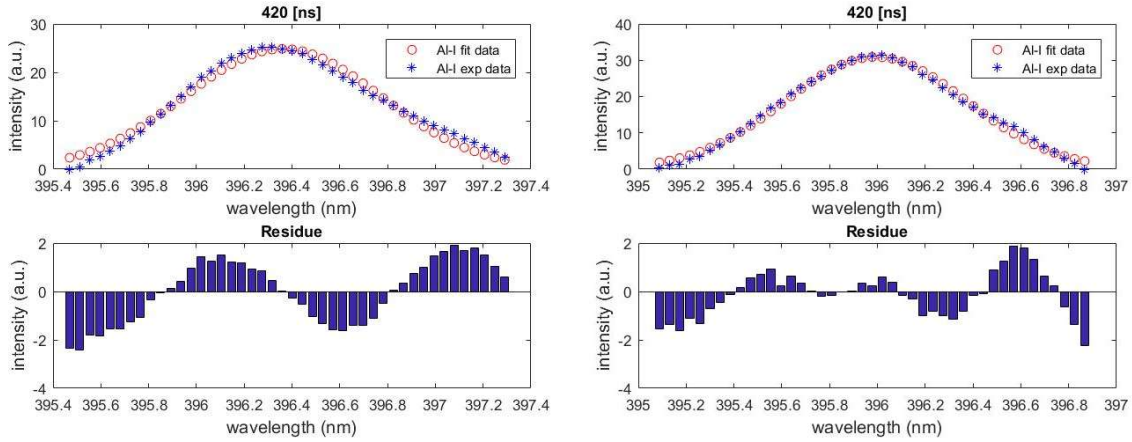

Figure 7.22: Voigt fitting of the Al-I emission line; (left) Al-Si flat target (right)Al-Si wedge target.

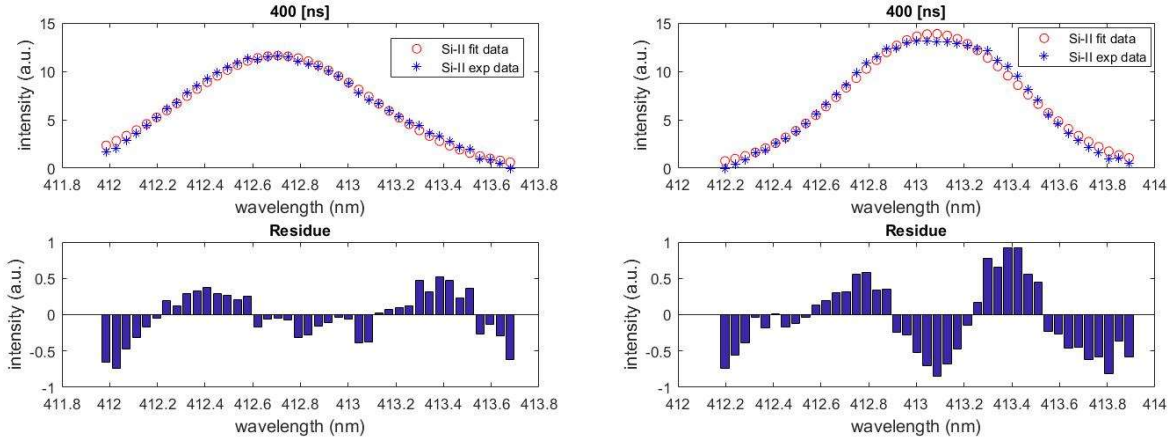

Figure 7.23: Voigt fitting of the Si-II emission line: (left) Al-Si flat target (right) Al-Si wedge target.

The Voigt fitting of the selected spectral lines was performed for delay time 240- 500 ns. Figure 7.21 shows the Voigt fitting of Al-I spectral line for Al-Al flat and wedge target along with the residue for specific delay time, Figure 7.22 shows the fitting result of Al-I spectral line for Al-Si flat and wedge target and Figure 7.23 shows the Si-II spectral line fitting for Al-Si flat and wedge target along with residue in order to show the fitting quality.

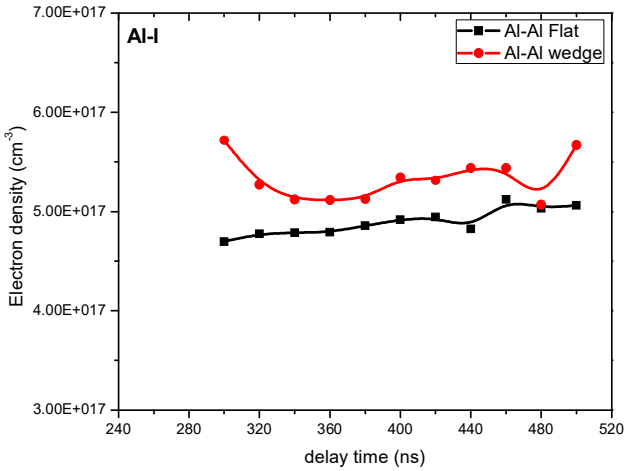

Figure 7.24: Electron density comparison at the collision front of Al-Al flat and wedge target calculated using Al-I emission line.

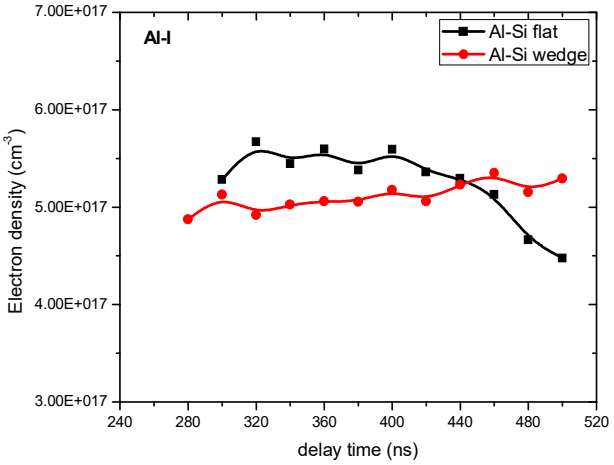

Figure 7.25: Electron density comparison at the collision front of Al-Si flat and wedge target calculated using Al-I emission line.

From the Voigt fitting, FWHM of the spectral lines were retrieved and the electron density calculated using eq. 7.5 and 7.6. Figure 7.24 shows the comparative results of time evolution of the density of electron in case of Al-Al flat and wedge target calculated using the FWHM of Al-I emission line. The stark broadening parameter (w) was used from [143] with value w= 0.84 A° for Al-I. As can be seen from Figure 7.24, the density of electron in case of wedge target is higher than the flat target. Figure 7.25 shows the comparison of time evolution of the electron density calculated using the FWHM of Al-I emission line in case of Al-Si flat and wedge target configurations. It is observed that in case of heterogeneous target (Al+ Si), the electron number

density calculated by FWHM of Al-I ion stage is higher in case of flat target as compared to wedge target. However, in case of homogeneous target (Al+ Al) it was opposite.

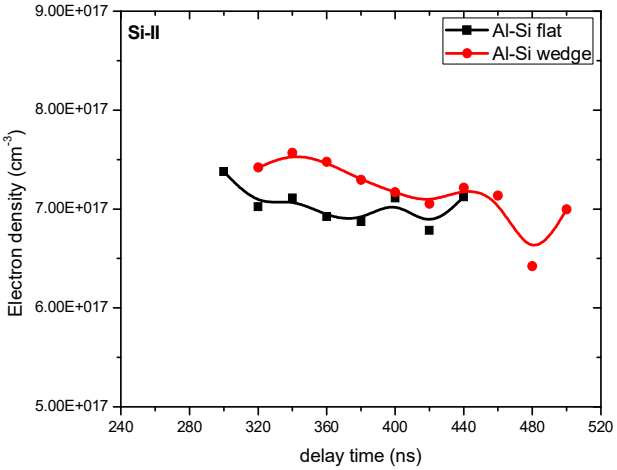

Figure 7.26: Electron density comparison at the collision front of Al-Si flat and wedge target calculated using Si-II emission line

Figure 7.26 shows the time evolution of electron density calculated using the Si-II emission line in case of Al-Si flat and wedge target. The stark broadening parameter (w) for Si-II emission line was taken from [151] with value w= 0.565 A°. From the comparison of the flat and wedge target, it can be observed that the electron density is higher in case of wedge target configuration as compared to flat target. However, the overall trend of electron density is decreasing with time.

7.6 Conclusions

Time evolution and dynamics of the Al-Al, Al-Si colliding plasma at their collision front was studied by employing time-resolved plasma spectroscopic technique. A comparative study has been done w.r.t. the two geometrical configurations (i.e., flat and 90° wedge) of the target. Two types of targets were used in this study (Al- Al, Al-Si) in order to study the effect of homogeneous and heterogeneous targets on the dynamics of the stagnation layer. The plasma dynamics was studied in terms of time evolution of different ion stages and electron number density. It was observed that in case of wedge target configuration the stagnation layer results in brighter spectra and higher ionization states were more prominent in earlier times as compared to the flat target configurations; this behavior was evidenced in all the data. Perhaps this is because of the fact that in case of wedge target, the two seed plasmas collide with a larger component of their forward expansion velocity. It was observed that in case of Al-Si target the time evolution of ion stages of

Aluminium were more uniform then in case of Al-Al targets. Moreover, the stagnation layer of Al-Si wedge target results in brighter spectra dominantly consist of Al-I ion stages however in case of Al-Si flat target the stagnation layer spectra was evenly distributed among the Si and Al ion stages. The electron number density was calculated using emission lines with longer lifetimes, i.e. Si-II and Al-I. Overall wedge target configuration results in higher electron density as compared to flat target configurations.

Chapter 8. Overall Conclusions and Future Directions

The work presented in this thesis covers two technologically important aspects related to the advancement and improvement in the short wavelength (EUV- VUV) technological domains.

The first and main aspect studied in this thesis is about the detailed optical investigations of the 2D materials (mono & few-layer graphene) in the VUV spectral region by employing different diagnostic techniques (VUV polarimetry and reflectometry) taking into account the light polarization. The aim was to explore the potential of such materials for the development and improvement of EUV- VUV optics.

The second aspect discussed is about the study of colliding laser produces plasmas with the purpose of analyzing the common region at the collision front of two plasmas called 'stagnation layer' for different target geometries, by exploiting time resolved spectroscopic technique. The aim was to comprehend and explore potential techniques for the development and improvement of laboratory-based light sources.

8.1 Conclusions

Based on the findings of the widespread research activities carried out during the three-year period, the following conclusions can be drawn.

- In order to explore the reliable optical performance of graphene-like samples having atomic thickness, it is essential to know/ measure the detailed optical properties of substrate material in the selected spectral region.
- A novel approach based on the combined use of ellipsometry and reflectometry to find out the reliable values of optical constants of SiO_2 at hydrogen Lyman alpha spectral line was demonstrated and it was concluded in this study that the least square fitting of the ellipsometric parameters results in reliable optical constants, however in case of reflectance fitting results shows greater uncertainty.
- Graphene on top of the dielectric substrate (SiO_2/Si) affects significantly, its polarimetric properties and optical throughput around Brewster angle, which is the evidence of strong

interaction of graphene with the E.M radiation at hydrogen Lyman alpha despite having atomic thickness.

- The reflectance data suggests that the graphene behaves as an optically anisotropic material at hydrogen Lyman alpha, which is the first experimental evidence as per our knowledge. Optical anisotropy was observed in the case of both samples (i.e., 1LG and 3LG); however, relatively higher anisotropy was observed in the case of the 3LG.
- The optical constants measurement of the graphene was a quite challenging task because of having an atomic thickness and optical anisotropic behavior. With the approach adopted in this thesis the reliable 'effective optical constants' corresponding to the 'effective thickness' of both samples of graphene 1L and 3L determined and optical constants reflect the optical anisotropy. To best of our knowledge, the optical constants values of graphene at hydrogen Lyman alpha are entirely new and never been reported.
- Another very interesting effect induced by graphene is the shift of the pseudo-Brewster angle with respect to that of the bare substrate. Downshift of the Brewster angle was observed at hydrogen Lyman alpha in contrast to the upshift in the literature, however at different spectral region. Larger downshift was observed in case of 3LG sample as compared to 1LG.
- Based on the optical findings, it can be concluded that 1LG and 3LG samples are independently different materials having different interaction with electromagnetic.
- These remarkable findings of the optical properties of graphene in VUV are of considerable importance and implications for the development and improvements for the EUV-VUV technological domains.
- Comparison of the time-resolved spectroscopic studies of Al-Al and Al-Si colliding plasmas at their collision front in case of flat and wedge targets suggests that in case of wedge target configuration the stagnation layer results in brighter spectra having higher ionization states more intense and appeared earlier in time as compared to the flat target configurations.
- Relatively larger electron number density is also observed in the case of wedge targets.
- Characteristics and formation of the stagnation layer at the collision front of two colliding plasmas depend on the geometrical shape of the targets as well as the materials.

8.2 Future Aspects and Directions

The remarkable results achieved in this thesis research work regarding the optical properties of graphene are of great interest shows the great potential regarding the utilization of graphene in the optics development and improvements for short-wavelength technological domains. Some of the potential areas where graphene can be highly beneficial are; astronomical optics (as capping layer for VUV reflective optics for improvement of optical throughput and protection against unavoidable oxidation/ corrosion), EUV optical components (e.g. Multilayer optics, EUV pellicles etc.), VUV polarimetric optics. The strong dependence of optical response of graphene on the light polarization at hydrogen Lyman alpha could be highly beneficial in a sense that having greater control and manipulation of incoming light.

The results of the research work presented are of great importance and motivates the needs of further studies related to the optical performance of 2D materials in the short wavelength technological domain.

- There is need to further explore the potential of graphene in whole spectral region EUV-VUV spectral region. As a future direction, further studies graphene in the other technologically important spectral lines of interests covering astronomical to EUV lithography technological areas will be explored. We already have done some preliminary measurements for some of these spectral lines of interest.
- Secondly, the optical response of graphene on different substrates of technological importance can be highly beneficial.
- Optical performance of other potential 2D materials e.g. 2D MoS_2 could be of great interest for short-wavelength optics advancements
- As a future work regarding the CLPP, generation of the EUV light source by reheating of the stagnation laser using CO_2 laser can be done.
- Dynamics of stagnation layer formed by different target geometries and different spectral areas of interest can be done.
- Use of femtosecond or picosecond laser to for similar kind of experiments can be of interesting study.

Bibliography

[1] D. Attwood, *Soft X-rays and Extreme Ultraviolet Radiation*. Cambridge: Cambridge University Press, 1999.

[2] L. V. R. De Marcos *et al.*, "Optimization of MgF 2 -deposition temperature for far UV Al mirrors," *Opt. Express*, vol. 26, no. 7, p. 9363, Apr. 2018.

[3] W. R. Hunter, J. F. Osantowski, and G. Hass, "Reflectance of Aluminum Overcoated with MgF_2 and LiF in the Wavelength Region from 1600 Å to 300 Å at Various Angles of Incidence," *Appl. Opt.*, vol. 10, no. 3, p. 540, 1971.

[4] Y. Zhang, Y. W. Tan, H. L. Stormer, and P. Kim, "Experimental observation of the quantum Hall effect and Berry's phase in graphene," *Nature*, vol. 438, no. 7065, pp. 201–204, 2005.

[5] W. A. de Heer *et al.*, "Epitaxial graphene," *Solid State Commun.*, vol. 143, no. 1–2, pp. 92–100, Jul. 2007.

[6] S. Chen *et al.*, "Oxidation Resistance of Graphene-Coated Cu and Cu/Ni Alloy," *ACS Nano*, vol. 5, no. 2, pp. 1321–1327, Feb. 2011.

[7] N. T. Kirkland, T. Schiller, N. Medhekar, and N. Birbilis, "Exploring graphene as a corrosion protection barrier," *Corros. Sci.*, vol. 56, pp. 1–4, Mar. 2012.

[8] J. S. Bunch *et al.*, "Impermeable atomic membranes from graphene sheets," *Nano Lett.*, vol. 8, no. 8, pp. 2458–2462, 2008.

[9] V. Mišković-Stanković, I. Jevremović, I. Jung, and K. Rhee, "Electrochemical study of corrosion behavior of graphene coatings on copper and aluminum in a chloride solution," *Carbon N. Y.*, vol. 75, pp. 335–344, 2014.

[10] P. Zuppella, F. Gerlin, and M. G. Pelizzo, "Angular reflectance of graphene/SiO2/Si in UV spectral range : A study for potential applications," *Opt. Mater. (Amst).*, vol. 67, pp. 132–138, 2017.

[11] J. W. Weber, V. E. Calado, and M. C. M. Van De Sanden, "Optical constants of graphene

measured by spectroscopic ellipsometry," *Appl. Phys. Lett.*, vol. 97, no. 9, p. 091904, Aug. 2010.

[12] A. Gao *et al.*, "Extreme ultraviolet induced defects on few-layer graphene," *J. Appl. Phys.*, vol. 114, no. 4, pp. 1–6, 2013.

[13] F. Gerlin *et al.*, "Stability and extreme ultraviolet photo-reduction of graphene during C-K edge NEXAFS characterization," *Surf. Coat. Technol.*, vol. 296, pp. 211–215, 2016.

[14] V. Yevgenyevich and E. Roelof, "(19) United States (12)," vol. 1, no. 19, 2014.

[15] Y. C. 299-0265 (JP) ONO, K. K. Y. 740-0061 (JP) KOHMURA, and (74), "PELLICLE AND EUV EXPOSURE DEVICE COMPRISING SAME (57)," 2016.

[16] R. B. Hoover *et al.*, "Solar observations with the multispectral solar telescope array," in *Multilayer and Grazing Incidence X-Ray/EUV Optics*, 1992, vol. 1546, p. 175.

[17] B. N. Handy *et al.*, "UV observations with the transition region and coronal explorer," *Sol. Phys.*, vol. 183, no. 1, pp. 29–43, 1998.

[18] W. Curdt, H. Tian, L. Teriaca, U. Schühle, and P. Lemaire, "The Ly-α profile and center-to-limb variation of the quiet Sun," *Astron. Astrophys.*, vol. 492, no. 1, pp. 1–5, 2008.

[19] J. A. S. and D. L. Ederer, *Vacuum Ultraviolet Spectroscopy I*. Academic Press, 1998.

[20] M. A. Barstow, S. L. Casewell, J. B. Holberg, and M. P. Kowalski, "The status and future of EUV astronomy," *Adv. Sp. Res.*, vol. 53, no. 6, pp. 1003–1013, 2014.

[21] J. Fujimoto, T. Hori, T. Yanagida, and H. Mizoguchi, "Development of laser-produced tin plasma-based EUV light source technology for HVM EUV lithography," *Phys. Res. Int.*, vol. 2012, no. 1, pp. 1–11, 2012.

[22] H. Komori *et al.*, "Ion damage analysis on EUV collector mirrors," in *Emerging Lithographic Technologies VIII*, 2004, vol. 5374, p. 839.

[23] A. I. Lvovsky, "Fresnel Equations," in *Encyclopedia of Optical Engineering*, no. August, 2013, pp. 37–41.

[24] Jean M . Bennett, "CHAPTER 5 Polarization," in *Handbook of Optics, Volume 1: Fundamentals, Techniques, and Design*, 1994, pp. 5.1-5.30.

[25] M. Bass and O. S. of America, *Handbook of Optics: Fundamentals, techniques, and design*, no. v. 1. McGraw-Hill, 1994.

[26] E. PALIK, "Handbook of Optical Constants of Solids," in *Handbook of Optical Constants of Solids*, San Diego: Academic Press, Inc., 1997.

[27] W. R. Hunter, "Measurement of optical properties of materials in the vacuum ultraviolet spectral region," *Appl. Opt.*, vol. 21, no. 12, p. 2103, 1982.

[28] J. I. Larruquert, J. A. Me, and J. A. Azna, "Far-ultraviolet reflectance measurements and optical constants of unoxidized aluminum films," *Appl. Opt.*, vol. 34, no. 22, pp. 4892–4899, 1995.

[29] R. Soufli and E. M. Gullikson, "Reflectance measurements on clean surfaces for the determination of optical constants of silicon in the extreme ultraviolet–soft-x-ray region," *Appl. Opt.*, vol. 36, no. 22, p. 5499, 1997.

[30] G. Monaco *et al.*, "Optical constants in the EUV soft x-ray (5÷152 nm) spectral range of B 4 C thin films deposited by different deposition techniques," in *Advances in X-Ray/EUV Optics, Components, and Applications*, 2006, vol. 6317, no. August, p. 631712.

[31] W. R. Hunter, *The Preparation and Use of Unbacked Metal Films as Filters in the Extreme Ultraviolet*, vol. 7. ACADEMIC PRESS, INC., 1973.

[32] Y. Uspenskii *et al.*, "Extreme UV optical constants of rare-earth metals free from effects of air contamination," in *Soft X-Ray Lasers and Applications VI*, 2005, vol. 5919, p. 59190S.

[33] H. J. Hagemann, W. Gudat, and C. Kunz, "OPTICAL CONSTANTS FROM THE FAR INFRARED TO THE X-RAY REGION: Mg, Al, Cu, Ag, Au, Bi, C, and Al2O3.," *J Opt Soc Am*, vol. 65, no. 6, pp. 742–744, 1975.

[34] H. G. Tompkins, E. A. Irene, C. Hill, and N. Carolina, *Handbook of Ellipsometry*. Eaton Avenue, Norwich, NY: Springer Berlin Heidelberg, 2005.

[35] T. Tsuru and M. Yamamoto, "Precise determination of layer structure with EUV ellipsometry data obtained by multilayer polarizing elements," in *Physica Status Solidi (C) Current Topics in Solid State Physics*, 2008, vol. 5, no. 5, pp. 1129–1132.

[36] A. E. H. Gaballah *et al.*, “A table top polarimetric facility for the EUV spectral range: implementations and characterization,” in *Proceedings of SPIE - The International Society for Optical Engineering*, 2017, vol. 10235, p. 102350X.

[37] A. E. H. Gaballah *et al.*, “EUV polarimetry for thin film and surface characterization and EUV phase retarder reflector development,” *Rev. Sci. Instrum.*, vol. 89, no. 1, p. 015108, 2018.

[38] Fujiwara, *Spectroscopic Ellipsometry: Principles and Applications*. 2007.

[39] A. Weidlich and A. Wilkie, “Realistic rendering of birefringency in uniaxial crystals,” *ACM Trans. Graph.*, vol. 27, no. 1, pp. 111–129, 2008.

[40] C. C. Davis, “The optics of anisotropic media,” in *Lasers and Electro-optics*, Cambridge: Cambridge University Press, 2014, pp. 539–579.

[41] F. V. Ignaovich and V. K. Ignatovich, “Optics of anisotropic media,” in *Uspekhi Fizicheskih Nauk*, vol. 182, no. 7, 2012, p. 759.

[42] P. R. Wallace, “The band theory of graphite,” *Phys. Rev.*, vol. 71, no. 9, pp. 622–634, 1947.

[43] Eduardo Fradkin, “Critical behavior of disordered degenerate semiconductors. II. Spectrum and transport properties in mean-field theory,” *Phys. Rev. B*, vol. 33, no. 5, pp. 3263–3268, 1986.

[44] N. D. Mermin, “Crystalline Order in Two Dimensions,” *Phys. Rev.*, vol. 176, no. 1, pp. 250–254, Dec. 1968.

[45] T. A. Land, T. Michely, R. J. Behm, J. C. Hemminger, and G. Comsa, “STM investigation of single layer graphite structures produced on Pt(111) by hydrocarbon decomposition,” *Surf. Sci.*, vol. 264, no. 3, pp. 261–270, 1992.

[46] Y. Ohashi, T. Koizumi, T. Yoshikawa, T. Hironaka, and K. Shiiki, “Size Effect inthe In-plane Electrical Resistivity of Very Thin Graphite Crystals,” *TANSO*, vol. 1997, no. 180, pp. 235–238, 1997.

[47] I. V. G. and A. A. F. K. S. Novoselov, A. K. Geim, S. V. Morozov, D. Jiang, Y. Zhang, S. V. Dubonos, “Electric Field Effect in Atomically Thin Carbon Films,” *Science (80-.).*,

vol. 306, no. 5696, pp. 666–669, Oct. 2004.

[48] B. Garg, T. Bisht, and Y.-C. Ling, “Graphene-Based Nanomaterials as Heterogeneous Acid Catalysts: A Comprehensive Perspective,” *Molecules*, vol. 19, no. 9, pp. 14582–14614, Sep. 2014.

[49] A. K. Geim and K. S. Novoselov, “The rise of graphene,” *Nat. Mater.*, vol. 6, no. 3, pp. 183–191, Mar. 2007.

[50] Y. H. Wu, T. Yu, and Z. X. Shen, “Two-dimensional carbon nanostructures: Fundamental properties, synthesis, characterization, and potential applications,” *J. Appl. Phys.*, vol. 108, no. 7, pp. 1–38, 2010.

[51] A. H. C. Neto and K. Novoselov, “New directions in science and technology: two-dimensional crystals,” *Reports Prog. Phys.*, vol. 74, no. 8, p. 082501, Aug. 2011.

[52] W. Choi, I. Lahiri, R. Seelaboyina, and Y. S. Kang, “Synthesis of Graphene and Its Applications: A Review,” *Crit. Rev. Solid State Mater. Sci.*, vol. 35, no. 1, pp. 52–71, Feb. 2010.

[53] P. Avouris and C. Dimitrakopoulos, “Graphene: Synthesis and applications,” *Mater. Today*, vol. 15, no. 3, pp. 86–97, 2012.

[54] K. E. Whitener and P. E. Sheehan, “Graphene synthesis,” *Diam. Relat. Mater.*, vol. 46, pp. 25–34, Jun. 2014.

[55] V. Singh, D. Joung, L. Zhai, S. Das, S. I. Khondaker, and S. Seal, “Graphene based materials: Past, present and future,” *Prog. Mater. Sci.*, vol. 56, no. 8, pp. 1178–1271, Oct. 2011.

[56] J. S. Bunch *et al.*, “Impermeable Atomic Membranes from Graphene Sheets,” *Nano Lett.*, vol. 8, no. 8, pp. 2458–2462, Aug. 2008.

[57] Y. Q. Liang, L. L. Yu, Z. D. Cui, S. L. Zhu, Z. Y. Li, and X. J. Yang, “Large-Scale Synthetic Graphene on Cu as Anti-Corrosion Coating by Chemical Vapor Deposition Approach,” *Sci. Adv. Mater.*, vol. 6, no. 3, pp. 545–549, Mar. 2014.

[58] A. S. Sai Pavan and S. R. Ramanan, “A study on corrosion resistant graphene films on low alloy steel,” *Appl. Nanosci.*, vol. 6, no. 8, pp. 1175–1181, 2016.

[59] M. Schriver, W. Regan, W. J. Gannett, A. M. Zaniewski, M. F. Crommie, and A. Zettl, "Graphene as a Long-Term Metal Oxidation Barrier: Worse Than Nothing," *ACS Nano*, vol. 7, no. 7, pp. 5763–5768, Jul. 2013.

[60] J. Hu, Y. Ji, and Y. Shi, "A Review on the use of Graphene as a Protective Coating against Corrosion," *Ann. Mater. Sci. Eng.*, vol. 1, no. 3, pp. 1–16, 2014.

[61] C. Lee, X. Wei, J. W. Kysar, and J. Hone, "Measurement of the Elastic Properties and Intrinsic Strength of Monolayer Graphene," *Science*, vol. 321, no. July, pp. 385–388, 2008.

[62] K. S. Kim *et al.*, "Large-scale pattern growth of graphene films for stretchable transparent electrodes.," *Nature*, vol. 457, no. 7230, pp. 706–10, 2009.

[63] W. Zhang *et al.*, "Ultrahigh-Gain Photodetectors Based on Atomically Thin Graphene-MoS2 Heterostructures," *Sci. Rep.*, vol. 4, no. 1, p. 3826, May 2015.

[64] R. R. Nair *et al.*, "Fine Structure Constant Defines Visual Transparency of Graphene," *Science (80-.).*, vol. 320, no. 5881, pp. 1308–1308, 2008.

[65] C. H. Lui, K. F. Mak, J. Shan, and T. F. Heinz, "Ultrafast Photoluminescence from Graphene," *Phys. Rev. Lett.*, vol. 105, no. 12, p. 127404, Sep. 2010.

[66] C. Casiraghi *et al.*, "Rayleigh Imaging of Graphene and Graphene Layers," *Nano Lett.*, vol. 7, no. 9, pp. 2711–2717, Sep. 2007.

[67] P. Blake *et al.*, "Making graphene visible," *Appl. Phys. Lett.*, vol. 91, no. 6, p. 063124, Aug. 2007.

[68] X. Wang, Y. P. Chen, and D. D. Nolte, "Strong anomalous optical dispersion of graphene: complex refractive index measured by Picometrology," *Opt. Express*, vol. 16, no. 26, p. 22105, 2008.

[69] M. Bruna and S. Borini, "Optical constants of graphene layers in the visible range," *Appl. Phys. Lett.*, vol. 94, no. 3, pp. 2007–2010, 2009.

[70] Z. H. Ni *et al.*, "Graphene Thickness Determination Using Reflection and Contrast Spectroscopy," *Nano Lett.*, vol. 7, no. 9, pp. 2758–2763, Sep. 2007.

[71] A. Gray, M. Balooch, S. Allegret, S. De Gendt, and W. E. Wang, "Optical detection and

characterization of graphene by broadband spectrophotometry," *J. Appl. Phys.*, vol. 104, no. 5, 2008.

[72] J. W. Weber, V. E. Calado, and M. C. M. Van De Sanden, "Optical constants of graphene measured by spectroscopic ellipsometry," *Appl. Phys. Lett.*, vol. 97, no. 9, pp. 1–4, 2010.

[73] M. Z. and K. F. Wei-E Wang, M. Balooch, C. Claypool, "Combined reflectometry-ellipsometry technique to measure graphite down to monolayer thickness," *Solid State Technol.*, vol. Vol. 52, no. Issue 6, 2009.

[74] V. G. Kravets *et al.*, "Spectroscopic ellipsometry of graphene and an exciton-shifted van Hove peak in absorption," *Phys. Rev. B - Condens. Matter Mater. Phys.*, vol. 81, no. 15, pp. 1–6, 2010.

[75] A. Matković *et al.*, "Spectroscopic imaging ellipsometry and Fano resonance modeling of graphene," *J. Appl. Phys.*, vol. 112, no. 12, p. 123523, Dec. 2012.

[76] M. Klintenberg, S. Lebègue, C. Ortiz, B. Sanyal, J. Fransson, and O. Eriksson, "Evolving properties of two-dimensional materials: from graphene to graphite," *J. Phys. Condens. Matter*, vol. 21, no. 33, p. 335502, Aug. 2009.

[77] W. T. Welford, "VI Aberration Theory of Gratings and Grating Mountings," in *Progress in Optics*, vol. 4, no. C, 1965, pp. 241–280.

[78] "CEM detectors." [Online]. Available: http://www.sjuts.com.

[79] "hamamatsu." [Online]. Available: http://www.hamamatsu.com.

[80] "PI motion and positioning." [Online]. Available: http://www.physikinstrumente.com.

[81] "BEAR beamline description." [Online]. Available: https://www.elettra.trieste.it/it/lightsources/elettra/elettra-beamlines/bear/beamline-description.html.

[82] S. Nannarone *et al.*, "The BEAR beamline at elettra," in *AIP Conference Proceedings*, 2004, vol. 705, no. June 2014, pp. 450–453.

[83] "Elettra sincrotrone Trieste." [Online]. Available: http://www.elettra.trieste.it/lightsources/elettra/elettra-beamlines/bear/beamline-description.html?showall=.

[84] “Atomic Force Microscopy.” [Online]. Available: http://www.nanoscience.com.

[85] N. Ahlawat, “Raman Spetroscopy: A Review,” *Int. J. Comput. Sci. Mob. Comput.*, vol. 3, no. 11, pp. 680–685, 2014.

[86] T. Itoh, A. Sujith, and Y. Ozaki, “Surface-Enhanced Raman Scattering Spectroscopy: Electromagnetic Mechanism and Biomedical Applications,” in *Frontiers of Molecular Spectroscopy*, 2009, pp. 289–319.

[87] D. E. Bugay and H. G. Brittain, “Raman spectroscopy,” in *Spectroscopy of Pharmaceutical Solids*, no. 1, 2006, pp. 271–312.

[88] “https://chromosomeface.wordpress.com/2017/03/08/raman-effect-biology/.” [Online]. Available: https://chromosomeface.wordpress.com/2017/03/08/raman-effect-biology/.

[89] A. C. Ferrari, “Raman spectroscopy of graphene and graphite: Disorder, electron–phonon coupling, doping and nonadiabatic effects,” *Solid State Commun.*, vol. 143, no. 1–2, pp. 47–57, Jul. 2007.

[90] Y. A. Kim *et al.*, “Raman spectroscopy of boron-doped single-layer graphene,” *ACS Nano*, vol. 6, no. 7, pp. 6293–6300, 2012.

[91] H. Park, J. A. Rowehl, K. K. Kim, V. Bulovic, and J. Kong, “Doped graphene electrodes for organic solar cells,” *Nanotechnology*, vol. 21, no. 50, p. 505204, Dec. 2010.

[92] M. S. Dresselhaus, A. Jorio, and R. Saito, “Characterizing Graphene, Graphite, and Carbon Nanotubes by Raman Spectroscopy,” *Annu. Rev. Condens. Matter Phys.*, vol. 1, no. 1, pp. 89–108, 2010.

[93] P. R. Kidambi *et al.*, “The parameter space of graphene chemical vapor deposition on polycrystalline Cu,” *J. Phys. Chem. C*, vol. 116, no. 42, pp. 22492–22501, 2012.

[94] P. E. . B. Moulder, J.F.; Stickle, W.F.; Sobol, *Handbook of X-ray Photoelectron Spectroscopy*, no. 1. Minnesota; Perkin-Elmer Corporation, 1992.

[95] M. Tryus, “Extreme Ultraviolet Reflectometry for Structural and Optical Characterization of Thin Films and Layer Systems,” 2018.

[96] A. Comisso, M. Nardello, A. Giglia, and P. Nicolosi, “Optical constants of e-beam evaporated titanium dioxide thin films in the 25.5- to 612-eV energy region,” *Opt. Eng.*,

vol. 55, no. 9, p. 095102, Sep. 2016.

[97] R. Soufli and E. M. Gullikson, “Reflectance measurements on clean surfaces for the determination of optical constants of silicon in the extreme ultraviolet-soft-x-ray region.,” *Appl. Opt.*, vol. 36, no. 22, pp. 5499–507, 1997.

[98] L. V. Rodríguez-de Marcos, J. I. Larruquert, J. A. Méndez, and J. A. Aznárez, “Self-consistent optical constants of MgF_2, LaF_3, and CeF_3 films,” *Opt. Mater. Express*, vol. 7, no. 3, p. 989, Mar. 2017.

[99] L. V. Rodríguez-de Marcos, J. I. Larruquert, J. A. Méndez, and J. A. Aznárez, “Self-consistent optical constants of SiO_2 and Ta_2O_5 films,” *Opt. Mater. Express*, vol. 6, no. 11, p. 3622, Nov. 2016.

[100] A. Kiani, K. Venkatakrishnan, B. Tan, and V. Venkataramanan, “Maskless lithography using silicon oxide etch-stop layer induced by megahertz repetition femtosecond laser pulses,” *Opt. Express*, vol. 19, no. 11, p. 10834, 2011.

[101] S. T. Pantelides, *The Physics of SiO2 and its Interfaces*, 1st Editio. Elsevier, 1978.

[102] D. Goldstein, *Handbook of Polarized light*, 2nd ed. New york, 2003.

[103] H. G. Tompkins, E. A. Irene, C. Hill, and N. Carolina, *Handbook of Ellipsometry*. 2005.

[104] D. L. Windt, “IMD - Software for modeling the optical properties of multilayer films,” *Comput. Phys.*, vol. 12, no. 4, pp. 360–370, 1998.

[105] L. C. M. Lavras, A. J. Damião, and N. A. S. Rodrigues, “OPTICAL PROPERTIES OF ZrO 2 AND Ta 2 O 5,” vol. 21, no. 11, pp. 3622–3637, 2002.

[106] H. R. Philipp, “Optical properties of non-crystalline Si, SiO, SiOx and SiO2,” *J. Phys. Chem. Solids*, vol. 32, no. 8, pp. 1935–1945, Jan. 1971.

[107] C. Tarrio and S. E. Schnatterly, “Optical properties of silicon and its oxides,” *J. Opt. Soc. Am. B*, vol. 10, no. 5, p. 952, 1993.

[108] E. Filatova, V. Lukyanov, C. Blessing, and J. Friedrich, “Reflection spectra and optical constants of noncrystalline SiO2 in the soft x-ray region,” *J. Electron Spectros. Relat. Phenomena*, vol. 79, no. Supplement C, pp. 63–66, 1996.

[109] E. Palik, *Handbook of Optical Constants of Solids*, 1st Editio. Academic Press, 1998.

[110] A. Gray, M. Balooch, S. Allegret, S. De Gendt, and W.-E. Wang, "Optical detection and characterization of graphene by broadband spectrophotometry," *J. Appl. Phys.*, vol. 104, no. 5, p. 053109, Sep. 2008.

[111] F. J. Nelson, V. K. Kamineni, T. Zhang, E. S. Comfort, J. U. Lee, and A. C. Diebold, "Optical properties of large-area polycrystalline chemical vapor deposited graphene by spectroscopic ellipsometry," *Appl. Phys. Lett.*, vol. 97, no. 25, pp. 1–4, 2010.

[112] R. R. Nair *et al.*, "Fine structure constant defines visual transparency of graphene," *Science (80-.).*, vol. 320, no. 5881, p. 1308, 2008.

[113] B. Majérus *et al.*, "Modified Brewster angle on conducting 2D materials," *2D Mater.*, vol. 5, no. 2, p. 025007, Jan. 2018.

[114] Y. L. Liu *et al.*, "Using optical anisotropy as a quality factor to rapidly characterize structural qualities of large-area graphene films," *Anal. Chem.*, vol. 85, no. 3, pp. 1605–1614, 2013.

[115] I. K. Kim and D. E. Aspnes, "Analytic determination of n, κ, and d of an absorbing film from polarimetric data in the thin-film limit," *J. Appl. Phys.*, vol. 101, no. 3, p. 33109, Feb. 2007.

[116] R. Lazzari, G. Renaud, C. Revenant, J. Jupille, and Y. Borensztein, "Adhesion of growing nanoparticles at a glance: Surface differential reflectivity spectroscopy and grazing incidence small angle x-ray scattering," *Phys. Rev. B*, vol. 79, no. 12, p. 125428, Mar. 2009.

[117] P. Adamson, "Inverse relationships for ellipsometry of uniaxially anisotropic nanoscale dielectric films on isotropic materials," *Opt. Commun.*, vol. 285, no. 13–14, pp. 3210–3216, 2012.

[118] I. N. Kholmanov *et al.*, "Improved electrical conductivity of graphene films integrated with metal nanowires," *Nano Lett.*, vol. 12, no. 11, pp. 5679–5683, 2012.

[119] N. Liu, Z. Pan, L. Fu, C. Zhang, B. Dai, and Z. Liu, "The origin of wrinkles on transferred graphene," *Nano Res.*, vol. 4, no. 10, pp. 996–1004, Oct. 2011.

[120] S. J. Chae *et al.*, "Synthesis of large-area graphene layers on poly-nickel substrate by chemical vapor deposition: Wrinkle formation," *Adv. Mater.*, vol. 21, no. 22, pp. 2328–2333, 2009.

[121] N. C. M. 2. 3. 1. Fairley, "Casaxpx Processing Software for Xps Spectra." Casa Software Ltd, 2009, Englang.

[122] N. A. Malik, P. Nicolosi, A. E. H. Gaballah, K. Jimenez, and P. Zuppella, "EUV reflective ellipsometry in laboratory: determination of the optical constants and phase retarder properties of SiO2 at hydrogen Lyman–alpha," in *EUV and X-ray Optics: Synergy between Laboratory and Space VI*, 2019, vol. 110320V, no. April, p. 32.

[123] H. Proehl, R. Nitsche, T. Dienel, K. Leo, and T. Fritz, "In situ differential reflectance spectroscopy of thin crystalline films of PTCDA on different substrates," *Phys. Rev. B - Condens. Matter Mater. Phys.*, vol. 71, no. 16, p. 165207, Apr. 2005.

[124] J. D. E. McIntyre and D. E. Aspnes, "Differential reflection spectroscopy of very thin surface films," *Surf. Sci.*, vol. 24, no. 2, pp. 417–434, 1971.

[125] T. Stauber, N. M. R. Peres, and A. K. Geim, "Optical conductivity of graphene in the visible region of the spectrum," *Phys. Rev. B - Condens. Matter Mater. Phys.*, vol. 78, no. 8, pp. 1–8, 2008.

[126] Y. V Bludov, N. M. R. Peres, and M. I. Vasilevskiy, "Unusual reflection of electromagnetic radiation from a stack of graphene layers at oblique incidence," *J. Opt.*, vol. 15, no. 11, p. 114004, Nov. 2013.

[127] F. Bonaccorso, Z. Sun, T. Hasan, and A. C. Ferrari, "Graphene photonics and optoelectronics," *Nat. Photonics*, vol. 4, no. 9, pp. 611–622, Sep. 2010.

[128] P. E. Gaskell, H. S. Skulason, C. Rodenchuk, and T. Szkopek, "Counting graphene layers on glass via optical reflection microscopy," *Appl. Phys. Lett.*, vol. 94, no. 14, pp. 10–13, 2009.

[129] R. J. E. Jaspers, "Plasma spectroscopy," in *Fusion Science and Technology*, 2012, vol. 61, no. 2 T, pp. 384–393.

[130] D. W. Hahn and N. Omenetto, "Laser-induced breakdown spectroscopy (LIBS), part I:

Review of basic diagnostics and plasmaparticle interactions: Still-challenging issues within the analytical plasma community," in *Applied Spectroscopy*, 2010, vol. 64, no. 12, pp. 335–366.

[131] S. Braun, H. Mai, M. Moss, and R. Scholz, "Mo/Si multilayers with different barrier layers for applications as EUV mirrors," in *2001 International Microprocesses and Nanotechnology Conference, MNC 2001*, 2001, pp. 90–91.

[132] F. (US) Martin Richardson, Geneva, "EUV, XUV, AND X-RAY WAVELENGTH SOURCES CREATED FROM LASER PLASMA PRODUCED FROM LIQUID METAL SOLUTIONS, AND NANO-SIZE PARTICLES IN SOLUTIONS," 2002.

[133] J. L. Krause, K. J. Schafer, and K. C. Kulander, "High-order harmonic generation from atoms and ions in the high intensity regime," *Phys. Rev. Lett.*, vol. 68, no. 24, pp. 3535–3538, 1992.

[134] M. E. Koepke, "Interrelationship between lab, space, astrophysical, magnetic fusion, and inertial fusion plasma experiments," *Atoms*, vol. 7, no. 1. pp. 1–10, 2019.

[135] R. W. Eason *et al.*, "Multi-beam pulsed laser deposition for advanced thin-film optical waveguides," *J. Phys. D. Appl. Phys.*, vol. 47, no. 3, 2014.

[136] J. Scaffidi, S. M. Angel, and D. A. Cremers, "Emission enhancement mechanisms in dual-pulse LIBS," *Analytical Chemistry*, vol. 78, no. 1. pp. 24–32, 2006.

[137] D. W. Hahn and N. Omenetto, "Laser-Induced Breakdown Spectroscopy (LIBS), Part I: Review of Basic Diagnostics and Plasma—Particle Interactions: Still-Challenging Issues within the Analytical Plasma Community," *Appl. Spectrosc.*, vol. 64, no. 12, pp. 335A-336A, Dec. 2010.

[138] S. S. Harilal, M. S. Tillack, Y. Tao, B. O'Shay, R. Paguio, and A. Nikroo, "Extreme-ultraviolet spectral purity and magnetic ion debris mitigation by use of low-density tin targets," *Opt. Lett.*, vol. 31, no. 10, p. 1549, 2006.

[139] J. R. Freeman, S. S. Harilal, T. Sizyuk, A. Hassanein, and B. Rice, "Wavelength dependence of prepulse laser beams on EUV emission from CO 2 reheated Sn plasma," in *Extreme Ultraviolet (EUV) Lithography III*, 2012, vol. 8322, p. 83220H.

[140] T. Cummins, C. O'Gorman, P. Dunne, E. Sokell, G. O'Sullivan, and P. Hayden, "Colliding laser-produced plasmas as targets for laser-generated extreme ultraviolet sources," *Appl. Phys. Lett.*, vol. 105, no. 4, pp. 1–5, 2014.

[141] M. N. R. Ashfold, F. Claeyssens, G. M. Fuge, and S. J. Henley, "Pulsed laser ablation and deposition of thin films," *Chem. Soc. Rev.*, vol. 33, no. 1, p. 23, 2004.

[142] A. Tselev, A. Gorbunov, and W. Pompe, "Cross-beam pulsed laser deposition: General characteristic," *Rev. Sci. Instrum.*, vol. 72, no. 6, pp. 2665–2672, Jun. 2001.

[143] J. Dardis and J. T. Costello, "Stagnation layers at the collision front between two laser-induced plasmas: A study using time-resolved imaging and spectroscopy," *Spectrochim. Acta Part B At. Spectrosc.*, vol. 65, no. 8, pp. 627–635, Aug. 2010.

[144] S. L. Gupta, P. K. Pandey, and R. K. Thareja, "Dynamics of laser ablated colliding plumes," *Phys. Plasmas*, vol. 20, no. 1, p. 013511, Jan. 2013.

[145] P. W. Rambo and J. Denavit, "Time-implicit fluid simulation of collisional plasmas," *J. Comput. Phys.*, vol. 98, no. 2, pp. 317–331, 1992.

[146] C. Chenais-Popovics *et al.*, "Kinetic to thermal energy transfer and interpenetration in the collision of laser-produced plasmas," *Phys. Plasmas*, vol. 4, no. 1, pp. 190–208, 1997.

[147] E. C. Merritt, A. L. Moser, S. C. Hsu, J. Loverich, and M. Gilmore, "Experimental characterization of the stagnation layer between two obliquely merging supersonic plasma jets," *Phys. Rev. Lett.*, vol. 111, no. 8, p. 085003, Aug. 2013.

[148] K. F. Al-Shboul *et al.*, "Interpenetration and stagnation in colliding laser plasmas," *Phys. Plasmas*, vol. 21, no. 1, p. 013502, Jan. 2014.

[149] H. Photonics, *Digital CCD Camera C8484-05G02 Instruction Manual*, vol. ver 1 ed. Hamamatsu Photonics, 2009.

[150] and N. A. T. (2018) Kramida, A., Ralchenko, Yu., Reader, J., "NIST atomic spectra database (ver. 5.6.1)," 2018. [Online]. Available: https://www.nist.gov/pml/atomic-spectra-database.

[151] N. Konjević, A. Lesage, J. R. Fuhr, and W. L. Wiese, "Experimental Stark widths and shifts for spectral lines of neutral and ionized atoms (A critical review of selected data for

the period 1989 through 2000),” *J. Phys. Chem. Ref. Data*, vol. 31, no. 3, pp. 819–927, 2002.